

# SEGMENTATION OF DIFFUSION WEIGHTED MRI USING THE LEVEL SET FRAMEWORK

THÈSE N° 3315 (2005)

PRÉSENTÉE À LA FACULTÉ SCIENCES ET TECHNIQUES DE L'INGÉNIEUR

Institut de traitement des signaux

SECTION DE GÉNIE ÉLECTRIQUE ET ÉLECTRONIQUE

ÉCOLE POLYTECHNIQUE FÉDÉRALE DE LAUSANNE

POUR L'OBTENTION DU GRADE DE DOCTEUR ÈS SCIENCES

PAR

Lisa JONASSON

M.Sc. in Engineering physics, Chalmers University of Technology, Göteborg, Suède  
de nationalité suédoise

acceptée sur proposition du jury:

Prof. J.-P. Thiran, directeur de thèse  
Prof. C. Alberola, rapporteur  
Dr E. Leriche, rapporteur  
Prof. P. Vandergheynst, rapporteur  
Prof. V. Wedeen, rapporteur

Lausanne, EPFL  
2005



*Nog finns det mål och mening i vår färd -  
men det är vägen, som är mödan värd.*  
Karin Boye <sup>a</sup>

---

<sup>a</sup>Yes, there is goal and meaning in our path - but it's the way that is the labour's worth.



---

# Contents

---

<b>Contents</b>	<b>v</b>
<b>List of Figures</b>	<b>ix</b>
<b>List of Tables</b>	<b>xiii</b>
<b>Acknowledgments</b>	<b>xv</b>
<b>Abstract</b>	<b>xvii</b>
<b>Version Abrégée</b>	<b>xix</b>
<b>Notations and symbols</b>	<b>xxi</b>
<b>1 Introduction and Preview</b>	<b>1</b>
1.1 Motivation . . . . .	1
1.1.1 Aim of the thesis . . . . .	2
1.1.2 Main contributions . . . . .	2
1.2 Outline . . . . .	3
<b>2 MR and Diffusion Imaging</b>	<b>7</b>
2.1 Introduction . . . . .	7
2.2 Magnetic Resonance Imaging . . . . .	7
2.2.1 Brief history . . . . .	7
2.2.2 Physical principles of MRI . . . . .	8
2.2.3 Image formation and k-space . . . . .	10
2.3 Diffusion Weighted MRI . . . . .	12
2.3.1 Physical principles of diffusion . . . . .	12
2.3.2 Image formation and q-space . . . . .	14
2.3.3 Diffusion tensor imaging . . . . .	17

---

2.3.4	High angular resolution diffusion imaging . . . . .	21
2.3.5	Tractography . . . . .	24
2.3.6	Potential applications . . . . .	25
<b>3</b>	<b>A fiber clustering technique for defining tracts</b>	<b>27</b>
3.1	Introduction . . . . .	27
3.2	Method . . . . .	28
3.3	Implementation details . . . . .	29
3.4	Data . . . . .	30
3.5	Results . . . . .	30
3.6	Discussion and Conclusion . . . . .	33
<b>4</b>	<b>Image segmentation with the level set method</b>	<b>37</b>
4.1	Introduction . . . . .	37
4.2	The Level Set Method . . . . .	38
4.2.1	The level set equation . . . . .	39
4.2.2	Curvature . . . . .	41
4.3	Variational formulation . . . . .	44
4.4	Geodesic Active Contours and surfaces . . . . .	45
4.5	Region based segmentation front propagation. . . . .	47
4.5.1	Geodesic active regions . . . . .	47
4.5.2	Active contours without edges . . . . .	49
4.6	Numerical implementation of the level sets. . . . .	51
4.6.1	The upwind scheme . . . . .	51
4.6.2	Stability condition . . . . .	52
4.6.3	Preserving the level set function . . . . .	52
4.6.4	Implementation . . . . .	53
4.7	Summary . . . . .	53
<b>5</b>	<b>A local front propagation method for white matter segmentation</b>	<b>55</b>
5.1	Introduction . . . . .	55
5.2	Method . . . . .	57
5.2.1	Similarity measures of DT . . . . .	57
5.2.2	The similarity based front propagation . . . . .	58
5.2.3	Regularization . . . . .	59
5.3	Implementation details . . . . .	60
5.3.1	Thresholding . . . . .	60
5.3.2	Weighting the Speed Terms . . . . .	60
5.4	Data . . . . .	60
5.4.1	Synthetic Tensor Fields . . . . .	60
5.4.2	Real DT-MRI . . . . .	62
5.5	Results and validation . . . . .	63

---

5.5.1	Synthetic Tensor Fields . . . . .	63
5.5.2	Real DT-MRI . . . . .	67
5.6	Discussion . . . . .	71
5.7	Conclusion . . . . .	71
<b>6</b>	<b>Evolving hyper surfaces for segmentation in position orientation space</b>	<b>73</b>
6.1	Introduction . . . . .	73
6.2	Position Orientation Space . . . . .	74
6.3	Method and implementation . . . . .	76
6.3.1	Creating POS . . . . .	76
6.3.2	Evolution of the hyper-surface. . . . .	76
6.4	Data . . . . .	76
6.4.1	Synthetic data . . . . .	76
6.4.2	Real data set . . . . .	76
6.5	Results and validation . . . . .	77
6.5.1	Synthetic data . . . . .	77
6.5.2	Real data set . . . . .	77
6.6	Discussion and Conclusion . . . . .	77
<b>7</b>	<b>Region based segmentation of tensor fields</b>	<b>81</b>
7.1	Introduction . . . . .	81
7.2	Method . . . . .	82
7.2.1	Coupling Forces . . . . .	84
7.2.2	Final evolution . . . . .	84
7.3	Implementation details and parameters . . . . .	84
7.4	Data . . . . .	86
7.4.1	Synthetic data set . . . . .	86
7.4.2	Real data set . . . . .	86
7.5	Results and validation . . . . .	88
7.5.1	Synthetic data set . . . . .	88
7.5.2	Segmentation of the thalamus . . . . .	88
7.6	Application of tensor segmentation in fluid dynamics . . . . .	96
7.7	Discussion and Conclusion . . . . .	102
<b>8</b>	<b>Discussion and conclusion</b>	<b>105</b>
8.1	Review of discussed topics . . . . .	105
8.2	Achievements . . . . .	106
8.3	Potential applications . . . . .	106
8.4	Discussion and future directions . . . . .	107
8.4.1	Region based segmentation of tensor fields . . . . .	108
8.4.2	Position-orientation space . . . . .	108
8.4.3	Spectral clustering . . . . .	108

8.4.4 Distance maps . . . . .	109
<b>Bibliography</b>	<b>111</b>
<b>Index</b>	<b>118</b>
<b>Curriculum Vitae</b>	<b>119</b>



---

# List of Figures

---

1.1	Main contributions . . . . .	4
2.1	Anatomical MRI and functional MRI . . . . .	9
2.2	$T_1$ -weighted and $T_2$ -weighted MR images. . . . .	10
2.3	Schematic figure of a typical imaging sequence for sampling $\mathbf{k}$ -space. . . . .	11
2.4	Water mobility restricted by axonal cell membrane and myelin sheath . . . . .	12
2.5	Schematic figure of a Pulse Gradient Spin Echo sequence for imaging diffusion along one gradient direction. . . . .	15
2.6	Examples of Diffusion Weighted MRI. . . . .	16
2.7	Visualization of the Diffusion Tensor . . . . .	18
2.8	From diffusion to the diffusion tensor. . . . .	19
2.9	A coronal slice of Diffusion tensors of the brain. . . . .	20
2.10	Visualizations of a Diffusion Tensor field using a) Mean diffusion map b) Fractional anisotropy map c) Color map . . . . .	21
2.11	From diffusion to the Orientation Distribution Function with DSI . . . . .	23
2.12	A coronal slice of ODFs of the brain . . . . .	24
2.13	Fiber tractography from DTI and DSI data. . . . .	25
3.1	The affinity matrix. . . . .	29
3.2	Clustering results for long fibers I . . . . .	31
3.3	Clustering results for long fibers II . . . . .	32
3.4	Histogram of the fiber lengths. . . . .	33
3.5	Clustering results for short fibers. . . . .	34
4.1	Examples of the power of the level sets as a segmentation tool. . . . .	38
4.2	Example of the level set principle for a curve in 2D. . . . .	39
4.3	An interface moving with a speed $F$ defined on every point of the interface. . . . .	40
4.4	The interface embedded in a level set function. . . . .	40
4.5	Flow evolving under minimal principal curvature. . . . .	43
4.6	Example of cube evolving under mean curvature flow. . . . .	43
4.7	A hyper-cube evolving under 5D mean curvature flow. . . . .	44

---

4.8	Segmentation of two 2D objects from one initial surface using the Geodesic Active Contour method. . . . .	46
4.9	Segmentation of four 3D objects from one initial surface using the Geodesic Active Surface method. . . . .	48
4.10	Region based segmentation with Geodesic Active Regions by evolving several coupled level sets. . . . .	49
4.11	Segmentation of the thalamus using Geodesic Active Regions. . . . .	50
4.12	Rosa's hand segmented by Xavier Bresson, using the Chan-Vese method. . .	51
4.13	Regions of interest when computing derivatives according to the upwind scheme. . . . .	52
5.1	Choice of adjacent voxels with respect to the normal of the surface. . . . .	59
5.2	Synthetic DT fields. . . . .	62
5.3	Effects of varying thresholds on the resulting segmentations of synthetic DT fields. . . . .	64
5.4	Effects of varying regularization parameter on the resulting segmentations of synthetic DT fields. . . . .	65
5.5	Segmentation of the left- and right cortico-spinal tract. . . . .	68
5.6	Segmentation of the corpus callosum. . . . .	69
5.7	Segmentation of the inferior long association bundles as a whole . . . . .	70
6.1	Example of POS for a 2D slice of a volume of ODFs. . . . .	75
6.2	Example of POS for a 2D slice of a volume of ODFs. . . . .	75
6.3	a) Slice of the synthetic 3D volume of ODFs. b) The intensity of the different angles plotted against each other. c) The 3D projection of the 5D result. . .	77
6.4	Results from application on HARD MRI from a human brain. . . . .	78
6.5	Results from application on HARD MRI from a human brain. . . . .	78
7.1	A cut of the synthetic tensor field used to test the segmentation method. . .	87
7.2	A cut of the segmentation result on a synthetic field. . . . .	89
7.3	Placing of the initial surfaces for the segmentation of the thalamus. . . . .	90
7.4	The segmentation of the thalamus displayed as a 3D surface on a horizontal cut of the fractional anisotropy map. . . . .	91
7.5	The segmentation of the thalamus displayed on horizontal cuts of the fractional anisotropy map. . . . .	92
7.6	The segmentation of the thalamus displayed on coronal cuts of the fractional anisotropy map. . . . .	93
7.7	The segmentation of the thalamic nuclei displayed on horizontal cuts of the fractional anisotropy. . . . .	94
7.8	The segmentation of the thalamic nuclei displayed on coronal cuts of the fractional anisotropy. . . . .	95
7.9	The segmentation of the thalamic nuclei seen in 3D. . . . .	96
7.10	The segmentation of the thalamic nuclei co-registered with SWSA. . . . .	97

---

7.11	Experimental set up of the lid-driven flow. . . . .	99
7.12	Color map slices of the Reynolds stress tensors from a flow in a lid-driven cubical cavity. . . . .	100
7.13	Results from segmentation of Reynolds stress tensors obtained from a flow in a lid-driven cubical cavity. . . . .	101
7.14	Results from article by Leriche et al. [66]. . . . .	101
7.15	Fiber tractography between the thalamus, segmented by our method, and the cortex. . . . .	103



---

# List of Tables

---

5.1	Comparison between similarity measures between different combinations of isotropic and anisotropic tensors. . . . .	58
5.2	Quantitative values of the segmentation results for different thresholds. . . .	66
5.3	Quantitative values of the segmentation results using different levels of regularization. . . . .	66



---

# Acknowledgments

---

Many people have been very important to me during my four years at Signal Processing Institute (ITS) at EPFL and I would like to thank them all. The first person I would like to thank is my thesis advisor Jean-Philippe Thiran for being very supportive and encouraging during my whole thesis. I would also like to thank Murat Kunt, the director of ITS for welcoming me to the lab.

Further, I would like to thank all the members of my jury; Carlos Alberola, who with his good knowledge in diffusion imaging provided very interesting and constructive feedback on my thesis. Emmanuel Leriche, who I have been working with on the fluid dynamics part. Pierre Vandergheynst, who evaluated this work with his mathematical background. Last of the jury members but definitely not least, I would like to thank Van Wedeen for participating in my jury but even more for welcoming me in Boston and sharing his knowledge, brilliant ideas and enthusiasm with me.

At ITS there are two persons that have been very important to me, Xavier Bresson and Patric Hagmann. Xavier has helped me understanding the world of level sets and he has also been a moral support and a good friend whenever I needed it. Patric and I have discovered diffusion imaging together, he has always been a great help and we have been sharing a lot of ideas and thoughts about work and life in our common office. Thank you also to Reto Meuli and to Leila Cammoun for their collaboration.

I would also like to thank all the people that read my thesis: Meritxell Bach, Olivier Cuisenaire, Christina Granziera and my parents for their constructive comments. A special thanks to Christina also for taking so good care of me, together with Nouchine, in Boston. Thank you also to all the students (Cecilia, Raphael etc.) I have had that all have provided great work and taught me a lot of things. I would also like to thank all the great people that I have met at conferences around the world for providing so much inspiration, especially Olivier Coulon and Anders Brun that I have seen several times.

All the other people at ITS have also been absolutely great and made going to work so much fun, we have shared many good coffee breaks, beach volley matches and ski days together. Thank you also to the Brain group that welcomed me when I first arrived in Lausanne and to Marianne and Gilles. I would also like to give a little extra thanks to Patricia and Zen for being good friends. My friends outside the lab (especially Sanna and Jenny) have also been very important to keep my mind off work and the Rinaldi family,

that took well care of me in the beginning.

A special thanks to my family; my parents, my brothers and my grandmothers, that have always been very supportive and close, even though the distance between us is far.

Finally I would like to thank Julien, for his good ideas but most of all for always believing in me, loving me and bringing me so much happiness.



---

# Abstract

---

Medical imaging is a rapidly growing field in which diffusion imaging is a recently developed modality. This novel imaging contrast permits in-vivo measurement of the diffusion of water molecules. This is particularly interesting in brain imaging where the diffusion reveals an amazing insight into the neuronal organization and cerebral cytoarchitecture. Diffusion images contain from six up to hundreds of values in each voxel and are represented as tensor fields (Diffusion Tensor Imaging (DTI)) or as fields of functions (High Angular Resolution Diffusion (HARD) imaging). To fully extract the large amount of data contained within these images new processing and analysis tools are needed. The aim of this thesis is the development of such tools.

The method we have been mainly focusing on for this purpose is the level set method. The level set method is a numerical and theoretical tool for propagating interfaces. In image processing it is used for propagating curves in 2D or surfaces in 3D for delineation of objects or for regularization purposes. In this thesis we have explored some of the numerous aspects of the level set frame work to see how the diffusion properties can be used for segmentation.

For segmentation of tensor fields we have considered similarity measures for comparison of tensors. From these similarity measures several applications of the level set method have been developed for the segmentation of different structures. Different measures of similarity have been used dependent on the application. When segmenting white matter regions in DTI, the similarity measure emphasizes anisotropic regions. The segmentation algorithm itself has a very local dependence since white matter, in general fiber tracts, experiences different diffusion in different parts of the structure. The presented results show segmentations of the major fiber tracts in the brain. Other structures, such as the deep cerebral nuclei, that are mainly composed of gray matter, have more homogenous diffusion properties than white matter structures. Therefore, in these structures we maximize the internal coherence within the entire structure by using a region based approach to the segmentation problem. Segmentations of the thalamus and its nuclei as well as on tensor fields from fluid mechanics are presented.

For High Angular Resolution Diffusion (HARD) images, two methods for fiber tract segmentation are presented based on different types of coherence. The coherence is either measured as the similarity between fibers obtained from a tractography algorithm, or the similarity of scalar values in a five-dimensional non-Euclidean space. The similarity between

two fibers is determined by a counting strategy and is equal to the number of voxels they have in common. A spectral clustering algorithm is then used for grouping fibers with a high inter-resemblance. When segmenting white matter with the level set method, we propose to expand the space we are working in from a three-dimensional space of Orientation Distribution Functions (ODF) to a five-dimensional space of position and orientation. By a careful definition of this space and an adaptation of the level set to five dimensions the fibers tracts can be segmented as separated structures. We show some preliminary results from segmentations in this 5D space.

The approaches proposed in this thesis permit a consideration of the fiber tracts and gray matter structures as an entity, allowing quantitative measures of the diffusion without losing information by simplifying the images to scalar representations.

---

# Version Abrégée

---

L'imagerie médicale est un domaine en grande expansion et une des dernières modalités développées dans ce domaine est l'imagerie de diffusion. Ce nouveau contraste nous permet de mesurer la diffusion des molécules d'eau in vivo. Cet effet est particulièrement intéressant en imagerie cérébrale puisqu'il peut fournir une meilleure compréhension de l'organisation neuronale et de l'architecture des cellules cérébrales. Contenant une gigantesque quantité de données, ces images doivent être traitées et analysées pour en extraire l'information intéressante, ce qui justifie la nécessité de nouveaux outils. L'objectif de cette thèse est le développement de ce genre d'outils pour mieux analyser des données de ce type d'images, surtout des champs tensoriels.

La méthode principalement étudiée est la méthode des courbes de niveaux. Les courbes de niveaux sont un outil numérique et théorique pour la propagation des fronts. Dans le traitement d'image ils sont utilisés pour la segmentation des objets par la propagation des courbes en 2D ou des surfaces en 3D. Dans cette thèse nous avons exploré les possibilités d'utiliser l'approche de courbes de niveaux pour la segmentation en utilisant les propriétés de la diffusion.

Pour la segmentation des champs tensoriels nous avons exploré des mesures de similarité pour la comparaison entre tenseurs. A partir de ces mesures de similarité plusieurs applications ont été développées pour la segmentation des structures différentes. Différentes mesures de similarité ont été utilisées en fonction de leur application. Pour la segmentation de régions de matière blanche dans des champs tensorielles, une mesure qui met en évidence l'anisotropie a été utilisée pour une propagation de front très locale. Nous montrons des résultats pour la segmentation des tractus de fibres majeurs dans le cerveau. A cause de la nature des données tensorielles, le problème de croisement des fibres ne peut pas être résolu avec cette méthode. C'est pourquoi nous utilisons des images de diffusion de haute résolution angulaire pour segmenter ce genre d'images. La segmentation est faite en définissant un nouvel espace non-euclidien de cinq dimensions décrivant l'orientation et la position d'un tenseur et en adaptant les courbes de niveaux à cet espace de haute dimension.

Nous présentons aussi une autre méthode de courbes de niveaux basée sur des régions pour segmenter des champs tensoriels. En imagerie de diffusion cette méthode a été adaptée pour segmenter des structures de matière grise mais elle a aussi été appliquée sur des champs tensoriels provenant de la dynamique des fluides. Une méthode pour segmenter des paquets

(tractus) de fibres a aussi été présentée en utilisant un algorithme de groupement spectral.

Les méthodes proposées dans cette thèse permettent des mesures quantificatives sans pour autant devoir simplifier les images tensorielles et les images de fonctions à des images scalaires.

---

# Notations and symbols

---

## Abbreviations

ADC	Apparent Diffusion Coefficient
DT	Diffusion Tensor
DTI	Diffusion Tensor Imaging
DT-MRI	Diffusion Tensor Magnetic Resonance Imaging
DSI	Diffusion Spectrum Imaging
FA	Fractional Anisotropy
fMRI	functional Magnetic Resonance Imaging
FID	Free Induction Decay
HARD	High Angular Resolution Diffusion
HARDI	High Angular Resolution Diffusion Imaging
IS	Integrated similarity
MR	Magnetic Resonance
MRI	Magnetic Resonance Imaging
NMR	Nuclear Magnetic Resonance
NTSP	Normalized Tensor Scalar Product
ODF	Orientation Distribution Function
PAS	Persistent Angular Structure
PDE	Partial Differential Equation
PDF	Probability Distribution Function
POS	Position Orientation Space
RGB	Red-Green-Blue, vector used for color images
RF	Radio Frequency
RST	Reynolds stress tensor
SNR	signal to noise ratio
SWSA	Schaltenbrandt atlas
TSP	Tensor scalar product
TD	Tensor Difference
2D	two-dimensional
3D	three-dimensional
ND	any number of dimensions

## Diffusion MRI

$\mathbf{B}_0$	external magnetic field
$\mathbf{B}_1$	time-varying rotating magnetic field acting perpendicular to $\mathbf{B}_0$
$\mathbf{M}$	spin magnetization vector
$\gamma$	gyro magnetic ratio specific for each kind of nucleus
$\omega_0$	the Larmor frequency, the resonance frequency for the spin system, $\omega_0 = \gamma \mathbf{B}_0$
$\tau$	the time the RF pulse is acting
$\alpha$	tip angle between $\mathbf{M}$ and the z-axis (along $\mathbf{B}_0$ , $\alpha = \gamma \mathbf{B}_1 \tau$
$T_1$	spin-lattice relaxation time
$T_2$	spin-spin relaxation time
$G_x, G_y, G_z$	linear field gradients along $x, y, z$
$\delta$	field gradient duration
$\varphi$	phase-shift induced by the linear field gradients, $\varphi = \gamma \delta G_y y$
<b>k-space</b>	reciprocal space for sampling of the MR-signal
$\mathbf{r}, \mathbf{r}'$	position vectors
$P_s(\mathbf{r}'   \mathbf{r}, t)$	probability of self-diffusion
$P(\mathbf{r}', t)$	probability of finding a particle at position $\mathbf{r}'$ at time $t$
$\rho(\mathbf{r})$	particle density at position $\mathbf{r}$
$J$	flux
$D$	diffusion coefficient
$\Delta$	the time between the two gradient pulses
$\mathbf{g}$	linear field gradient in any direction, $\mathbf{u}$ where $\mathbf{g} = g\mathbf{u}$
$S$	the measured signal in the MRI experiment
<b>q-space</b>	reciprocal space for sampling the signal in a diffusion MRI experiment, $\mathbf{q} = \frac{1}{2\pi} \gamma \delta \mathbf{g}$
$\mathbf{R}$	total displacement, $\mathbf{R} = \mathbf{r} - \mathbf{r}'$
$\mathcal{F}$	the Fourier transform, the inverse is denoted $\mathcal{F}^{-1}$
$b$ -value	descriptor for the MR sequence, $b = \gamma^2 \delta^2 g^2 \Delta = \mathbf{q}^2 \Delta$
$\mathbf{D}$	the diffusion tensor
$d(\mathbf{x})$	diffusion in direction $\mathbf{x}$ , $d(\mathbf{x}) = \mathbf{x} \mathbf{D} \mathbf{x}$
$\lambda$	eigenvalue, for a diffusion tensor there are three, $\lambda_1 \geq \lambda_2 \geq \lambda_3$
$e_i$	eigenvectors corresponding to $\lambda_i$
$\varsigma$	length of vector $\mathbf{R} = \varsigma \mathbf{u}$ where $ \mathbf{u}  = 1$
$\mathbf{D}_1 : \mathbf{D}_2$	Tensor scalar product between $\mathbf{D}_1$ and $\mathbf{D}_2$ . Defined as $\text{Trace}(\mathbf{D}_1 \mathbf{D}_2)$ .

## Level set method

$\phi(\mathbf{x}(t), t)$	the level set function dependent on time, $t$ and position $\mathbf{x}$
$\Gamma$	symbol for curve/surface/hyper-surface in $\mathbb{R}^N$ such that $\Gamma(t) := \{\mathbf{x}(t) \mid \phi(\mathbf{x}(t), t) = 0\}$ $\phi < 0$ for points lying <i>inside</i> $\Gamma$ and $\phi \geq 0$ for points lying <i>outside</i> $\Gamma$
$F$	propagation speed for interface embedded by $\phi$
$\mathbf{n}$	normal
$\kappa_n$	principal curvatures
$\mathcal{G}$	Gaussian curvature
$\mathcal{M}$	mean curvature
$\phi_x$	the derivative of $\phi$ with respect to $x$
$\phi_{xx}$	second derivative of $\phi$ with respect to $x$
$\phi_{xy}$	cross derivative of $\phi$ with respect to $x$ and $y$
$P_p$	projection operator onto a space orthogonal to the vector $p$
$p$	a vector $p = (p_1, p_2)$
$\otimes$	tensor product
$E$	energy functional with the general form $\int_{\Omega} f(\mathbf{x}, \phi, \nabla \phi) d\Omega$
$\delta_{ij}$	Kroeneckers delta function
$f$	a monotonically decreasing function such that $f : [0, +\infty] \rightarrow \mathbb{R}^+$ and $f(0) = 1$ and $f \rightarrow 0$ as $x \rightarrow \infty$
$I$	an image $I : [0, a] \times [0, b] \rightarrow \mathbb{R}^+$
$g_{ij}$	a metric, in general expressed as: $f(\nabla I)[\delta_{ij}]$
$C(p)$	parametrized planar curve: $C(p) : [0, 1] \rightarrow \mathbb{R}^2$
$L_R$	length definition in Riemannian space, $\int_{C(p)} g_{ij} dx_i dx_j$
$A_R$	area definition in Riemannian space, $\int_{C(p)} g_{ij} dx_i dx_j$
$\mathcal{R}_i$	a region with boundary $\partial \mathcal{R}_i$
$p_i(s)$	probability of voxel $s$ belonging to region, $\mathcal{R}_i$
$c_1$	mean over region $\phi \geq 0$ , $\frac{\int_{\Omega} H_{\epsilon}(\phi) I dx}{\int_{\Omega} H_{\epsilon}(\phi)}$
$c_2$	mean over region $\phi < 0$ , $\frac{\int_{\Omega} (1-H_{\epsilon}(\phi)) I dx}{\int_{\Omega} (1-H_{\epsilon}(\phi))}$
$ds$	Euclidean arc length

## General

$\nabla$	the gradient operator
$\nabla^2$	Hessian derivative operator which corresponds to the second derivative
$\nabla \cdot$	divergence operator
$\frac{\partial}{\partial t}$	the derivative with respect to $t$
$\det$	determinant
$\langle \rangle$	mean
$\propto$	proportional to
$S^2$	the unit sphere
$\Omega$	image domain
$\partial\Omega$	the boundary of $\Omega$

$\mathbf{M}$	3D Euclidean space
$\varrho$	length of voxel sides in $\mathbf{M}$
$n$	numbering of fibers
$\mathbf{v}_i^n$	position of point $i$ of fiber $n$
$\mathbf{A}$	affinity matrix
$\Lambda$	eigenvalues of $\mathbf{A}$
$\mathbf{V}$	eigenvectors of $\mathbf{A}$
$\mathbf{V}_d$	$d$ first eigenvectors of $\mathbf{A}$
$\mathcal{N}(x)$	neighborhood of $x$
$T$	threshold
$H_T(x)$	Heaviside function
$\alpha, \beta, \gamma$	weighting parameters
$d_{ij}$	distance metric between two tensors
$c_i$	the sum of distances $d_{ij}$ to all other tensors within the region, $\mathcal{R}_i$
$H_i(j, \phi_j(s))$	coupling force for surface $i$ with respect to surface $j$
$D_{typ,i}$	the tensor best representing the tensors within region $\mathcal{R}_i$
$\varphi, \theta$	angles on the unit sphere



## Fluid dynamics

$\mathbf{U}(\mathbf{x}, t)$	velocity field
$\rho(\mathbf{x}, t)$	continuum density field
$L$	characteristic length scale
$U$	speed
$\nu$	molecular viscosity
$Re$	Reynolds number, $Re = UL/\nu$
$\langle \mathbf{U}(\mathbf{x}, t) \rangle$	mean velocity field
$u(\mathbf{x}, t)$	fluctuating velocity field $\langle u(\mathbf{x}, t) \rangle = 0$
$\langle u_i u_j \rangle$	Reynolds stress tensor
$k(\mathbf{x}, t)$	turbulent kinetic energy, $(\langle u_1^2 \rangle + \langle u_2^2 \rangle + \langle u_3^2 \rangle)/2$
$a_{ij}$	anisotropic stress $\langle u_i u_j \rangle - \frac{2}{3}k\delta_{ij}$



---

# Introduction and Preview

---

# 1

## 1.1 Motivation

Diffusion imaging is a new imaging modality that permits in-vivo measurement of the diffusion of water molecules. This imaging contrast is particularly interesting in brain imaging where it reveals an amazing insight of neuronal organization and cerebral cytoarchitecture. The diffusion images contain a large amount of data and to fully extract all information in the images they must be processed and analyzed. Image processing and analysis is also a relatively new science for automatic treatment of digitized images and videos that has grown with the use of computers and the multimedia society. An important branch of image analysis is dedicated to medical image analysis with the goal of improving the diagnostic and analytical tools for doctors and researchers. Automatic procedures for localization and delineation of structures remove the subjectivity of the human evaluator and are of great help for inter-subject comparisons.

Most traditional imaging methods in medicine produce gray scale images where the different gray levels correspond to different physical properties of the tissues. A digital gray scale image is a two- or three-dimensional grid of scalar values and for this type of image numerous image processing and analysis methods exist. For a vector valued image, where each pixel or voxel (as it is called in 3D) contains a vector as for example color images or directional data images, such methods also exist but are more complicated due to the increased complexity of the data. In diffusion imaging the complexity of the data increases even further and each voxel contains from six up to hundreds of values. For these new type of data new analysis methods need to be developed to fully exploit the possibilities that these images provide. Developing liable and robust analysis tools for the diffusion data will hopefully contribute to improve our knowledge of brain anatomy and brain function.

### 1.1.1 Aim of the thesis

The aim of this thesis has been to develop tools to make the information contained in these multi-valued images more accessible and quantifiable. The methods are general approaches for segmentation of tensor fields and fields of functions but the principal application is images from Diffusion Weighted Magnetic Resonance Imaging. At the beginning of this thesis, the only approaches available for analyzing diffusion data were scalar simplifications and fiber tracking. Throughout this thesis new tools for segmenting and localizing structures made visible through this new modality have been developed. Fiber tracking provides visually compelling images giving a qualitative appreciation of the neuronal connectivity but is often hard to quantify. Quantification is a critical issue for clinical studies and for diagnosis of neurological diseases and surgical planning. The approaches that we propose in this thesis are important since they delineates fiber tracts and gray matter structures as an entity which will allow quantification measures of the diffusion.

The framework we have been mainly focusing on for this purpose is the level set method, in particular the framework of active contours. The reason we have chosen this particular framework is the possibility of using a variety of features simultaneously. This can be image based features derived from the diffusion data or features of the segmentation result itself. The level set method is a numerical tool for propagating interfaces and in image processing they are used for propagating curves in 2D or surfaces in 3D for delineation of objects or for regularization purposes. The liberty of formulation of these propagating fronts gives us countless possibilities. Often the fronts are driven with the purpose of finding a minimum of an energy functional derived from the image but they can also be driven by other physical properties of the data. In this thesis we have explored some of the numerous aspects of this level set frame work to see how the diffusion properties can be used for finding useful image segmentations. An aspect we have concentrated on is how to compare diffusion properties for diffusion tensors (DT) and how these measures of similarities can be used for propagating fronts.

### 1.1.2 Main contributions

The main contributions of this thesis are illustrated in Figure 1.1 and can be summarized as follows:

- Development of a fully automatic clustering method for grouping fibres into bundles.
- Analysis of similarity measures for image segmentation purposes and a proposal of a new similarity measure that detects very subtle differences in diffusion between tensors.
- A novel approach to segmentation of tensor fields by using measures of similarity.
- Development of a method for white matter segmentation with the level set method using the full tensor information.

- Development of a region based segmentation method for tensor fields, especially adapted for gray matter segmentation.
- Definition of a new non-Euclidean 5D space of orientation and position for segmentation of high angular resolution diffusion images.
- Implementation of level sets in a 5D non-Euclidean space.

## 1.2 Outline

This dissertation is organized as follows:

- Chapter 2 Presentation of MR imaging basics with an emphasis on diffusion MRI. This chapter provides a background on image acquisition and better understanding of the nature of the data.
- Chapter 3 Presentation of a new clustering algorithm developed for grouping of fiber tracts. This clustering algorithm can be used as a practical visualization tool and as the bridge between a qualitative and quantitative analysis of the data. It is used to show the connection between fiber tractography and fiber tract segmentation by showing that fiber tracts can be considered as bundles of coherent fibers.
- Chapter 4 Presentation of the level set method and its use in image segmentation. Together with Chapter 2 this is the background on which this thesis is founded. This is an important chapter for understanding the underlying principles of the level set method that is used for segmenting structures in Chapter 5, Chapter 7 and Chapter 6.
- Chapter 5 Presentation of similarity measures between DTs and demonstration of how to use these similarity measures to define a front propagation with a local dependence. The front propagation is used for segmenting some of the major fiber tracts from DT-MRI in the human brain. The problem of regularizing curves with tubular structure is also addressed.
- Chapter 6 Segmentation of structures from high angular resolution diffusion images (HARDI) by changing the representation of the image. The 3D image of functions is extended to a 5D space of position and orientation. We show how to apply a region based level set method for gray scale images in this high-dimensional, non-Euclidean space. The adaptation of the mean curvature in such as high-dimensional space is discussed.
- Chapter 7 We show how a similarity measure can be used to define regions which can be used to define an energy functional. Minimizing this functional corresponds to the optimal segmentation of the tensor field. This method is used for segmenting the thalamus and its nuclei from DT-MRI. We also show examples how it can be used in fluid dynamics.

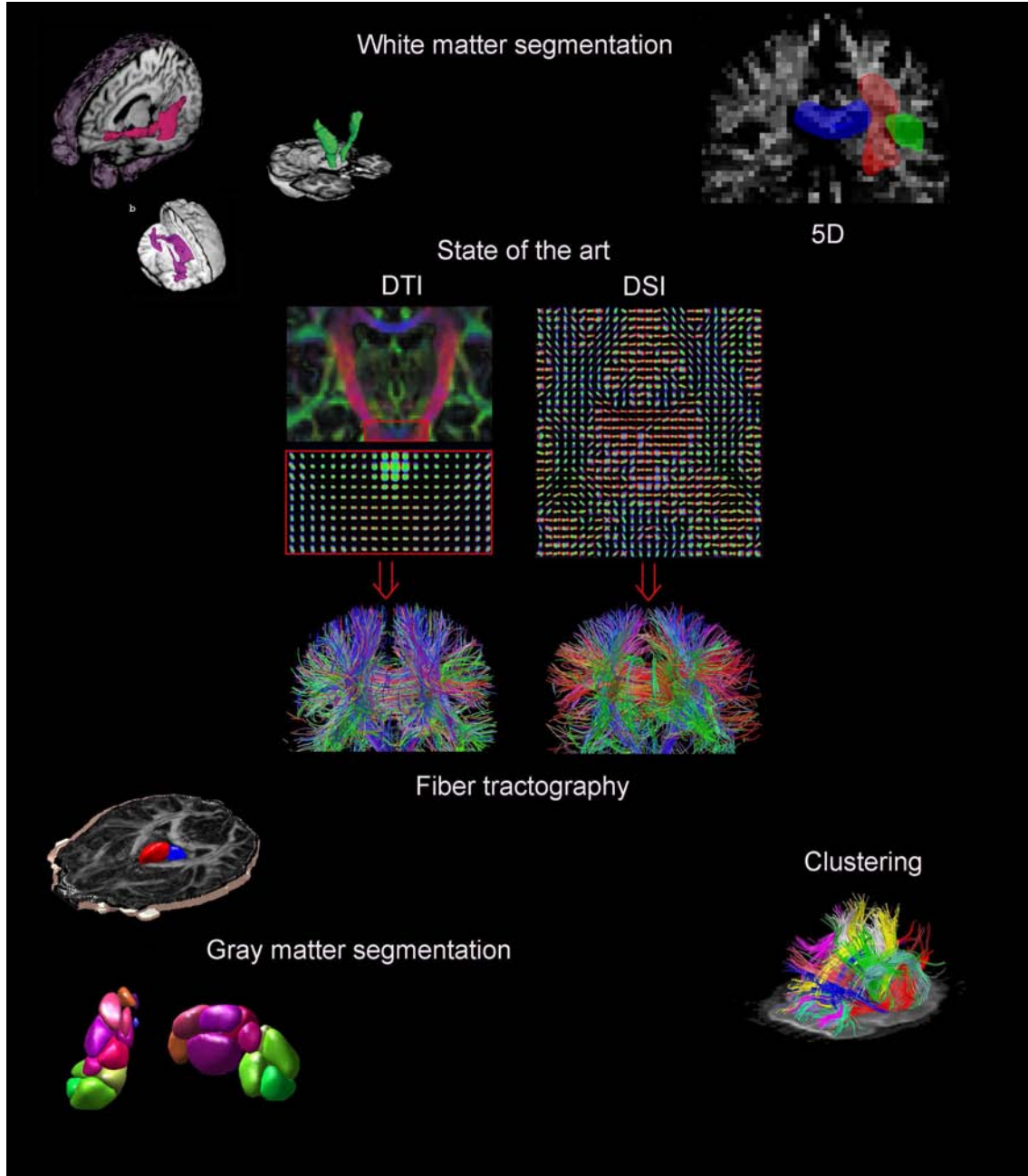


**Figure 1.1:** Figure illustrating our main contributions (corners of the image) in relation to the state-of-the-art (the center of the image). Current state-of-the-art includes image acquisition and fiber tractography from DT-MRI and Diffusion Spectrum Imaging (DSI). From this our four main contributions are derived. Top row shows examples of white matter segmentation where the top left corner is from DT-MRI and top right corner from DSI. Bottom left corner illustrates the gray matter segmentation method we developed for the thalamus and its nuclei. Bottom right corner represents our clustering algorithm for fibers of high angular resolution.

---

Chapter 8 Conclusion, we will here give a resume of our achievements and a discussion of future application and research topics.





---

# MR and Diffusion Imaging

---

# 2

## 2.1 Introduction

We will here introduce the basic principles \* behind the images on which we will apply most of our new methods. First, we will describe the principles behind magnetic resonance imaging (MRI), from the underlying physics to the image acquisition. We will then discuss the self-diffusion of molecules and how it is related to the neuronal architecture of the brain. Diffusion can be measured by an adapted MRI experiment and we will show the connection between the physical principles of diffusion and imaging. We will then present different models of the diffusion, in particular the diffusion tensor (DT) model and the diffusion spectrum imaging (DSI).

Most of the vocabulary that we will use further on will be defined in this chapter as well as in Chapter 4 that will set the mathematical background of the image segmentation method we will adapt. Together, these two chapters present the state-of-the-art.

## 2.2 Magnetic Resonance Imaging

### 2.2.1 Brief history

Imaging human internal organs with exact and non-invasive methods is very important for medical diagnosis, treatment and follow-up as well as for clinical research. Today, one of the most important tools for this purpose is the MRI. MRI scanners are based on the discovery of the nuclear magnetic resonance (NMR) phenomenon that was detected independently by Bloch [18] and Purcell [83] in 1946. They discovered that an atomic nucleus with unpaired protons in a strong magnetic field rotates with a frequency depending on the strength of

---

\*Information collected from [26][67][53]

the magnetic field and the nature of the atom. If it is submitted to a radio frequency (RF) field of this particular frequency, which is the resonance frequency, it absorbs energy and when the RF field is removed this energy is emitted through an electromagnetic wave of the resonance frequency. For this discovery Bloch and Purcell were awarded the Nobel Prize in Physics in 1952 [26].

The MR phenomenon was initially used mainly for studies of the chemical structure of substances. The first two-dimensional magnetic resonance (MR) images were reconstructed in 1973 by Lauterbur [63]. By introducing gradients in the magnetic field he made it possible to determine the origin of the emitted RF-signals. The same year, independently of Lauterbur, Mansfield and Grannell demonstrated the Fourier relationship between the spin density and the NMR signal acquired in the presence of a magnetic field gradient [70]. These discoveries were ground breaking and led to the currently used application of MR in medical imaging. It also led to the Nobel Prize in Medicine for Lauterbur and Mansfield in 2003.

Even more Nobel Prizes [1] have been attributed for discoveries in the field of MR imaging. Richard Ernst was awarded the Nobel Prize in chemistry 1991 for his contributions on further development of the methodology of high resolution nuclear MR spectroscopy in 1975.

The MRI medical scanners have been available since 1980 and since then the use of MR scanners has rapidly increased, in 2002, there were approximately 22 000 in use worldwide, and more than 60 million MRI examinations were performed [53]. Compared with other imaging modalities MR has many advantages, first of all it is non-invasive and to present knowledge has no secondary effects. It provides an amazingly strong imaging contrast between tissues and it can, as we will see in this chapter, be adapted to image other physical phenomena.

Today, the most frequently used MRI method in medicine is the anatomical MRI designed to differentiate tissue structures. It is used for basically any part of the body, brain, knees, arms etc. Another more recent imaging method is the functional MRI (fMRI) for mapping of activation patterns in the brain. This is an important modality for better understanding of function. When a brain region is activated new energy must be transported to this region which leads to an increased blood flow in this part of the brain. This can be imaged by repetitive MR scans and detected by appropriate signal processing methods. In Figure 2.1 results from an fMRI scan is exposed on anatomical MRI scans. In this thesis we will focus on a third modality, the diffusion weighted MRI. This imaging method maps the movement of water molecules in the brain which is dependent on the tissue cytoarchitecture. This is particularly useful in fibrous regions where the diffusion is restricted in coherent direction which give insight in the neuronal connectivity.

### 2.2.2 Physical principles of MRI

Protons, neutrons and electrons have an angular momentum known as spin. Each spin can have the values  $\pm\frac{1}{2}, \frac{3}{2}, \frac{5}{2}, \dots$ . Since spins in atomic nuclei with pair number of protons will

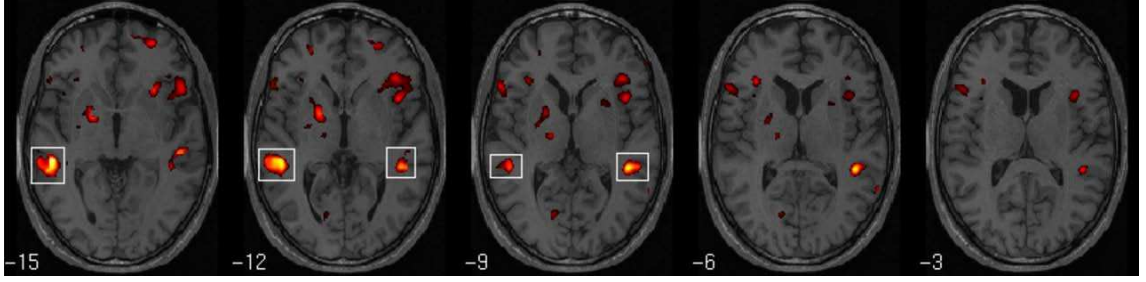


**Figure 2.1:** Examples of two different types of MRI. The background image showing the contrast between different tissue structures is an anatomical MRI. The red zones are activated areas in the brain highlighted by functional MRI.

cancel each other, only atoms with an odd number of protons have a net spin which is necessary for being NMR-active. The most typical nucleus to use in the NMR experiment is the hydrogen nucleus,  $^1H$ , that has the spin states  $\pm\frac{1}{2}$ . Since the signal of one spin is impossible to measure, spins are in general considered as an ensemble and are described in terms of precession around a spin magnetization vector,  $\mathbf{M}$ . When no external field is applied the spins are randomly distributed between the spin up ( $+\frac{1}{2}$ ) and spin down ( $-\frac{1}{2}$ ) position and the net spin of the ensemble of spins therefore equals zero.

In the presence of an external magnetic field  $\mathbf{B}_0$  (a polarizing field), the spin magnetization vector  $\mathbf{M}$  will align itself with the field and the spins start precessing around  $\mathbf{B}_0$ . The frequency of precession is the natural resonance frequency of the spin system. This resonance frequency is known as the Larmor frequency  $\omega_0 = \gamma\mathbf{B}_0$  where  $\gamma$  is the gyromagnetic ratio specific for each kind of nucleus. When considering a spin system we will define a laboratory frame in which  $\mathbf{M}$  appears to be stationary and aligned with  $\mathbf{B}_0$ . The axis along which  $\mathbf{B}_0$  acts, is the longitudinal  $z$ -axis and the plane orthogonal to the  $z$ -axis is the transverse  $xy$ -plane. For a more detailed description see [26][67].

To obtain a measurable signal from the experiment the system must absorb energy that can later be emitted and measured. The absorption of energy is made by exciting the system with another time-varying rotating magnetic field, an RF pulse  $\mathbf{B}_1$ , acting perpendicular to  $\mathbf{B}_0$  and oscillating with the Larmor frequency,  $\omega_0$ . The RF-pulse tilts  $\mathbf{M}$  away from the  $z$ -axis and  $\mathbf{M}$  starts precessing about the rotating  $\mathbf{B}_1$ -field. The tip-angle between  $\mathbf{M}$  and the  $z$ -axis is dependent on the duration of the RF-pulse. For the time,  $\tau$ , the angle is given by  $\alpha = \gamma\mathbf{B}_1\tau$ . The cases  $\alpha = 90^\circ$  and  $\alpha = 180^\circ$  are the most commonly used in NMR-imaging and are called a  $90^\circ$  pulse and a  $180^\circ$  pulse respectively. When the RF-pulse is removed,  $\mathbf{M}$  will fall back to its initial position aligned with  $\mathbf{B}_0$ , this process is called relaxation. It is during the relaxation that the energy that has been added to the system by the RF pulse is emitted and produces an RF signal, the free induction decay (FID). This signal can be measured by an antenna or receiver coil and be interpreted as we will see later, to generate the image.

The relaxation process contains two kinds of relaxations. The spin-lattice (longitudinal) relaxation and the spin-spin (transverse) relaxation. The spin-lattice relaxation process

involves the exchange of energy between the spin-system and the surroundings. The equilibrium state is when the magnetization vector  $\mathbf{M}$  is aligned with the longitudinal  $\mathbf{B}_0$ . The time for the system to reach equilibrium is the spin-lattice relaxation time and is described by the time  $T_1$ . The spin-spin relaxation is the process where spins come to thermal equilibrium with themselves, this is also called the transverse relaxation and it is described by the time  $T_2$ . The difference in the physical properties of the different tissue types is reflected in the relaxation times. It is this mechanism that generates the contrast between different tissue types in imaging ( $T_1$ ,  $T_2$  etc. see Figure 2.2).

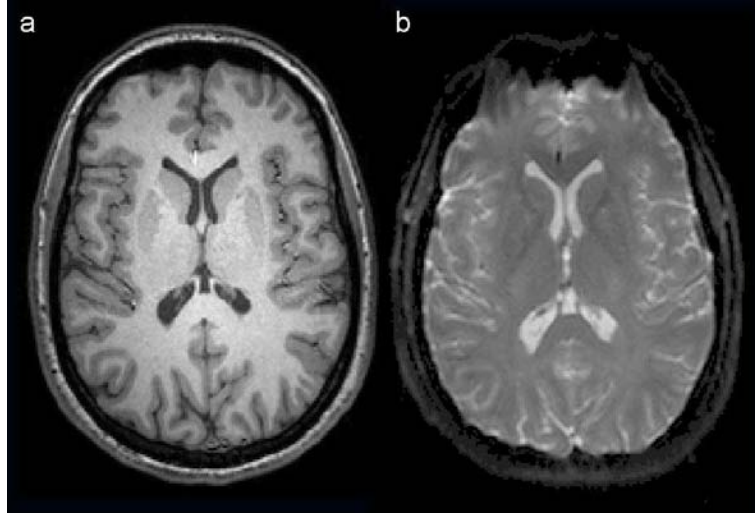


**Figure 2.2:** a)  $T_1$ -weighted MR image. b)  $T_2$ -weighted MR image.

### 2.2.3 Image formation and k-space

As previously mentioned, the Larmor frequency is dependent on the external field,  $\mathbf{B}_0$ . By using a polarizing gradient field  $G_z$  linearly variable along the  $z$ -axis but constant in time, the Larmor frequencies will change depending on its position. Due to this effect, a slice selection can be made by letting  $\mathbf{B}_1$  oscillate with different frequencies dependent on the choice of slice to excite. Linear field gradients along the  $x$  and  $y$ -axis,  $G_x$  and  $G_y$ , are applied to determine position in the transverse  $xy$ -plane. Generally,  $G_y$  is first applied and introduces a phase-shift in the FID-signal dependent on the position along the  $y$ -axis. The phase-shift is due to the difference in frequency that varies with position. It is determined relative to the phase introduced by  $\mathbf{B}_0$ ,  $\gamma\mathbf{B}_0\delta$ . The phase-shift is given by:

$$\varphi = \gamma\delta G_y y, \quad (2.1)$$

where  $\gamma$  is the gyro-magnetic ratio,  $\delta$  is the length of time over which  $G_y$  is applied and  $y$  the position.

When the field gradient is removed the frequencies will return to their initial value but the phase-shifts between nuclei remain at different positions on the  $y$ -axis. Then the field

gradient,  $G_x$  is applied and the frequencies will change again, dependent on their position along the  $x$ -axis. It is normally during the application of  $G_x$  that the signal is detected. The resulting signal after successively applying  $G_z$ ,  $G_y$  and  $G_x$  corresponds to the Fourier-transform of the transversal magnetization  $M_{xy}$ . In order to make the Fourier relation between the signal and the magnetization more obvious a reciprocal spacial frequency space, known as  $\mathbf{k}$ -space, is introduced. The measured signal for a set of gradients,  $G_x$ ,  $G_y$  and  $G_z$ , produces a single line in  $\mathbf{k}$ -space. Applying these gradients in different combinations leads to different samplings of  $\mathbf{k}$ -space. Once  $\mathbf{k}$ -space has been sampled the MR image is obtained by applying the inverse Fourier transform. The above description samples  $\mathbf{k}$ -space for one slice along the  $z$ -axis at a time, see Figure 2.3, but several different techniques for sampling the 3D volume exists, see [26] for more examples.

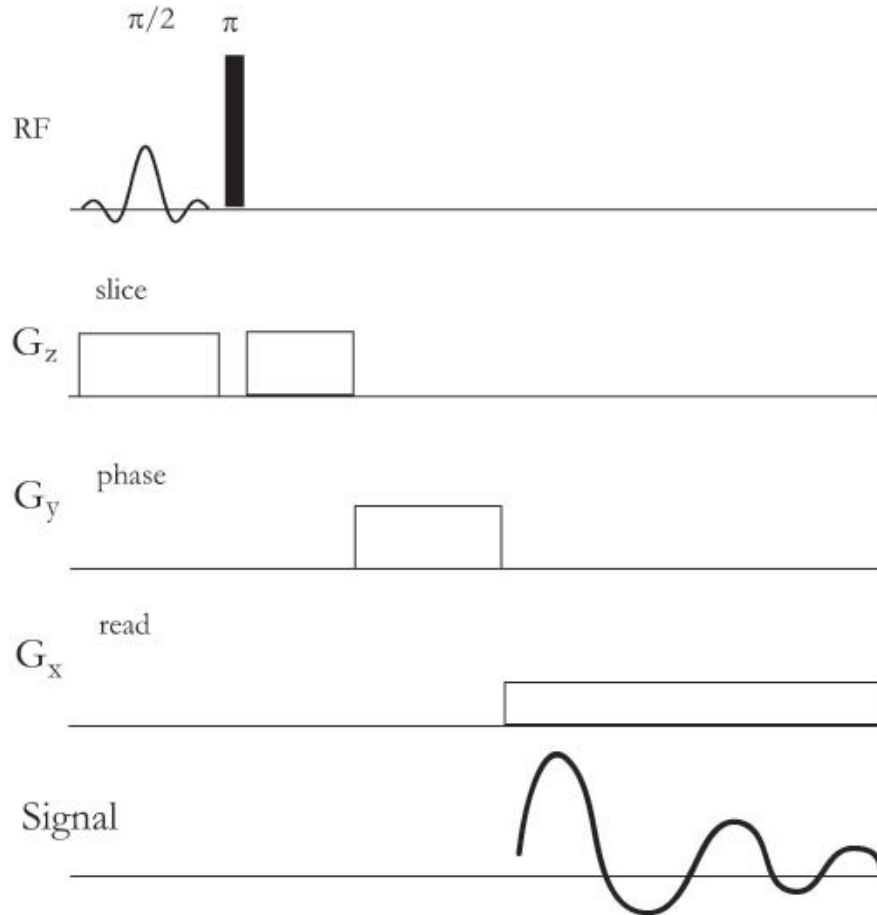


**Figure 2.3:** Schematic figure of a typical imaging sequence for sampling  $\mathbf{k}$ -space. The  $z$ -gradient is responsible for the slice selection and the  $x$ - and  $y$ -gradients are responsible for frequency and phase encoding respectively.

## 2.3 Diffusion Weighted MRI

Water diffusion in living tissues is highly affected by its cellular organization. Axonal cell membrane and myelin sheath are in particular the main components restricting the water mobility [13] as can be seen in Figure 2.4. Imaging the diffusion process in-vivo gives therefore an insight of the microstructure of the tissue. The anisotropic diffusion in fibrous regions can be used for mapping neuronal connectivity and structures invisible in other imaging modalities can be localized due to the information contained in the diffusion. Diffusion imaging is therefore a valuable tool to improve our current knowledge of the brain. Even though diffusion weighted imaging is routinely used in investigations of stroke, more advanced models of the diffusion such as diffusion tensor MRI is rare in most institutions. Other possible clinical applications include investigations of cerebral ischemia, axonal injury, understanding of the developing brain, maturation and aging etc. [90]. In psychiatric research diffusion tensor MRI is used for studies in disorders of cognitive dysfunction, Schizophrenia, alcoholism etc. [93].

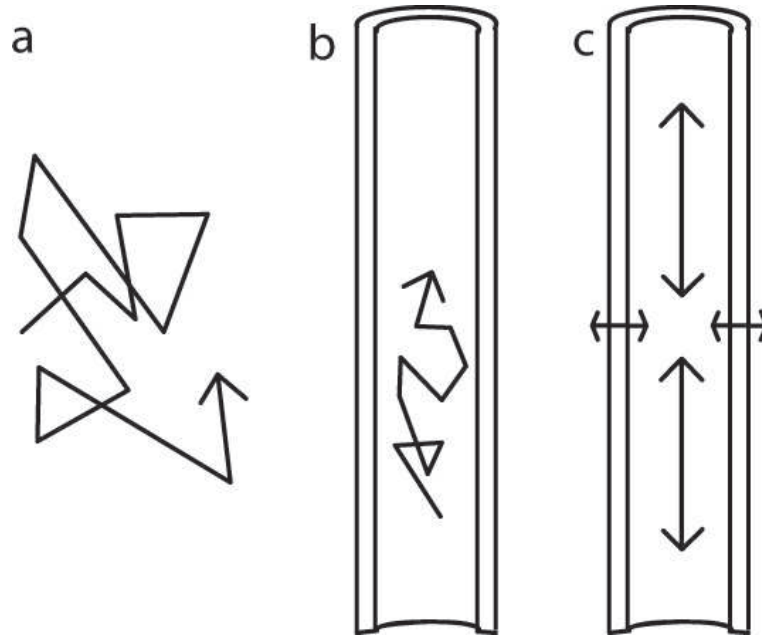


**Figure 2.4:** Axonal cell membrane and myelin sheath are in particular the main components restricting the water mobility. a) The random translational motion of the water molecules is restricted in the axones b). The main diffusion will therefore be along the axones as shown in c)

### 2.3.1 Physical principles of diffusion

Molecules in a medium constantly exhibit a random translational motion, see Figure 2.4a. This phenomenon, known as Brownian motion, is the self-diffusion of the molecules and it is a physical process that was described by Einstein in 1905 [38]. Even though the

random motion for a single particle is impossible to predict it is possible to make statistical predictions about the macroscopic behavior of a large number of molecules. In a free medium the diffusion of the molecules is isotropic and can be modelled by a Gaussian distribution. In this free diffusion the diffusion coefficient is only dependent on the molecular mass, the temperature and the viscosity of the medium. When the diffusion is restricted due to obstacles, the diffusion can no longer be considered Gaussian.

Since the signal in NMR is never detected from one single spin but from a very large number of spins we have a macroscopic description that gives us an ensemble-averaged view of the behavior of the molecules. We can therefore link the diffusion to the measured signal in the MRI experiment by talking in terms of the *ensemble-averaged diffusion propagator*. This is the probability of finding a particle at position  $\mathbf{r}'$  after a time  $t$  given its initial position was at  $\mathbf{r}$ . This is equivalent to the probability of self-diffusion  $P_s(\mathbf{r}' | \mathbf{r}, t)$ . The total probability of finding a particle at position  $\mathbf{r}'$  at time  $t$  is given by:

$$P(\mathbf{r}', t) = \int \rho(\mathbf{r}) P_s(\mathbf{r}' | \mathbf{r}, t) d\mathbf{r}, \quad (2.2)$$

where  $\rho(\mathbf{r})$  is the particle density at position  $\mathbf{r}$ .

### Fick's laws on macroscopic diffusion

The macroscopic behavior of diffusion was modelled in 1855 by Adolf Fick, now known as Fick's first and second law. Fick's first law states the proportionality between the flux and the concentration gradient of the fluid, weighted by the diffusion coefficient. When considering self-diffusion there is no net concentration gradient, so instead of using the concentration we can use the probability of self-diffusion,  $P_s$  from Eq. (2.2) which gives us Fick's first law :

$$J = -D \nabla P_s. \quad (2.3)$$

where  $J$  is the flux and  $D$  the diffusion coefficient. In a closed medium, the number of particles must be conserved. This constraint is described by the *continuity equation* that originally links the rate of change of particle concentration at a point in space with the divergence of the local flux. In terms of  $P_s$  this condition is expressed as:

$$\nabla \cdot J = -\frac{\partial}{\partial t} P_s, \quad (2.4)$$

By differentiating Eq. (2.3) with respect to  $x$  ( $D$  is constant) and combining it with the continuity equation Eq. (2.4) we obtain Fick's second law.

$$\frac{\partial}{\partial t} P_s = D \nabla^2 P_s. \quad (2.5)$$

Fick's second law can be solved for the case of unrestricted diffusion and we obtain the following relation:

$$P_s(\mathbf{r}' | \mathbf{r}, t) = \frac{1}{\sqrt{4\pi Dt}} \exp \left[ -\frac{(\mathbf{r}' - \mathbf{r})^2}{4Dt} \right]. \quad (2.6)$$

We see here that also the macroscopic description predicts a Gaussian behavior in a free medium and it is therefore compatible with the microscopic description provided by Einstein.

### 2.3.2 Image formation and q-space

To image the diffusion we must link the diffusion propagator to the signal measured in the MRI experiment. In 1950 Hahn noted that random thermal motion of the spins in the presence of a magnetic field inhomogeneity would lead to attenuations of the spin echo [50]. To take into account the artefacts this might cause, Torrey modified the Bloch-equations used for describing the magnetization of spins in an NMR experiment. These modified equations are now known as the Bloch-Torrey equations and have become the most fundamental equations in diffusion imaging [95].

The first NMR experiment specifically designed to measure the diffusion was demonstrated in 1965 by Stejskal and Tanner [89]. The experiment is known as the Pulse Gradient Spin Echo (PGSE) and provides a quantitative measurement of diffusion in a sample, see Figure 2.5. The Stejskal-Tanner PGSE experiment uses the effect that spins moving along the gradient direction will experience different field strength and therefore has a different phase depending on their position on the gradient axis. If two pulses acting in the inverse direction of each other are applied, the phase for a static spin will return back to the initial zero-phase but spins that have moved along the gradient direction will experience a phase-shift. Molecules moving in other directions will not experience any change in field strength and therefore not have any phase-shift. A phase-shift of the magnetization vector will lead to an attenuation of the net magnetization measured in the NMR signal and is directly related to the diffusion coefficient for free diffusion through the Bloch-Torrey equations [89]. Stejskal later extended the theory to describe the more general case for any generic diffusion propagator [88].

#### From induced phase-shifts to the MR signal

A schematic figure showing the ideas behind a PGSE can be seen in Figure 2.5. The first gradient applied will introduce a phase-shift according to Eq. (2.1). A  $180^\circ$  RF-pulse is applied before the second gradient and aims at reversing the the phase-shift. This will lead to a total phase-shift of:

$$\varphi = \gamma \delta \mathbf{g}(\mathbf{r}' - \mathbf{r}). \quad (2.7)$$

Here  $\mathbf{g}$  is the applied diffusion gradient,  $\mathbf{r}$  and  $\mathbf{r}'$  are the position vectors for the spins at the first and second gradient pulses and  $(\mathbf{r}' - \mathbf{r})$  is the displacement during the time  $\Delta$ , which is the time between the two gradient pulses. The phase-shift is expressed relative to the polarizing field  $\mathbf{B}_0$ . After both gradients have finished acting the spins fall back to their original positions aligned with  $\mathbf{B}_0$  and an RF-signal is emitted.

The measured phase-shift is proportional to the spin displacement and maps the mean diffusion within a voxel. Due to the millimetric resolution provided by the NMR experiment



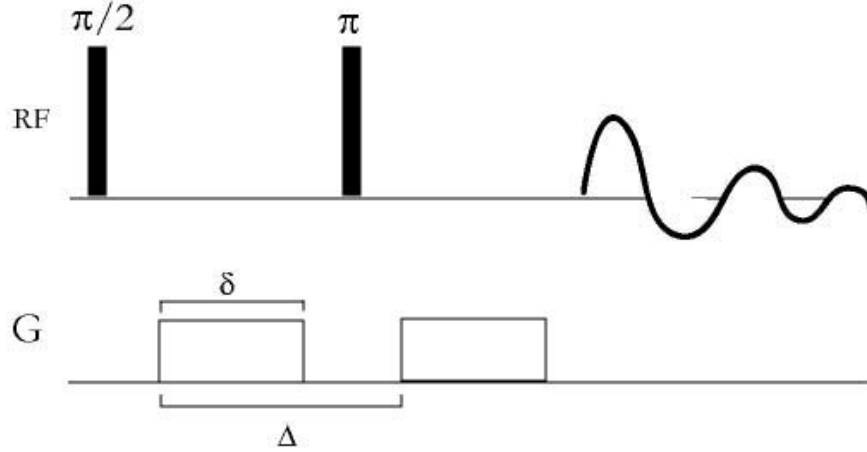


**Figure 2.5:** Schematic figure of a Pulse Gradient Spin Echo (PGSE) sequence for imaging diffusion along one gradient direction. The  $\pi$ -pulse inverses the rotation of the spins and induces a phase-shift dependent on the movement of the spins along the gradient axis. The gradient pulse,  $G$ , is applied in the direction in which the diffusion is measured.  $\Delta$  is the time between two gradient pulses and  $\delta$  is the duration of one gradient pulse. This sequence should be combined with a  $\mathbf{k}$ -space sampling to yield a complete image.

compared to the micro-metric scale of the diffusion it is biologically reasonable to assume that the diffusion between voxels is very small compared to the diffusion within the voxel itself so the inter-voxel effects will be ignored. The mean displacement within a voxel can be considered being the expectation value, or the ensemble average of  $\exp(i\varphi)$  so the measured signal is expressed as:

$$S(\mathbf{g})/S(0) = \langle \exp [i\gamma\delta\mathbf{g}(\mathbf{r}' - \mathbf{r})] \rangle, \quad (2.8)$$

where  $S$  is the measured signal.

#### From the measured signal to the probability density function

Each phase term in Eq. (2.8),  $\exp[i\gamma\delta\mathbf{g}(\mathbf{r}' - \mathbf{r})]$ , is weighted by the probability of a spin being at  $\mathbf{r}$  and move to  $\mathbf{r}'$ . This probability is expressed as the ensemble-averaged diffusion propagator in Eq. (2.2). Hence, the signal can be written as:

$$S(\mathbf{g})/S(0) = \int \rho(\mathbf{r}) \int P_s(\mathbf{r}' | \mathbf{r}, \Delta) \exp [i\gamma\delta\mathbf{g}(\mathbf{r}' - \mathbf{r})] d\mathbf{r} d\mathbf{r}'. \quad (2.9)$$

For the same purpose as the  $\mathbf{k}$ -space was introduced to make the classical MRI experiment more intuitive a reciprocal space,  $\mathbf{q}$ , is defined for imaging diffusion by substituting:

$$\mathbf{q} = \frac{1}{2\pi} \gamma \delta \mathbf{g}.$$

Introducing  $\mathbf{q}$  and substituting  $\mathbf{r}' = \mathbf{r} + \mathbf{R}$ , the signal in Eq. (2.9) can be rewritten as:

$$S(\mathbf{q}) = \int \int \rho(\mathbf{r}) P(\mathbf{r} + \mathbf{R} | \mathbf{r}, \Delta) d\mathbf{r} \exp [i2\pi\mathbf{q} \cdot \mathbf{R}] d\mathbf{R}. \quad (2.10)$$

The ensemble average diffusion propagator is now expressed as a function of the displacement  $\mathbf{R}$ ,  $P(\mathbf{R}, \Delta)$ . The simple inverse Fourier relation between the signal and  $P(\mathbf{R}, \Delta)$  is now evident:

$$S(\mathbf{q}) = \int P(\mathbf{R}, \Delta) \exp[i2\pi\mathbf{q} \cdot \mathbf{R}] d\mathbf{R} = \mathcal{F}^{-1}[P(\mathbf{R}, \Delta)]. \quad (2.11)$$

By measuring the signal for sampled points in  $\mathbf{q}$ -space we can reconstruct the ensemble average diffusion propagator in every voxel.  $\mathbf{q}$ -space is sampled by either varying the diffusion gradient strength,  $\mathbf{g}$ , or the gradient duration,  $\delta$ . Hence the probability distribution is obtained through:

$$P(\mathbf{R}, \Delta) = \mathcal{F}[\| S(\mathbf{q}) \|]. \quad (2.12)$$

It is sufficient to only use the modulus of the signal to obtain the probability distribution, this has been proved in [103]. Examples of diffusion weighted MR images for different gradient directions can be seen in Figure 2.6.

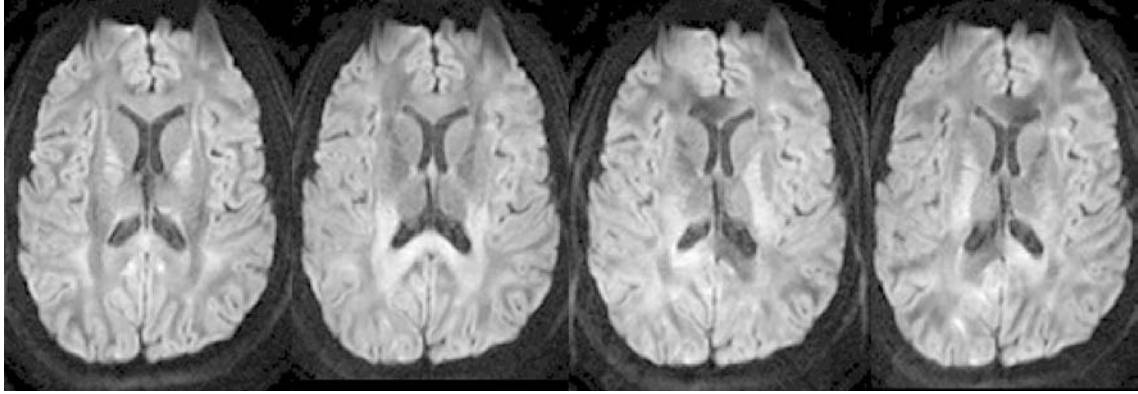


**Figure 2.6:** Diffusion Weighted MRI. Each image shows  $S(\mathbf{q})$ , for different values of  $\mathbf{q}$  obtained by varying the gradient direction,  $\mathbf{g}$  and a constant  $b$ -value. Darker areas correspond to areas of diffusion in the direction of  $\mathbf{g}$  since the signal is the most attenuated in this direction.

### The $b$ -value

In diffusion imaging,  $b$ -values are often used for describing the diffusion sequence that has been used for the image acquisition. The  $b$ -value is defined as:

$$b = \gamma^2 \delta^2 \mathbf{g}^2 \Delta = \mathbf{q}^2 \Delta. \quad (2.13)$$

However, the effective diffusion time is  $\tau = (\Delta - \delta/3)$ , where  $\delta/3$  is a correction due to the diffusion that occurs while the gradient is applied. The movement during the gradient pulse is difficult to detect and the smaller it is the more exact the information about our movement will be. We will therefore try to make the pulse infinitely small so that we can

use the narrow pulse approximation,  $\delta \ll \Delta$ . This improves the signal as the displacement during the gradient pulse is negligibly small.

The  $b$ -value can be variable or constant depending on the desired imaging modality. The  $b$ -value depends on  $\mathbf{q}$  and on the diffusion time  $\Delta$ . Varying these parameters will lead to different properties. A longer diffusion time will for example lead to a better directional resolution. Imagine the diffusion within an axon, for a very short diffusion time there will be a similar amount of diffusion in every direction. When the diffusion time gets longer the diffusion perpendicular to the direction of the axon will reach the axon wall and there will be no more diffusion in that direction whereas in the direction along the axon the diffusion will continue. Thus, a longer diffusion time increases the distinction between the signals in different directions. However, a longer diffusion time will lead to a lower signal-to-noise ratio (SNR) so a compromise is necessary.

### 2.3.3 Diffusion tensor imaging

The diffusion tensor formalism was introduced by Bassar et al. in 1994 [6] [7]. This approach was the first one to provide a unified description of the diffusion from a series of diffusion weighted images. Bassar proposed to fit a second order symmetric tensor to the diffusion data in every voxel. This diffusion tensor (DT) fully characterizes the variation of the diffusion dependent on direction. The DT model is based on the hypothesis that the diffusion is unrestricted and can therefore be modelled by a Gaussian distribution. In biological tissues this assumption is not correct and instead of talking about the true diffusion coefficient we therefore talk about the *apparent diffusion coefficient* (ADC).

In the previous section we saw that the diffusion in a free medium is Gaussian. Isotropic diffusion has a constant diffusion coefficient,  $D$ , but when the diffusion varies with directions it is anisotropic and must be modelled with a tensor,  $\mathbf{D}$ . Thus, the diffusion propagator for anisotropic Gaussian diffusion is:

$$P(\mathbf{R}, \Delta) = \frac{1}{\sqrt{\det |\mathbf{D}|} (4\pi\Delta)^3} \exp \left[ \frac{-\mathbf{R}^T \mathbf{D}^{-1} \mathbf{R}}{4\Delta} \right]. \quad (2.14)$$

In the NMR experiment the signal we measure in free diffusion looks like:

$$S(\mathbf{q})/S(0) = \mathcal{F}^{-1}[P(\mathbf{R}, \Delta)] \propto \exp [-\mathbf{q}^T \mathbf{D} \mathbf{q}]. \quad (2.15)$$

Since the DT is symmetric, six elements have to be determined. This means that the ADC has to be measured in at least six linearly independent directions together with a reference image,  $S_0$ . By varying the gradient directions,  $\mathbf{q}$ , but not their amplitude,  $|\mathbf{q}|$ , in order to keep a constant  $b$ -value, the DT coefficients can be determined for every voxel. More than six directions are often used for a more reliable measurement of the diffusion tensor, the tensor components are obtained by solving the redundant system of equations formed by the signal in Eq. (2.15). When six gradient directions are used the DT can easily be determined using the simplified method proposed by Bassar [11].

### Properties and visualization of the diffusion tensor

The DT is a  $3 \times 3$  symmetric, semi-positive definite matrix. By diagonalizing the DT we obtain the eigenvalues ( $\lambda_1, \lambda_2, \lambda_3$  where  $\lambda_1 \geq \lambda_2 \geq \lambda_3$ ) and the corresponding eigenvectors ( $\mathbf{e}_1, \mathbf{e}_2, \mathbf{e}_3$ ). Since the tensor is symmetric and semi-positive definite the eigenvalues are always non-negative even though noise can destroy the semi-positivity of the DT. The largest eigenvalue and its corresponding eigenvector describe the quantity and direction of the principal diffusion. The DT is normally visualized as an ellipsoid with the principal axes along the eigenvectors and with the length of these axes proportional to the magnitude of the eigenvectors. An anisotropic tensor has a distinct cigar shaped look whereas an isotropic tensor approaches the shape of the sphere. By making a double contraction of an arbitrary unit vector,  $\hat{x}$  with the DT a measure of the diffusion in that direction is obtained:

$$d(\mathbf{x}) = \mathbf{x} \mathbf{D} \mathbf{x}^T. \quad (2.16)$$

By plotting the diffusion for different directions on the sphere we see that the typical shape of a DT is not an ellipsoid but more a peanut shaped fuzz ball as can be seen in Figure 2.7b. A field of fuzz balls can be seen in Figure 2.9. Figure 2.8 shows how diffusion in fibrous regions are represented by the DT model.

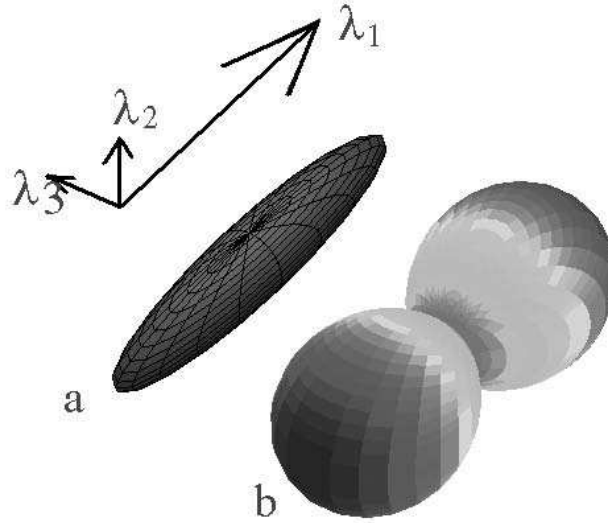


**Figure 2.7:** A diffusion tensor visualized as a) an ellipsoid and b) a fuzz ball. The axes corresponds to the eigenvalues and the principal direction of diffusion is directed along the eigenvector of the largest eigenvalue,  $\lambda_1$ .

The mean diffusivity highlights areas of strong diffusion such as the ventricles, see Figure 2.10a, and it is given by:

$$\langle \mathbf{D} \rangle = \frac{\text{Trace}(\mathbf{D})}{3} = \frac{D_{1,1} + D_{2,2} + D_{3,3}}{3}. \quad (2.17)$$

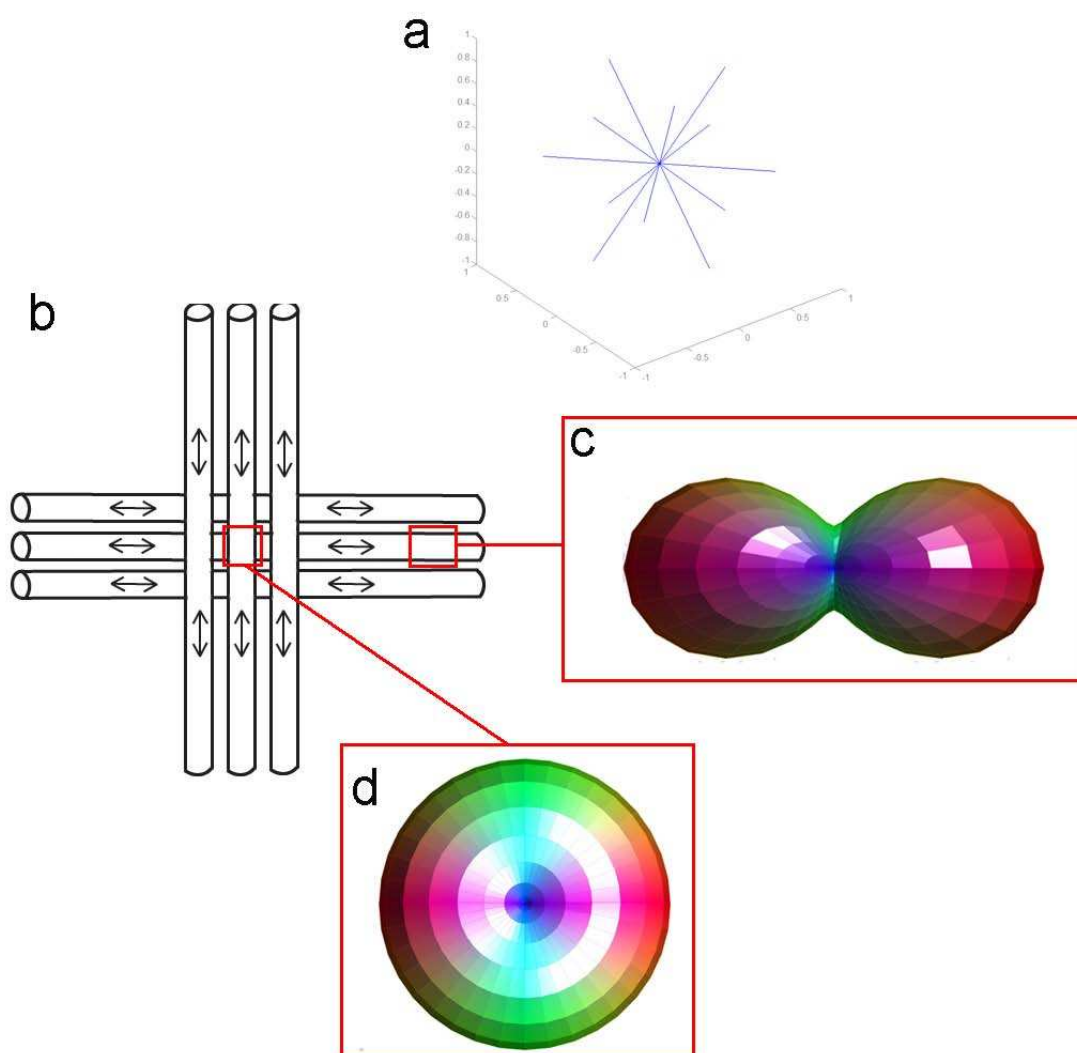


**Figure 2.8:** a) The diffusion tensor (DT) is most commonly obtained by measuring  $S(\mathbf{q})$  in 6 linearly independent directions. b) In fibrous regions the DT represents the diffusion well in highly anisotropic parts c) whereas in fiber crossings d) the angular resolution of the tensor model does not resolve the crossing but will have a planar shape.

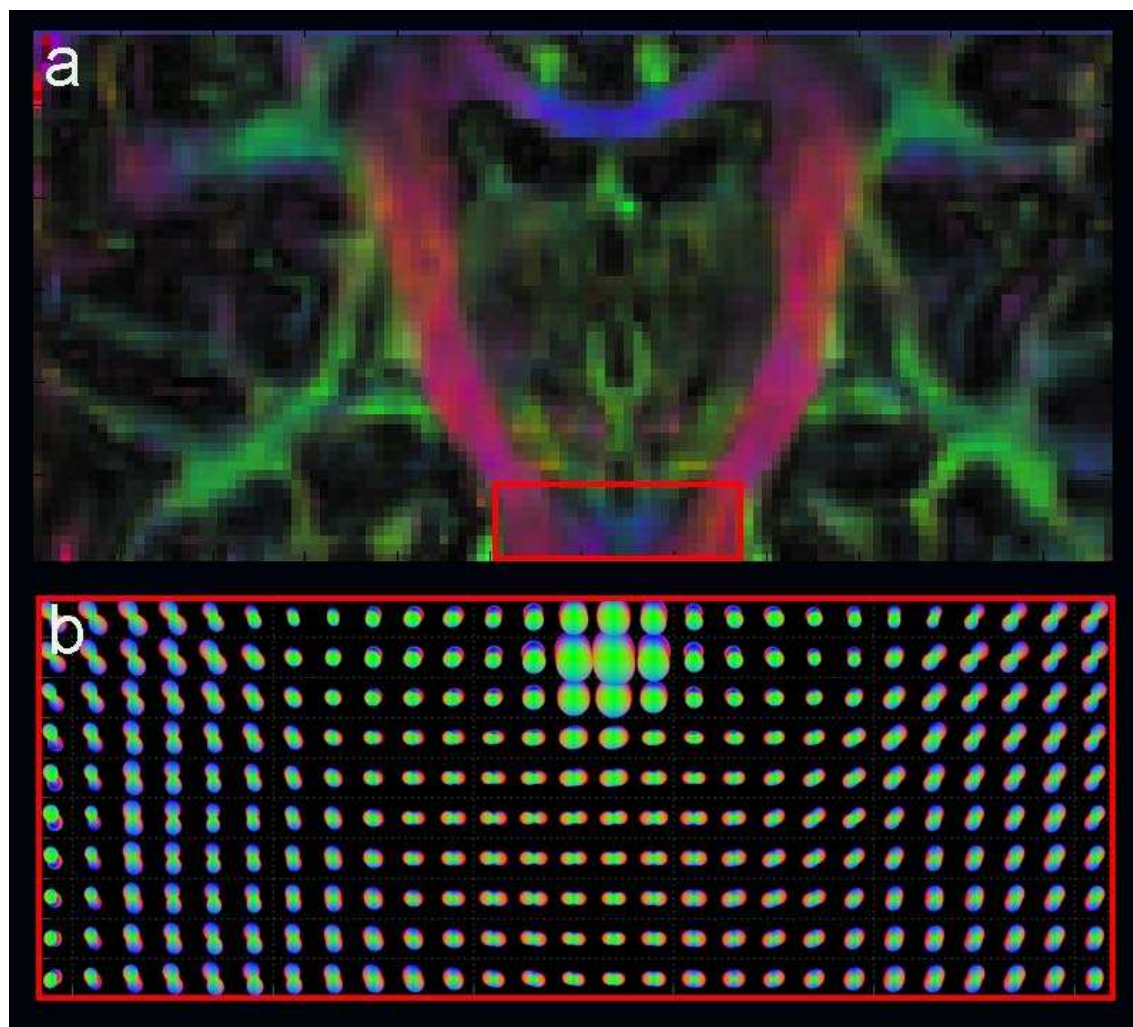


**Figure 2.9:** a) A coronal cut of a color map from a field of DT. b) A field of DT visualized as fuzz balls.

An important property of the DT is the anisotropy which is high in fibrous regions but is low in other regions such as the ventricles. The level of anisotropy is calculated from the eigenvalues and the most commonly used measure is the fractional anisotropy (FA) [10]:

$$\text{FA} = \sqrt{\frac{3}{2}} \sqrt{\frac{(\lambda_1 - \langle \lambda \rangle)^2 + (\lambda_2 - \langle \lambda \rangle)^2 + (\lambda_3 - \langle \lambda \rangle)^2}{\lambda_1^2 + \lambda_2^2 + \lambda_3^2}}, \quad (2.18)$$

where  $\langle \lambda \rangle$  is the average of the eigenvalues. This is a measure of the deviation of the DT from the isotropic case, see Figure 2.10b.

A useful visualization of a tensor field can be obtained by color coding the tensors. The principal direction of diffusion is considered being an RGB-vector in color space so each direction is represented by a color and the intensity is determined by the fractional anisotropy [77], see Figure 2.10c.

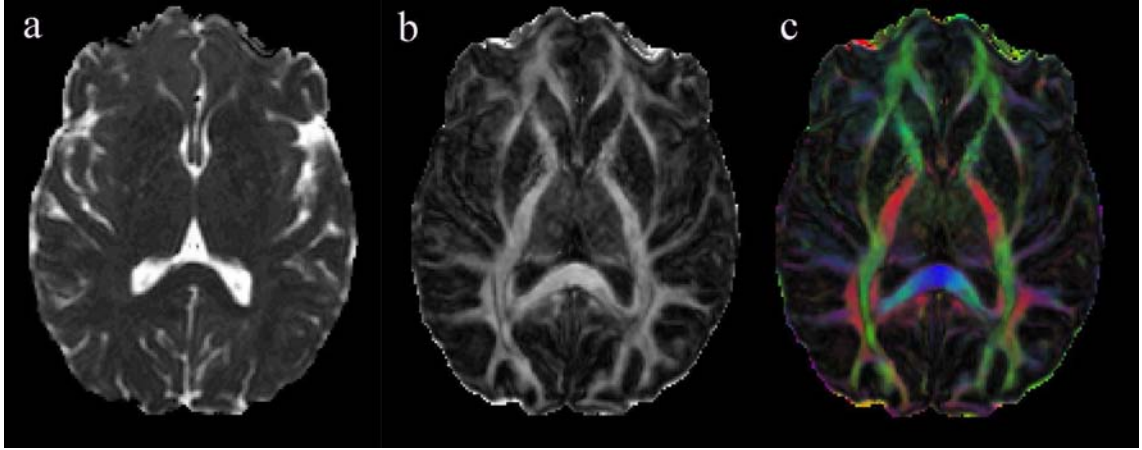


**Figure 2.10:** Visualizations of a DT field using a) Mean diffusion map b) Fractional anisotropy map c) Color map, green color represent fronto-occipital, blue color for transverse and red for cranio-caudal principal diffusion direction.

It can often be useful to compare the diffusion between different compartments. A direct way to do so is to compare the principal directions of diffusion but that leaves out a lot of information contained within the tensor. In Chapter 5 we will present different measures of similarity for comparison with the full diffusion information of the DT.

#### 2.3.4 High angular resolution diffusion imaging

The DT model, which is the most commonly used model today, basically only contains information about anisotropy and principal diffusion and it has limited possibilities to resolve complex brain white matter architectures, particularly in regions with fiber crossings. Augmenting the angular resolution of the diffusion model will help us to resolve the fiber crossings and give us images that more and more resembles the anatomical reality.

### Diffusion Spectrum Imaging

A recent approach, first presented by Wedeen et al. in [104], is the Diffusion Spectrum Imaging (DSI) that provides a full 3D probability density function (PDF) of the diffusion at each location without implying any model of the diffusion. As we have seen in Eq. (2.11), the measured signal is related to the PDF through the inverse Fourier transformation:

$$S(\mathbf{q}) = \int P(\mathbf{R}, \Delta) \exp[i2\pi\mathbf{q} \cdot \mathbf{R}] d\mathbf{R} = \mathcal{F}^{-1}[P(\mathbf{R}, \Delta)]. \quad (2.19)$$

We can therefore obtain the PDF for each voxel by sampling the  $\mathbf{q}$ -space for a very high number of gradient directions and several values of  $b$ , see Figure 2.11b, and then applying the Fourier transform:

$$P(\mathbf{R}, \Delta) = \mathcal{F}[\| S(\mathbf{q}) \|]. \quad (2.20)$$

The PDF provides a detailed description of the diffusion and manages to resolve highly complex organization of fibers such as crossings, see Figure 2.11c. For simplicity the PDF is normally reduced to an orientation density function (ODF), see Figure 2.11d, through a radial projection of the PDF,  $P(\mathbf{R}, \Delta)$  according to:

$$ODF(\mathbf{u}) = Z \int_{\mathbb{R}^+} P(\varsigma\mathbf{u}, \Delta) \varsigma^2 d\varsigma, \quad (2.21)$$

with  $\|\mathbf{u}\| = 1$ ,  $\varsigma\mathbf{u} = \mathbf{R}$  and  $Z$  is a normalization constant.

### Q-ball imaging

Keeping only directional information means that a lot of unnecessary information is acquired during the measurements. With the purpose of reducing the acquisition time, methods for approximating the ODF have appeared. Q-ball imaging [99] is a way of avoiding the measuring of unnecessary information by sampling the diffusion signal directly on the sphere. A function resembling the ODF from the radial projection is then directly reconstructed. The spherical inversion is accomplished by the reciprocal space Funk transform which is a generalization of the Radon transform to the sphere [107]. The inverse of the Radon transform is used to reconstruct images from CT scans. The Funk transform assigns a value to a given point on the sphere, the point can be seen as a pole and the value that is assigned to it is the integral over the associated equator.

Tuch shows in [98] that this Funk transform of the diffusion signal,  $S(\mathbf{q}_j)$ , where  $\mathbf{q}$  is sampled on a sphere, will generate a result that very much resembles the ODF obtained by the radial projection of the PDF.

### Persistent angular structure

Another method for determining the ODF directly from diffusion MRI, proposed by Jansons and Alexander [54], is the persistent angular structure(PAS) MRI. As in q-ball imaging the PAS-MRI is an inversion algorithm that extracts orientational information about the displacement probability function,  $p(x)$ , from a sparse set of measurements. The method



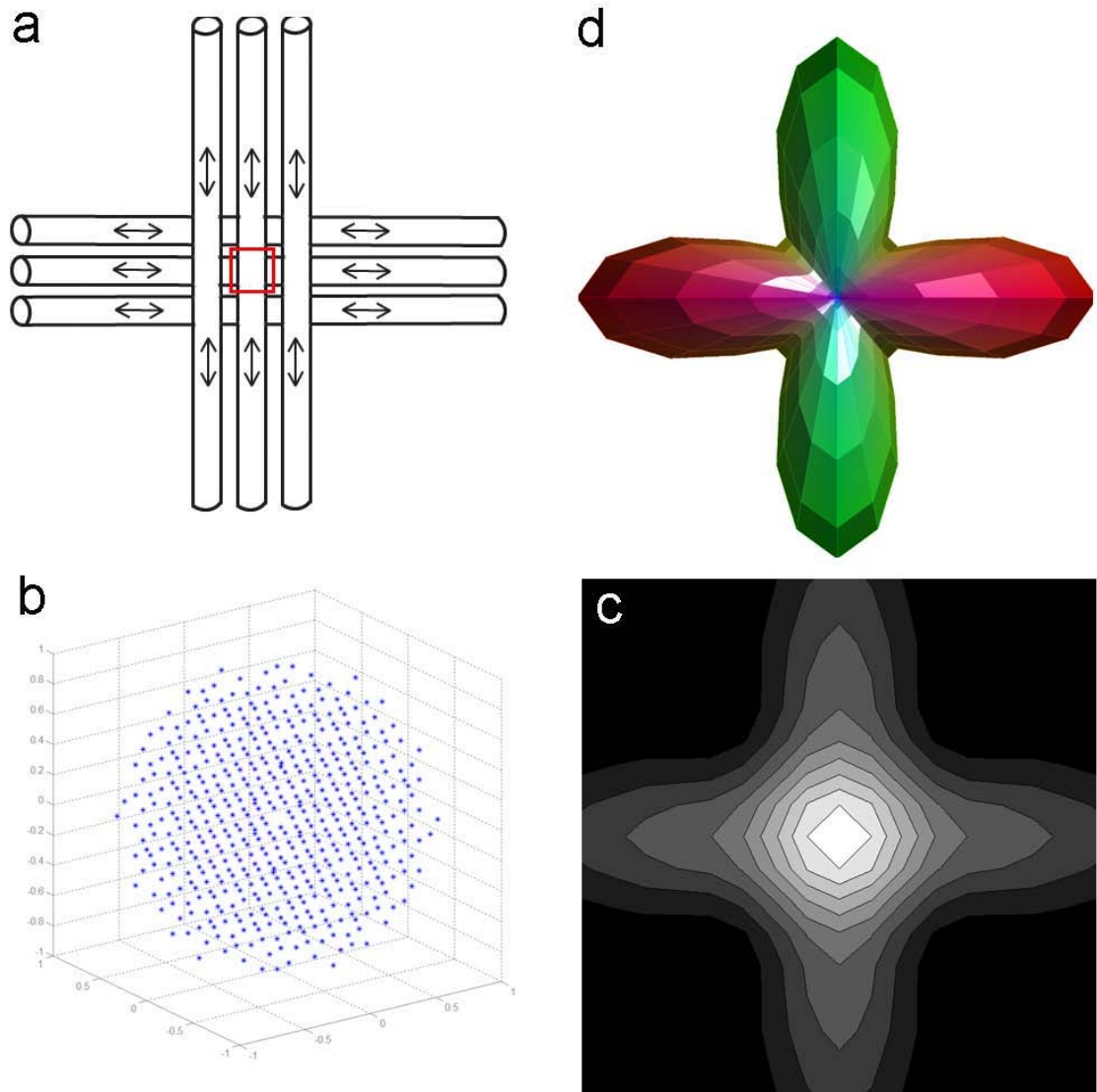


**Figure 2.11:** From diffusion to Orientation Distribution Function (ODF) with DSI. a) Model of a fiber crossing. For the remaining figures, consider one voxel placed in the crossing. b)  $\mathbf{q}$ -space, sampled by measuring  $S(\mathbf{q})$  for various  $\mathbf{q}$  on a 3D grid. c) The Probability Distribution Function (PDF). Obtained by applying the Fourier transform of  $\mathbf{q}$ -space. d) The ODF is obtained through a radial projection of the PDF.

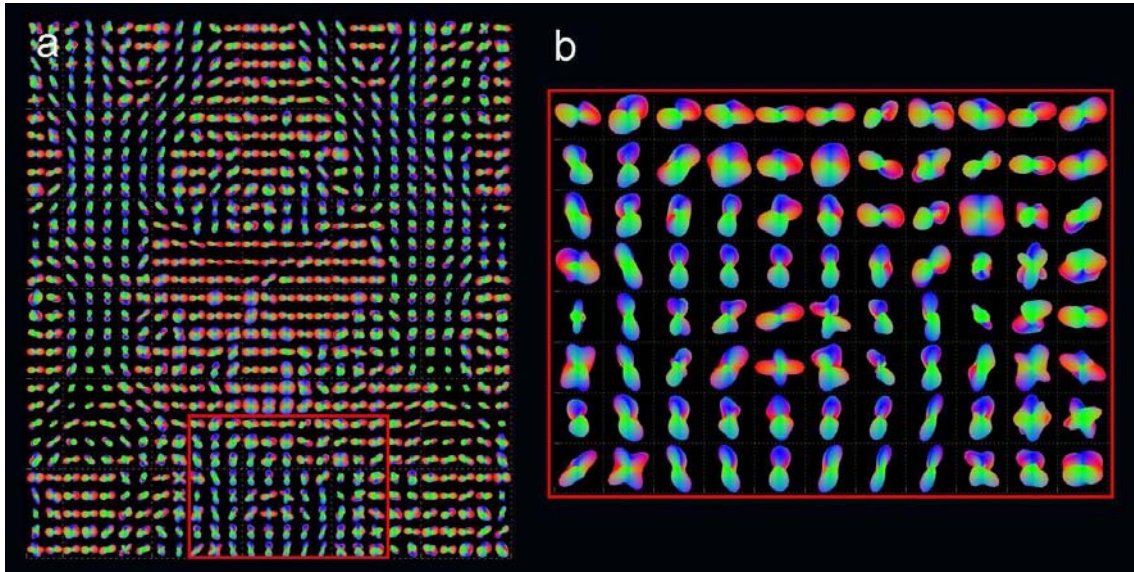


**Figure 2.12:** a) A coronal slice of ODFs of the brain. b) The zoomed region shows a region with many fiber crossings. The HARD data have been obtained from a DSI experiment.

makes the best fit of a function, the ODF, to the points that exist in  $\mathbf{q}$ -space using the inverse Fourier relationship and without adding any extra information.

All these methods are commonly referred to as high angular resolution diffusion (HARD) MRI.

### 2.3.5 Tractography

Fiber tractography is one of the first and most direct interpretations of diffusion weighted images in human brains. Its primary purpose is to reveal the orientational architecture of tissues from the diffusion data by integrating paths of coherent orientation. Fibers obtained through tractography are often viewed as a representation of true axons or nerve fibers but it is more correct to consider them being a contrast mechanism for directional data. This contrast is very informative and interesting for visualization of the human neuronal anatomy, see Figure 2.13.

The connectivity map obtained from tractography will have a different character depending on which imaging modality has been used as diffusion data. Since the DTI is the Gaussian approximation of the true diffusion and its representation as a diffusion tensor is restricted to variations of an ellipsoid it restricts the tractography compared to HARD images where a much higher complexity can be revealed. Deterministic fiber tracking from DTI uses the principal direction of the diffusion to integrate streamlines between voxels [9, 35, 100] but ignores the statistical nature of the DT. To explore this property of the data, Hagmann et al. introduced statistical fiber tracking by considering the tensor as a probability distribution of the diffusion [49].

Fiber tractography on HARDI data, such as DSI or q-ball imaging, results in a large set

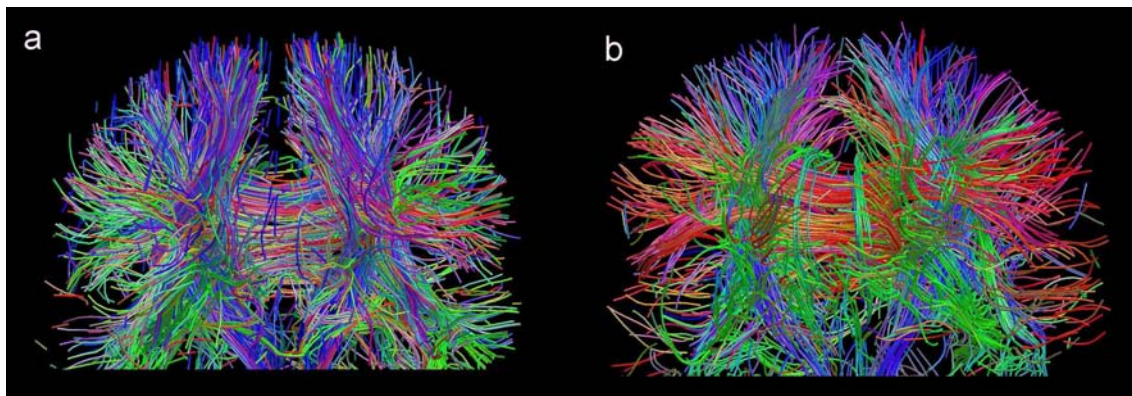


**Figure 2.13:** Fiber tractography. a) DTI data, b) DSI data. All fibers are colored after their principal direction.

of fiber tracts with a very complex geometry. The higher complexity compared to DT-MRI is due to the numerous intersections between fibers that can be resolved, that is to say separated, using HARDI. For DTI, tractography gently starts being used in clinic but there is still a problem with validation and accuracy of the methods.

### 2.3.6 Potential applications

In this chapter we have presented the basics of MRI and how MR can be used for imaging diffusion in-vivo. We briefly discussed the underlying physics of diffusion and how it can be modelled by the DT or HARDI. In current clinical research, DT-MRI is the most frequently used modality. In particular the most simple representation of the diffusion is used such as fractional anisotropy and mean diffusion, see Figure 2.10. These values can indicate changes in white matter due to neurological diseases such as Schizophrenia, Multiple sclerosis, Parkinson and Alzheimer and is also often used for investigating stroke.

An important issue when using diffusion imaging in clinic is the acquisition times. For a reasonable SNR each MR sequence must be repeated numerous times which leads to long acquisition times. As we could see in Section 2.3.3, the diffusion can be measured with only 6 gradient directions which makes it possible to obtain a high quality image within a reasonable time limit, together with an anatomical MRI which is standard to take in clinic, the patient will have to stay approximately 20 minutes in the scanner. As for DSI, the total acquisition time is over one hour which is unfeasible for clinical practise. For an even better SNR even longer scan-times are necessary.

An important problem concerning tractography is how to obtain quantitative measures for comparative studies. This problem is even more present for HARD data where the ODF contain only directional information. In DSI where the whole PDF is present without simplification there are possibilities of quantification and mapping of the fiber density.

What we will present in this thesis is a new way of looking at the information contained in these diffusion images by considering tractography as a segmentation problem. We will also present methods for localization of structures that consist mainly of gray matter that

due to this new imaging modality can be clearly distinct.

---

# A fiber clustering technique for defining tracts

---

# 3

## 3.1 Introduction

Before we tackle the problem of segmenting fiber tracts as a whole we will set its context by defining fiber tracts as bundles of spatially compact and functionally coherent fibers. In this chapter we use fibers obtained from DSI data and present an effective algorithm for clustering of fibers to illustrate how these fiber tracts are defined. The goal is to group fibers into coherent bundles that correspond to the main fiber tracts in the brain. Today, grouping of fibers is often done manually defining regions of interest and selecting all fibers passing through both regions. Such an approach leads to problems of variability and reproducibility. A completely automatic technique for coloring of fiber bundles can therefore be useful for enhancing the imaging contrast provided by the tractography.

Even though fiber bundles can have a distinct orientational separation they intertwine and mix in the 3D position space. To separate these bundles and identify tracts we will use a technique that will prove to be highly appropriate for the characteristics of our data, namely spectral clustering. Spectral clustering techniques are methods that aim at obtaining new data representations to separate clusters with significant overlaps by creating a new feature space in which the clusters are clearly distinct from each other. This new space is constructed from the eigenvectors of a local affinity matrix representing the data and any classical clustering algorithm can then be applied on the eigenvectors [73, 106]. Brand et al. presents in [19] a unifying theory on how this spectral embedding works. Their conclusion is that *"there exists an eigenvector representation which matches the angles between data-points in feature space; as the dimensionality of the representation is reduced, angles between similar points shrink while angles between dissimilar points grow. This highlights the cluster structure of the data and makes segmentation by heuristic methods more likely to succeed."*

Two approaches to clustering of fibers related to spectral segmentation have been made for DT-MRI by Brun et al. [23][24]. In their first approach they use the distance between the end-points of the fibers to generate a weighted graph [23]. They cluster this graph using Laplacian eigenmaps [15]. In their second approach the weighted graph is generated from a pair wise comparison of distance and shape between fibers. This graph can be compared to our affinity matrix. Then, they use normalized cuts to partition the graph by using its second smallest eigenvector and successively subdividing the graph until the desired number of clusters is obtained. Even though authors disagree on which eigenvectors to use and how to derive clusters from them, recent papers on spectral clustering now agree that using more eigenvectors and directly partitioning in the desired number of clusters will improve the results. Weiss et al. [106] argue that more eigenvectors lead to better segmentation.

Our approach to the clustering problem is a simple algorithm for counting the number of intersections between fibers and run a spectral segmentation algorithm on the co-occurrence matrix obtained from the counting. The simplicity of this approach is due to the high angular resolution of the fibers from DSI. The proposed method is an unsupervised clustering technique, applicable for large sets of fiber tracks. Moreover, it is easy to implement and has a low computational cost.

### 3.2 Method

In this method we consider  $N$  fibers, numbered  $1 \leq n \leq N$ . Each fiber,  $n$ , is represented by  $m$  vectors  $\mathbf{v}$  that each represent a point in the space such that:

$$\text{Fiber } n := \{\mathbf{v}_i^n : 1 \leq i \leq m(n)\}, \quad (3.1)$$

where  $m$  is the number of points for fiber  $n$ .

The first step of our algorithm is to create a 3D Euclidean voxel space,  $\mathbf{M}$ , of an appropriate resolution with the voxel side  $\varrho$ . A list of all fibers passing through will be saved in every voxel in  $\mathbf{M}$ . The position in the new space is simply determined by computing  $[v_{i,1}^n/\varrho, v_{i,2}^n/\varrho, v_{i,3}^n/\varrho]$ . At every point in  $\mathbf{M}$  we will then have a list of fibers passing through.

In the second step an  $N$  by  $N$  large co-occurrence matrix,  $\mathbf{A}$ , is created where  $N$  is the number of fibers to cluster, see Figure 3.1.  $\mathbf{A}$  contains the number of times two fibers share the same voxel. Since the number of fibers that we wish to segment is very large this co-occurrence matrix will also be very large. Due to the nature of the DSI data the matrix is also sparse since most of the fibers never cross which makes it possible to handle it in Matlab despite its size. The matrix will be made even sparser by removing the influence of fibers that have only a few voxels in common by setting their values in the co-occurrence matrix to zero. This co-occurrence matrix is the affinity matrix and represents our data set. The affinity matrix resembles what in network theory is known as a weighted graph. The axes of the matrix represent the *nodes* and each entry of the matrix represents the *edges* between the nodes.

Each fiber is then represented by a column vector from our weighted graph. This means that each fiber is described in terms of the fibers it crosses. Considering the nature of our



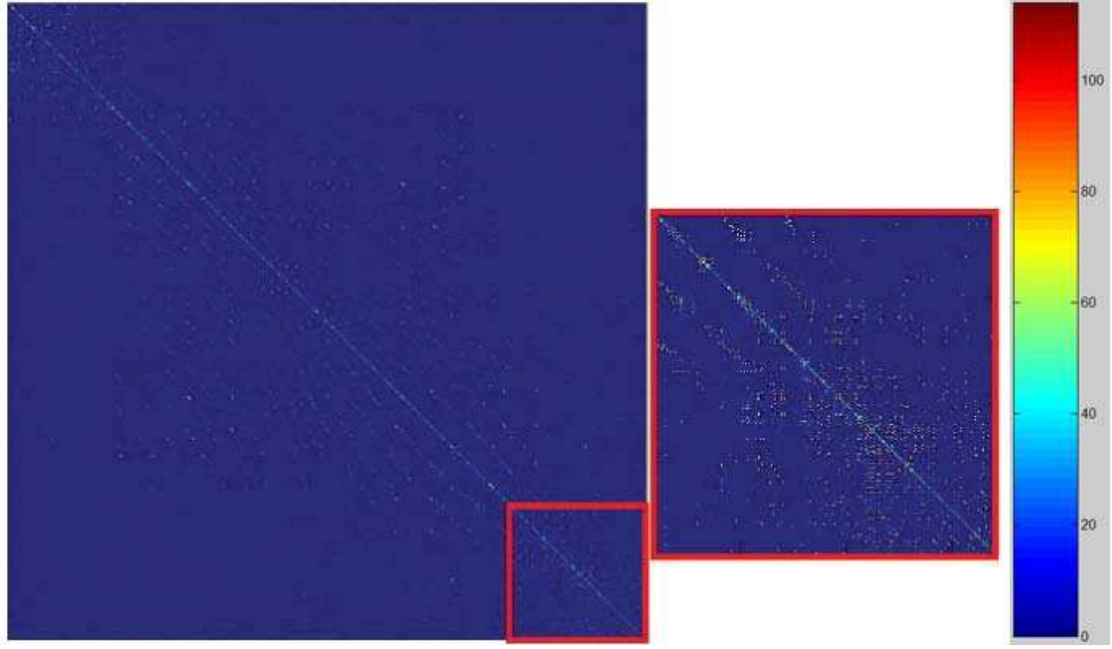


**Figure 3.1:** The affinity matrix,  $\mathbf{A}$ ,  $N$  by  $N$  large where  $N$  is the number of the fibers to cluster.  $\mathbf{A}$  contains the number of times two fibers share the same voxel.

fiber data this description will be highly entangled and it will be hard to group fibers of high resemblance. By applying Principal Component Analysis (PCA) on the weighted graph we project the vector representation of the fibers into an orthogonal subspace in which the fibers become disentangled. Thus, the affinity matrix is decomposed to:

$$\mathbf{A} = \mathbf{V}\mathbf{\Lambda}\mathbf{V}^T$$

As we have seen in Chapter 2, the first eigenvector of the diffusion tensor corresponds to the direction of the principal diffusion. For the affinity matrix, the first eigenvector corresponds to the vector along which the fibers are separated the most. The second eigenvector is orthogonal to the first one and it is the second most important axis in the subspace and so on. We will chose the  $d$  first eigenvectors and call the truncated representation of the eigenvectors  $\mathbf{V}_{(d)}$ . In this new space the fibers can be clearly distinct and grouped using a simple clustering algorithm on  $\mathbf{V}_{(d)}$ . We have used the standard k-means clustering algorithm as implemented in Matlab [17].

### 3.3 Implementation details

The method is extremely simple to implement and the clustering is fully automatic and fast. The limiting number of fibers depends on the size of matrix that Matlab is capable of diagonalizing. So far up to 4000 at a time is no problem. By using the sparse function in Matlab, matrices with up to 8000 times 8000 entries can be treated. However, for these matrices only 6 eigenvalues can be obtained at a time. With only 6 eigenvalues the fibers

are not sufficiently separated to give a satisfying result. More eigenvectors can be obtained iteratively by projection.

---

**Algorithm 3.1:** Fiber clustering with spectral segmentation.

---

- 1: Create Euclidean voxel space,  $\mathbf{M}$ , with voxel size  $\varrho^3$
  - 2:  $\forall i, \forall n: \mathbf{M}(\lfloor \mathbf{v}_i^n / \varrho + 1/2 \rfloor) = \mathbf{M}(\lfloor \mathbf{v}_i^n / \varrho + 1/2 \rfloor) \cup \{n\}$
  - 3:  $\forall i, j, 1 \leq i, j \leq N: A(i, j) := \#\{\mathbf{x} \mid \{i, j\} \subset \mathbf{M}(\mathbf{x})\}$
  - 4:  $\mathbf{A} = \mathbf{V} \mathbf{\Lambda} \mathbf{V}^T$
  - 5: Clusters = k-means( $\mathbf{V}_d$ , noClusters);
- 

When clustering all fibers, the Euclidean space in which the fibers are mapped contains voxels with a side  $\varrho = 2mm$ . To remove the influence of fibers that only have a very few number of voxels in common, all entries of the affinity matrix inferior to 5 is set to zero. When the short fibers are clustered independently, the Euclidean space in which the fibers are mapped contains voxels with a side of  $\varrho = 5mm$  and no fiber crossings are ignored. These values have been determined experimentally.

### 3.4 Data

The method has been tested on a set of fibers obtained from DSI data using a tractography method described in Hagmann et al. [48]. The diffusion images were obtained on a healthy volunteer with a 3T Allegra scanner (Siemens, Erlangen, Germany). We used a twice-refocused spin echo EPI sequence with TR/TE/ = 3000/154/66 ms, bmax = 17000mm<sup>2</sup>/s and a spatial resolution of  $3 \times 3 \times 3mm^3$ . Data were acquired using 515 different diffusion encoding directions sampling on a sphere of radius r=5 grid units. The diffusion data were obtained from Athinoula A. Martinos Center for Biomedical Imaging, Massachusetts General Hospital and the Harvard Medical School, Boston, MA, United States.

### 3.5 Results

The clustering algorithm was tested on a set of fibers containing 17000 fibers. To diminish the size of the affinity matrix every fifth fiber was selected to map back into Euclidean space. In Figure 3.2a all the clusters are displayed except for the cluster that contains what we call the background fibers. This cluster contains all the short fibers that due to the thresholding of the affinity matrix do not have any immediate neighbors. It can be seen in Figure 3.2b. In Figure 3.3 we have selected clusters representing some of the fiber tracts that we will segment directly from the DTI in the next chapter.

By looking at the histograms of the fiber lengths in Figure 3.4 for all the clustered



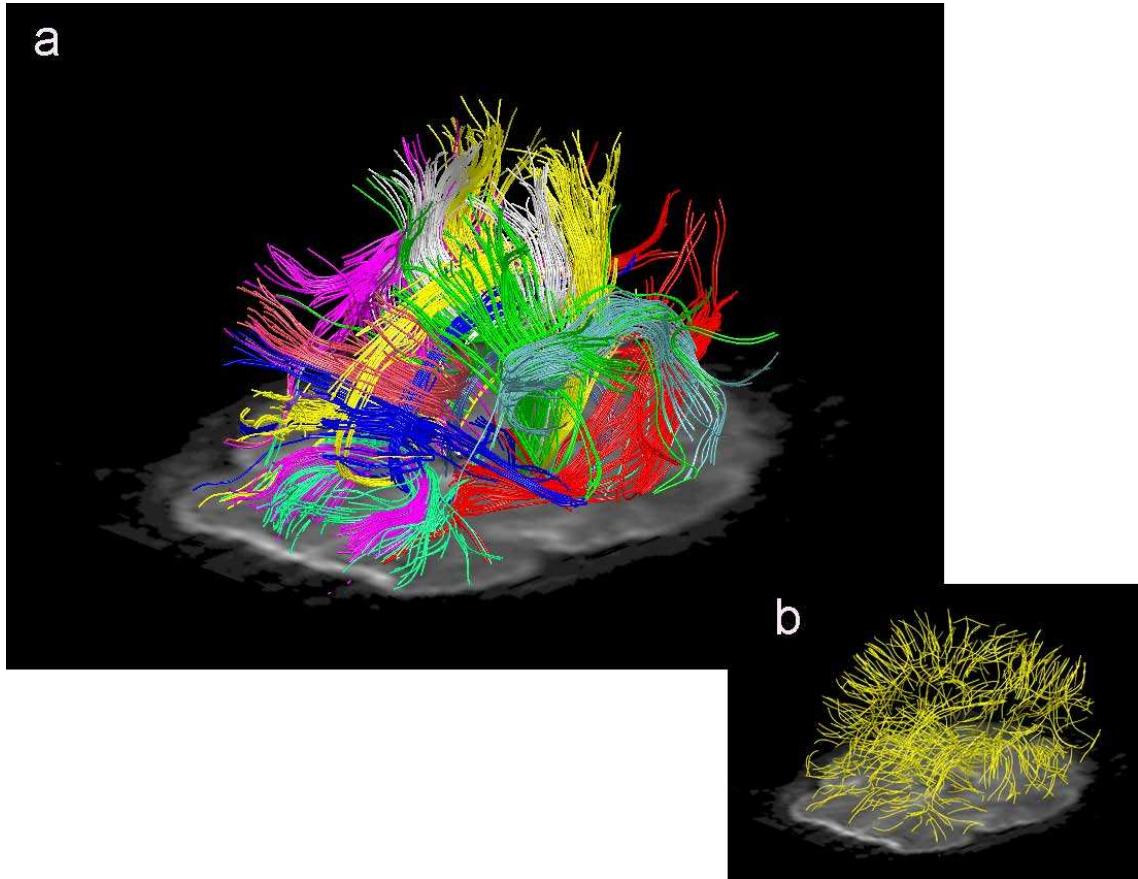


**Figure 3.2:** Clustering of every fifth fiber from the output of a fiber tractography algorithm into 20 clusters. a) All clusters except for the background cluster. b) The cluster of background fibers contains the short fibers that due to the removal of values inferior to 5 in the affinity matrix, do not belong to specific clusters.

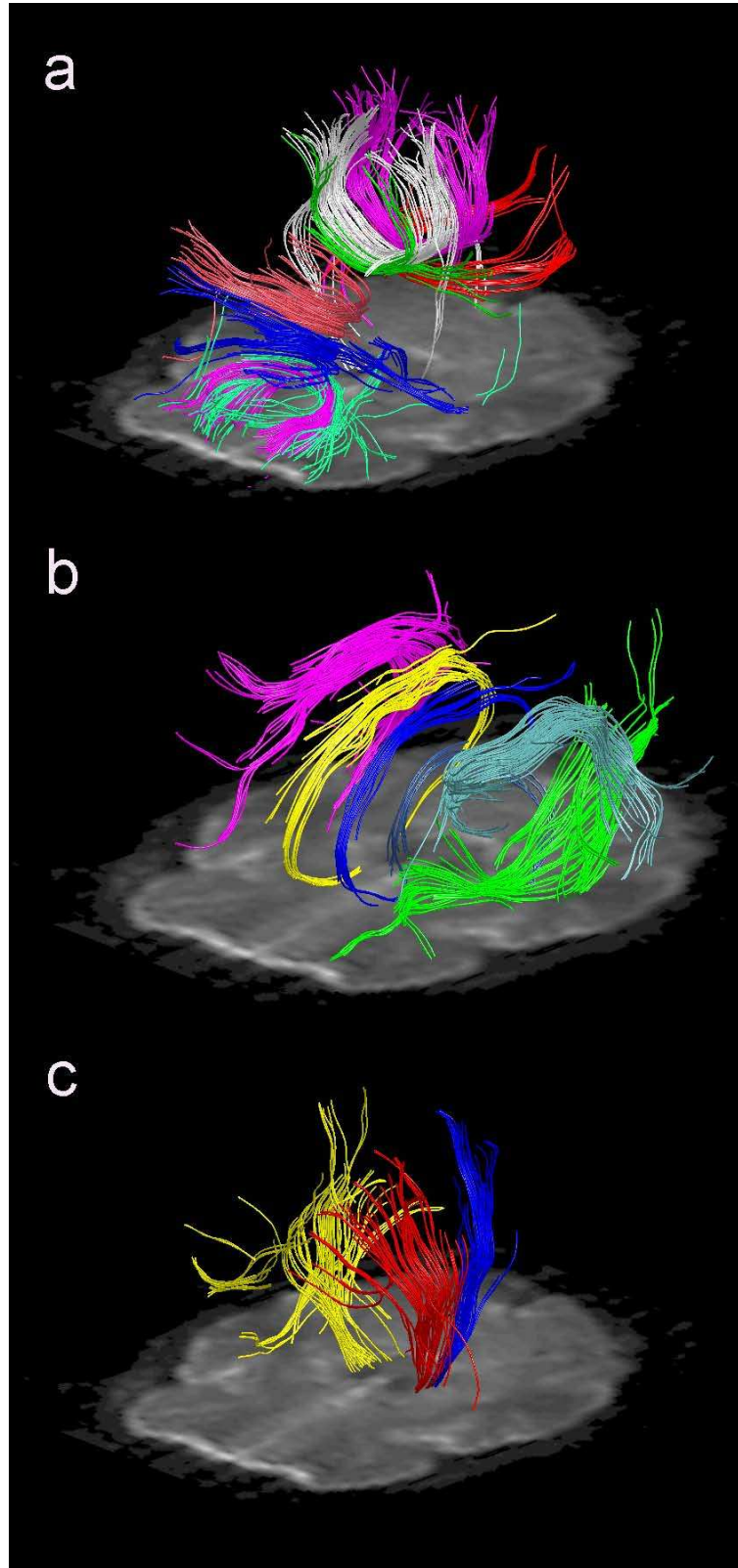


**Figure 3.3:** Clustering of every fifth fiber from the output of a fiber tractography algorithm into 20 clusters. Every fifth fiber on both hemi-spheres were used. a) The corpus callosum. b) Long association fibers. c) Cortico spinal tract.

fibers compared to the background fibers, we see that the length of the background fibers are mainly inferior to 15 points ( $m \leq 15$ ). We will therefore treat these fibers separately. The reason that they have ended up in the cluster of background fibers is because they are short and that they do not share enough voxels with their neighbors. Since the size of the affinity matrix is a limitation of the method we can augment the density of the short fibers by removing fibers longer than 15 points and use only fibers on one hemisphere. We also remove the thresholding of the affinity matrix. The remaining treatment rests the same. The results of the clustering for the short fibers can be seen in Figure 3.5.

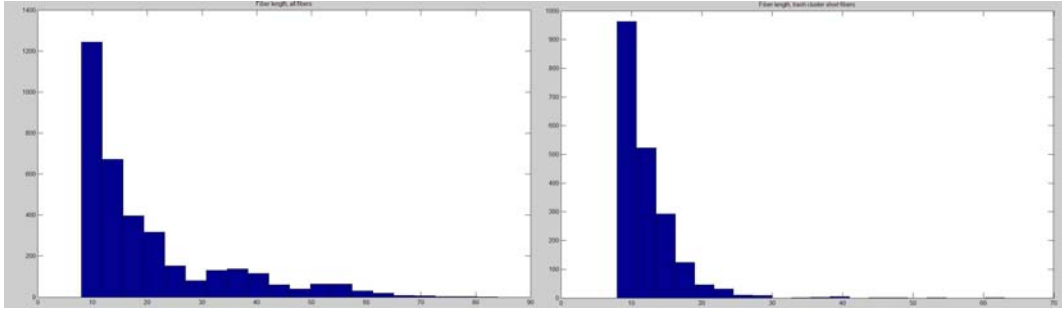


**Figure 3.4:** Histogram of the fiber lengths (in points). Every fifth fiber from the output of a fiber tractography algorithm have been used. a) Histogram of the fiber lengths for the entire set of fibers used in the clustering algorithm. b) Histogram of the fiber lengths of the 'trash' cluster.

### 3.6 Discussion and Conclusion

We have shown an example of the capability of spectral clustering to segment fibers that intertwine in position space and also showed evidence of their orientational separation. This unsupervised segmentation technique is a first step towards a quantitative analysis of the fiber tracts from HARD data which will improve the comprehension of connectivity in anatomical structures. The higher orientational resolution that HARDI provides allows us to use a very simple approach to obtain our affinity matrix. The sparseness of the affinity matrix is a consequence of this and is important for several reasons. Most importantly, the sparseness gives a sense to our counting procedure. With a lower angular resolution numerous fibers would have several intersecting points in common without belonging to the same tract; this is one reason for which this counting procedure will most probably not work for DT-MRI. Methods for clustering fibers from DT-MRI have previously been presented [24][23]. They mostly rely on pairwise similarity between fibers which include defining appropriate distances between fibers, both concerning shape and Euclidean distance. Defining these similarity measures is obviously a much more challenging task than simply counting the intersection points.

What we see in this chapter is also how fibers can be bundled together in groups that correspond to the main fiber tracts in the brain. In the following chapter we will segment

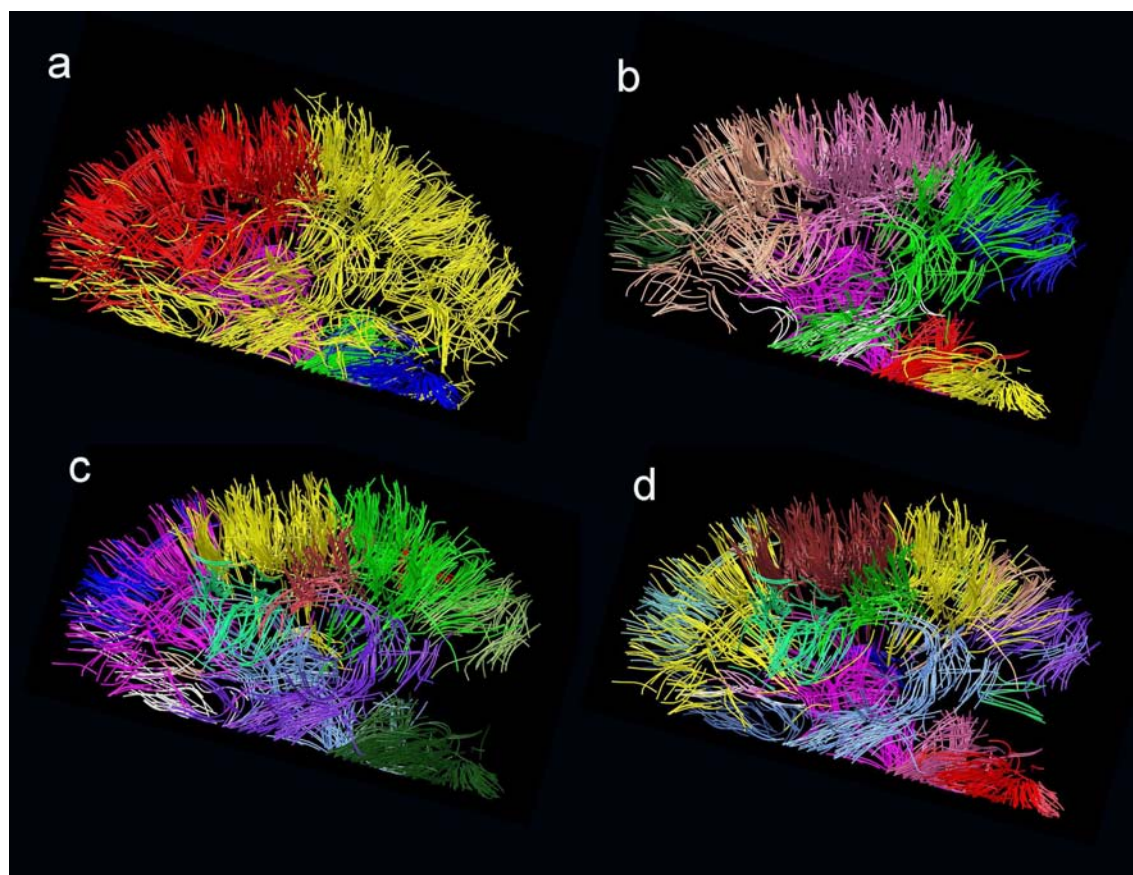


**Figure 3.5:** Clustering of short fibers inferior to a length of 15 points. All fibers on the left hemisphere was used. a) 5 clusters b) 10 clusters c) 15 clusters. d) 20 clusters.

---

the main fiber tracts directly from DT-MRI without using fiber tractography. Segmenting the fiber tracts as a whole is very useful for quantitative analysis of the diffusion in these important structures of the brain.

The work presented in this chapter has been presented in [58].



---

# Image segmentation with the level set method

---

# 4

## 4.1 Introduction

Since the level set method was first introduced by Osher and Sethian [75, 76, 87] it has become a more and more popular theoretical and numerical framework within image processing, fluid mechanics, graphics, computer vision etc. The level set method is basically used for tracking moving fronts by considering the front as the zero level set of an embedding function, called the level set function. In physics, numerous phenomena can be modelled with moving fronts propagated using a curvature dependent speed such as for example crystal growth, flame and wave propagation, only to mention a few. Other possible applications are optimal path planning and noise removal.

In image analysis it has become a widely used tool for segmentation. Dependent on how the propagation speed of the front is defined, many features can be considered simultaneously such as edges, region statistics and shape and any kind of multidimensional data. Consideration of a priori knowledge of shape for segmentation of partly occluded objects [21] [22] and texture segmentation [20] are some other recent and very interesting approaches, see Figure 4.1. Examples of handling of multidimensional data are segmentation of color images [85] and now the very recent approach of tensor segmentation, that is presented in this thesis and has been published in [57][55] [56] [60].

These numerous possibilities constitute some of the many reasons why this framework have been chosen when tackling the segmentation problem for our multi-valued diffusion images (see Chapter 2). Compared to other powerful methods such as Markov Random Fields [43][44] which is a statistical approach for region based segmentation, the level set method provides the possibility of including several properties when formulating the problem. Moreover, having a front that can be smoothed automatically leads to a regularization of the segmentation and a more visually compelling result. The level set method also has



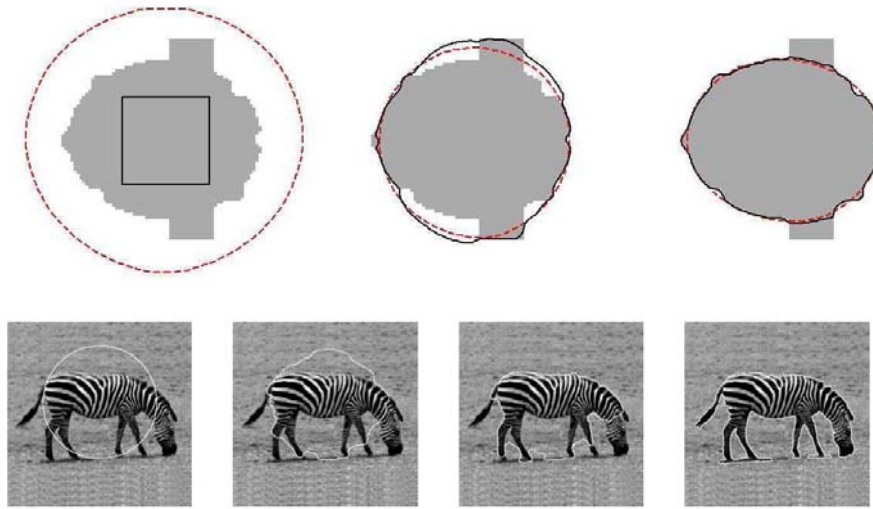


**Figure 4.1:** Examples of the power of the level sets as a segmentation tool. The first row shows the use of shape prior for segmentation of a partly occluded object. It shows the evolution of the active contour (solid line) with an a priori knowledge of its shape (the dotted line) [21] [22]. The second row shows the segmentation of objects with complex textures using information theory [20].

a sub-voxel precision in its segmentation, a property that very few segmentation methods provide. However, some drawbacks exist such as long computation times and sensitivity to initial conditions. The latter can be resolved by hybrid techniques by coupling this high precision method with more large scale segmentation tools.

This chapter aims at presenting the basic concepts of level set theory and showing a few examples of how to define propagation speeds from physical properties of the image. The examples presented are oriented towards detection of boundaries and regions.

## 4.2 The Level Set Method

The level set method is a theoretical and numerical tool for moving any kind of implicitly represented surfaces or interfaces. The method is based on theories borrowed from mechanics on hyperbolic conservation laws and especially properties of Hamilton-Jacobi equations. In mechanics, these theories are since long well developed and by adapting the same framework for the level set theory many practical problems of moving fronts have already been solved. Examples of potential problems that can occur when propagating fronts are irregularities of the moving interface. This is solved theoretically using the theory of viscosity solutions and numerically by using schemes based on hyperbolic conservation laws. We will briefly discuss some of these questions later but for more details about these relations we refer to [87].

The idea of the level set method is to consider the moving interface as the set of zero-



values of an embedding function  $\phi$ . Such an implicit representation has numerous advantages over a parametrical approach. The most striking example is topological changes occurring during the propagation, typically when two flames burn together the evolving interfaces merge into one single propagating front. In Figure 4.2 it is shown how the level set method practically handles topology changes. The initial curve, seen as a magenta colored line at the zeroth position of the embedding function, seen in Figure 4.2a, will deform and split into two curves, Figure 4.2c, without changing topology of the embedding level set. Several numerical advantages such as the easy computation of normals and curvatures are also due to the level set implementation. Later it will be seen that these computations will play a major role in the front propagation.

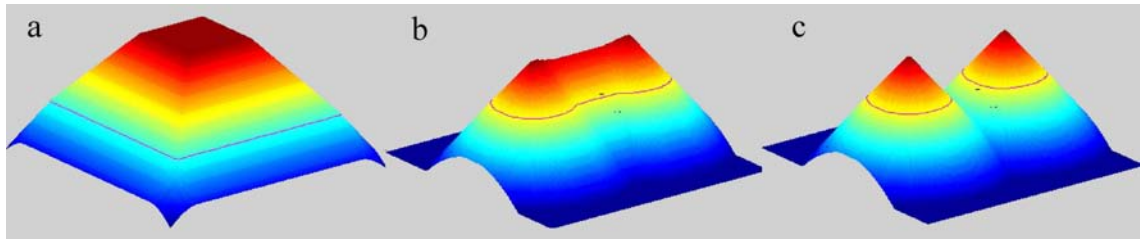


**Figure 4.2:** Example of the level set principle for a curve in 2D. The propagating curve is the magenta colored line and the pyramid formed function is its level set. The curve will change shape as the level set evolves. Between b) and c) the curve has split into two curves whereas the topology of the level set remains.

The level set method can be applied to any kind of problem where an interface is moving with a speed  $F$  defined on every point, see Figure 4.3.  $F$  can depend on any kind of complex physics, such as heating or fluid mechanic effects. This thesis will treat the problem of finding a suitable  $F$  to use when segmenting multi-valued images, in particular tensor images.

#### 4.2.1 The level set equation

For now, let us assume that  $F$  is known. Consider an interface,  $\Gamma$  that can be a curve, surface, hyper-surface in  $\mathbb{R}^N$ , as a boundary between two regions, one inside the boundary and another one outside the boundary. A level set function is constructed around the interface that constitutes the zero value of the embedding function,  $\phi$ , as can be seen in Figure 4.4. All other points of the level set function have the value of the distance from that point to the closest point on the boundary. The distance is positive if this point is situated on the outside of the bounded area and negative if it is situated on the inside. The level set function will change with time according to the speed  $F$  and the interface is always constituted by the points where the level set function equals zero. The interface,  $\Gamma$ , embedded by the level set function,  $\phi$ , can be expressed as:

$$\Gamma(t) := \{\mathbf{x}(t) \mid \phi(\mathbf{x}(t), t) = 0\}, \quad (4.1)$$

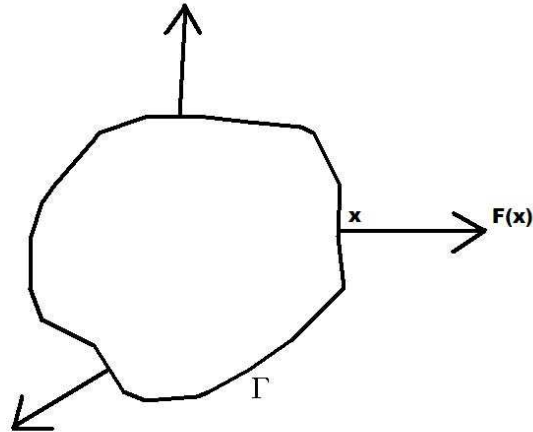


**Figure 4.3:** The level set method can be applied to any kind of problem whenever an interface,  $\Gamma$ , here represented as a curve in  $\mathbb{R}^2$ , is moving with a speed  $F$  defined on every point of the interface.  $F$  can be dependent on external properties, such as complex physical properties or images, and on intrinsic properties of the curve itself.

where  $t$  being the time and  $\mathbf{x}(t)$  are the points of  $\phi$ .  $\phi < 0$  for points lying *inside* the surface and  $\phi \geq 0$  for points lying *outside* the surface.

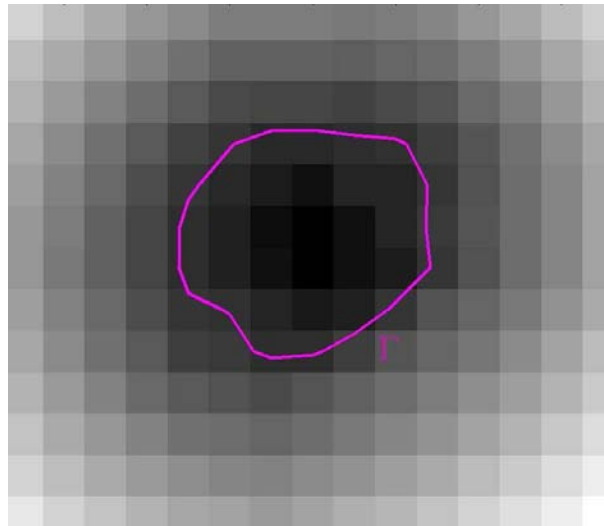


**Figure 4.4:** The interface,  $\Gamma$ , here represented as a curve in  $\mathbb{R}^2$ , is embedded in a level set function,  $\phi$ , and it is constituted of all points where the value of the level set function is zero  $\Gamma(t) := \{\mathbf{x}(t) \mid \phi(\mathbf{x}(t), t) = 0\}$ .

Computing the time derivative of the level set  $\phi(\mathbf{x}(t), t)$  by using the chain rule gives us:

$$\frac{\partial \phi}{\partial t} + \nabla \phi(\mathbf{x}(t), t) \cdot \frac{d\mathbf{x}}{dt} = 0. \quad (4.2)$$

where  $\nabla$  is the gradient operator.

We introduce  $F$  as the speed in the outward normal direction such that  $F = (dx/dt) \cdot \mathbf{n}$  where  $\mathbf{n} = \nabla\phi / |\nabla\phi|$ . If the initial level set function is known,  $\phi(\mathbf{x}, t = 0)$ , the level set equation becomes:

$$\frac{\partial\phi}{\partial t} + F |\nabla\phi| = 0. \quad (4.3)$$

This partial differential equation (PDE) will propagate the boundary towards the optimal solution. For certain choices of  $F$ , Eq. (4.3) corresponds to a Hamilton-Jacobi equation. The property of being a Hamilton-Jacobi is used when studying the existence and uniqueness of the solutions and designing stable numerical schemes.

When interfaces propagate, sharp corners and other phenomenon such as 'swallow-tails' [87], can easily be formed. These artefacts cause problems since their derivatives can not be determined. To deal with this problem the sharp corners are smoothed out by letting the interfaces move under curvature.

For the special case:

$$F = -\nabla \cdot \left( \frac{\nabla\phi}{|\nabla\phi|} \right), \quad (4.4)$$

where  $\nabla \cdot$  is the divergence operator, we have that  $F$  is the mean curvature of the level sets of  $\phi$ . With this definition of  $F$ , Eq. (4.3) becomes a pure mean curvature flow which is a thoroughly studied case [4] [76]. Curvature will be further discussed in Section 4.2.2.

In image processing the level set method is most frequently used as a segmentation tool through propagation of a contour by using the properties of the image. One of the first applications was to detect edges in an image [28], but in more recent applications textures, shapes, colors etc can be detected. The level set theory was initially used for two dimensional images but its general formulation makes it possible to use for images of  $N$  dimensions. The theoretical extension to 3D is commonly used and even though some of the properties of the 2D curves, such as the property of shrinking to a point under curvature flow, do not hold in the 3D case, the main part of the theory remains valid and works well for segmentation of 3D objects [29]. The extension to even higher dimensions is theoretically straightforward but has some practical complications as we will see in Chapter 6.

### 4.2.2 Curvature

In this section all fronts considered are of codimension one. This means that the front is embedded in a space of one superior dimension. This is the case for a curve in a two dimensional space, a surface in a three dimensional space etc. A curve lying in a 3D space is of codimension two. The general case of curvature in arbitrary codimension is treated in [4]. The curvatures that will be treated here are the principal curvatures, mean curvature and Gaussian curvature. A two-dimensional surface can be curved differently in different directions, this is described by the principal curvatures. A cylinder has one curvature defined radially and another defined axially. The radially dependent curvature is the maximum principal curvature  $\kappa_1 = 1/R$  ( $R$ =radius of the cylinder) and the axially defined curvature is the minimum principal curvature  $\kappa_2 = 0$ .

From the principal curvatures mean curvature and Gaussian curvature is defined. The Gaussian curvature is intrinsic, that means that it is dependent only on itself and determines whether a surface is locally convex or locally saddle. The Gaussian curvature,  $\mathcal{G}$ , can be expressed in terms of the principal curvatures,  $\kappa_n$  as:

$$\mathcal{G} = \kappa_1 \kappa_2 \dots \kappa_N. \quad (4.5)$$

Mean curvature is extrinsic which means that it is dependent on the embedding of the surface. Differential geometry decomposes the mean curvature,  $\mathcal{M}$ , into its principal curvatures,  $\kappa_n$ , such as:

$$\mathcal{M} = \frac{\kappa_1 + \dots + \kappa_N}{N}. \quad (4.6)$$

To understand the difference between Gaussian and mean curvature and the concept of principal curvatures it is again instructive to consider a cylinder. As already mentioned, the principal curvatures of the cylinder are  $\kappa_1 = 1/R$  ( $R$ =radius of the cylinder) and  $\kappa_2 = 0$ . An ant living on the surface of the cylinder, unconscious of the surrounding world, will consider the cylinder being flat but would be capable of detecting small irregularities on the surface. What it experiences is the intrinsic (Gaussian) curvature which for a cylinder is  $\mathcal{G} = 1/R \cdot 0 = 0$ . Looking at the cylinder from an external point of view we see that the cylinder is flat along the principal axis but curved around the axis. Thus the external (mean) curvature is  $\mathcal{M} = (1/R + 0)/2 = 1/2R$ . When using the level set method we consider implicit surfaces in an embedding function and we will therefore mostly use the mean curvature. However, for some cases it can be useful to use the minimum principal curvature that can be expressed as a combination of the Gaussian and mean curvature:

$$\kappa_{min} = \mathcal{M} - \sqrt{\mathcal{M}^2 - \mathcal{G}} \quad (4.7)$$

Using this definition of the curvature, tubular structures are smoothed axially and not radially, as if they are open curves in a 3D space, allowing them to keep their tubular form. This effect is illustrated in Figure 4.5. Thus, this curvature flow satisfies the property of shrinking to a point while preventing undesirable changes of topology.

The mean curvature of the level set function for an arbitrary dimension is expressed in Eq. (4.4). In the 2D case the expression of the mean curvature becomes:

$$\nabla \cdot \left( \frac{\nabla \phi}{|\nabla \phi|} \right) = \frac{\phi_{xx}\phi_y^2 - 2\phi_x\phi_y\phi_{xy} + \phi_{yy}\phi_x^2}{(\phi_x^2 + \phi_y^2)^{1/2}}. \quad (4.8)$$

where  $\phi_x$  is the derivative of  $\phi$  with respect to  $x$ ,  $\phi_{xx}$  is the second derivative and  $\phi_{xy}$  is the cross derivative with respect to  $x$  and  $y$ . In Figure 4.6 the evolution of a cube under mean curvature flow is shown. For the 3D case the expression becomes much longer but it is still feasible to implement. The expression in 5D is far too complicated to be numerically acceptable.

N-D mean curvature flows have already been treated in literature [4, 32]. Hence, for dimensions superior to three the theory developed by Ambrosio and Sonner [4] will be used to determine the mean curvature in a N-D space.

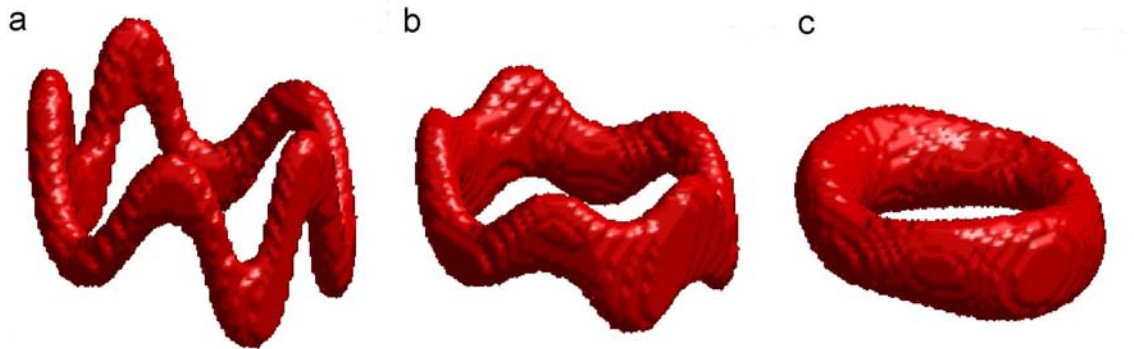


**Figure 4.5:** Flow evolving under minimal principal curvature. The original structure in a) evolves while keeping the tubular structure in b) and c). From the shape in c) it shrinks to a point and disappears.

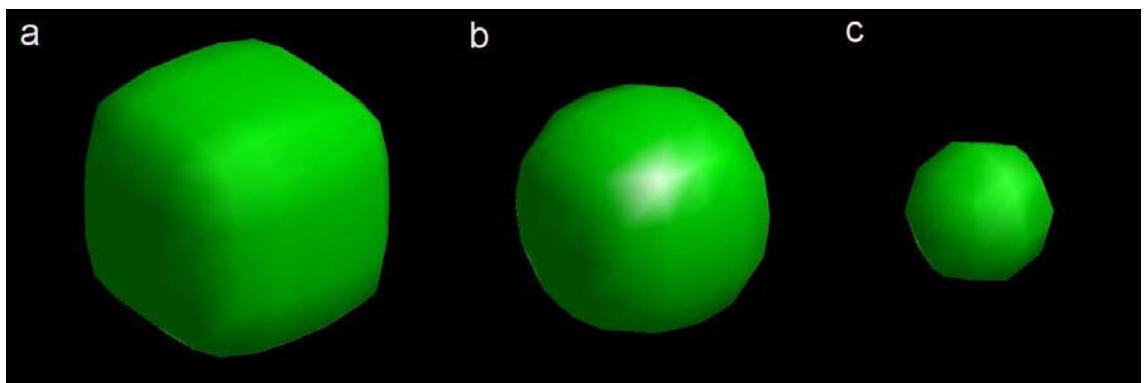


**Figure 4.6:** Example of cube evolving under mean curvature flow, a) the corners of the cube are directly smoothed out and b) becomes a sphere that shrinks c) to a point.

They show that the principal curvatures of a hyper-surface in N-D, embedded in a level set function,  $\phi$ , of codimension one are then given by the eigenvalues of the following  $N \times N$  matrix:

$$\frac{1}{|\nabla\phi|^2} P_{\nabla\phi} \nabla^2 \phi P_{\nabla\phi}. \quad (4.9)$$

Here  $\nabla^2 \phi(x)$  is the Hessian derivative operator, which corresponds to the second derivatives of  $\phi$ , and  $P_p$  is a projection operator for the Hessian of the level set function onto the space normal to the nonzero vector  $p$ :

$$P_p = I - \frac{p \otimes p}{|p|^2}. \quad (4.10)$$

Here  $I$  is the identity matrix and  $p \otimes p$  is the tensor product which in two dimensions is expressed as:

$$p \otimes p = \begin{pmatrix} p_1 p_1 & p_1 p_2 \\ p_1 p_2 & p_2 p_2 \end{pmatrix}$$

with  $p = \begin{pmatrix} p_1 & p_2 \end{pmatrix}$ .

Their work extends to surfaces of arbitrary co-dimension and they show the existence and uniqueness of surfaces propagating with speeds from these definitions.

In Chapter 6 we will use a 5D level set to evolve a hyper surface. To illustrate the above theories we have evolved hyper-cube in 5D through a mean curvature flow and seen how it first turns into a hyper sphere and then finally shrinks to a point, see Figure 4.7.

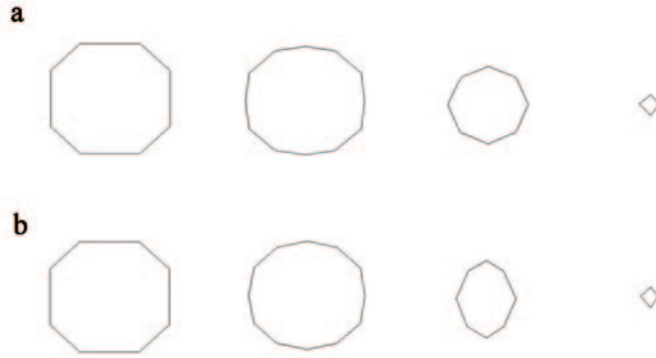


**Figure 4.7:** A hyper-cube evolving under 5D mean curvature flow. a)  $x - z$ -plane, b)  $y - \theta$ -plane.

### 4.3 Variational formulation

The variational formulation is generally used when determining  $F$  from an energy functional  $E$ , dependent on the data. Through the calculus of variation a PDE driving the interface

can be determined. This way of determining  $F$  guaranties that there exists a unique solution of the PDE and that the interface will converge towards this solution.

For a functional of the form:

$$E = \int_{\Omega} f(\mathbf{x}, \phi, \nabla \phi) d\Omega \quad (4.11)$$

where  $\Omega$  is the image domain. A necessary condition for a (local) minimum is given by the Euler-Lagrange equation [42]:

$$\frac{\partial f}{\partial \phi} - \frac{\partial}{\partial x_1} \left( \frac{\partial f}{\partial \phi_{x_1}} \right) - \frac{\partial}{\partial x_2} \left( \frac{\partial f}{\partial \phi_{x_2}} \right) - \frac{\partial}{\partial x_3} \left( \frac{\partial f}{\partial \phi_{x_3}} \right) = 0 \quad (4.12)$$

from the condition that the first variation of  $E$  must be zero.

Denote the left-hand side of the Euler-Lagrange equation  $F$ . If a surface  $\Gamma^*$  satisfies the equation  $F = 0$  then  $S^*$  is also a stationary solution to the equation:

$$\frac{\partial \mathbf{x}}{\partial t} \cdot \mathbf{n} = \pm F, \quad (4.13)$$

for all points  $\mathbf{x}(t) \in \Gamma^*$  where  $\pm F$  then is the velocity in the normal direction. This means that an initial surface will converge to a minimum of the functional  $E$  if evolved according to Eq. (4.13). Substituting this into Eq. (4.2) and again using that  $\mathbf{n} = \nabla \phi / |\nabla \phi|$  we come back to the level set function.

$$\frac{\partial \phi}{\partial t} = - \frac{\partial \mathbf{x}}{\partial t} \cdot \nabla \phi = \pm F |\nabla \phi|. \quad (4.14)$$

## 4.4 Geodesic Active Contours and surfaces

One of the first applications of the level set method in image processing is for edge detection and is known as Geodesic Active Contours (GAC), introduced by Caselles in [28]. A geodesic is a weighted curve between two points and the length shortest curve between the points defines their distance. In Euclidean space the shortest distance between two points is a straight line but in other spaces the distance is weighted by the topology of the manifold. If you consider yourself walking across a flat field of grass, the most energy-saving path between two points, A and B, would be a straight line. Now consider yourself being in Switzerland, in a highly mountainous area. The choice of the closest path between two points it is now less evident. The energy you need to go from A to B would be weighted by the altitude difference of your path. Minimizing the energy to go from A to B would be the same thing as to minimize a geodesic.

The same principle is used to find edges in an image. We are interested not only in finding the path of minimum classical length, but the one that minimizes a new length definition which bears in consideration the image characteristics. The image can be seen as a Riemannian space, where the metric defining the weighted length of a path is dependent on the proximity of an edge. The energy functional is constructed from this metric which

is based on a monotonically decreasing function  $f : [0, +\infty] \rightarrow \mathcal{R}^+$  such that  $[f(0) = 1$  and  $f(x) \rightarrow 0$  as  $x \rightarrow \infty]$ . The metric can be written:

$$[g_{ij}] : f(\nabla I)[\delta_{ij}], \quad (4.15)$$

where  $\delta_{ij}$  is the Kroenecker delta function. Example of functions,  $f$ , that can be used for edge detection are:

$$f(\nabla I) = 1/(1 + |\nabla I|) \quad (4.16)$$

$$f(\nabla I) = \exp(-|\nabla I|)$$

where  $I : [0, a] \times [0, b] \rightarrow \mathbb{R}^+$  is the image where we look for edges and  $\nabla I$  the image gradient. At an edge this image gradient is high and the most important property of  $f$  is that it goes toward zero in the vicinity of an edge.

Consider the parameterized planar curve  $\mathcal{C}(p) : [0, 1] \rightarrow \mathbb{R}^2$ . The length definition in the Riemannian space, defined from the metric in Eq. (4.15) is given by:

$$L_R = \int_{\mathcal{C}(p)} g_{ij} dx_i dx_j = \int_0^1 f(|\nabla I(\mathcal{C}(p))|) |\mathcal{C}'(p)| dp = \int_0^{L(C)} f(|\nabla I(\mathcal{C}(s))|) ds, \quad (4.17)$$

where  $ds$  is the Euclidean arc length. This weighted length corresponds to the energy functional in Eq. (4.11) and should be minimized. In the case of a surface in a 3D space this equation would be an integral over Euclidean area elements,  $da$  [29]. Thus, we wish to minimize the weighted area:

$$A_R = \iint f(|\nabla I|) da \quad (4.18)$$

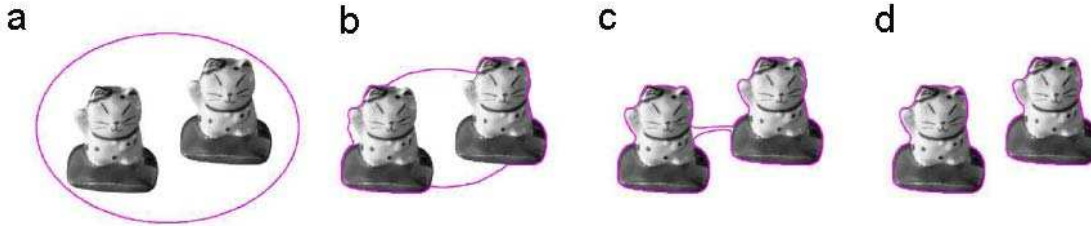


**Figure 4.8:** Segmentation of two 2D objects from one initial surface using the Geodesic Active Contour method. Note how the initial curve easily separates in several curves due to the implicit representation by the level set method.

By computing the Euler-Lagrange of the energy functional we obtain an equivalent result for 2D as well as for 3D which is the evolution of our level set function described by the following PDE:

$$\frac{\partial \phi}{\partial t} = f(\nabla I) |\nabla \phi| \nabla \cdot \left( \frac{\nabla \phi}{|\nabla \phi|} \right) + \nabla f(\nabla I) \cdot \nabla \phi. \quad (4.19)$$



This corresponds to a speed function,  $F = f(\nabla I)\mathcal{M} + \nabla f \cdot \mathbf{n}$ , where  $\mathcal{M} = \nabla \cdot (\nabla \phi / |\nabla \phi|)$  is the curvature as in Eq. (4.4) and  $\mathbf{n}$  is the normal to the evolving surface. The first term is the mean curvature flow multiplied by the image dependent function,  $f(\nabla I)$ . This will stop the front propagation at edges. The second term forms an attraction valley that pushes the front towards the edge when the front is sufficiently close to it. This is especially useful if a balloon term is added to the propagation speed. A balloon term is a constant speed and it is added to increase the convergence speed. This can be dangerous since the front sometimes can be pushed too far and pass the edge. In this situation the second term starts acting to push the front back to the edge. An example of a segmentation of 2D objects can be seen in Figure 4.8 and for 3D objects can be seen in Figure 4.9. Note how the initial curve in 2D and surface in 3D easily separate in several curves and surfaces due to their implicit representation by the level set method.

## 4.5 Region based segmentation front propagation.

Several methods of segmenting regions using level set methods have been proposed in literature. We will here consider two of them, the Geodesic Active Regions (GAR) [78] and the Chan-Vese model [30]. Both models are based on the hypothesis that an image is composed of homogenous intensity regions.

### 4.5.1 Geodesic active regions

The GAR model treats the case of  $N$  regions. The probability of a voxel,  $s$ , belonging to region,  $\mathcal{R}_i$  is dependent on the image value of the voxel,  $I(s)$  and equals  $p_i(I(s))$ . In this model this probability is determined by estimating the image intensity histogram with Gaussian distributions. The Gaussian distributions are found by using the maximization expectation algorithm [5]. An intensity based probability is not the only way to determine a region probability, in Chapter 7 a method for determining regions from diffusion tensor similarity is presented.

From the region probability an energy functional is defined. Combined with a boundary detection similar to what we have seen in the GAC model it will look like:

$$E(\{\mathcal{R}_i\}_{1 \leq i \leq N}) = \alpha \sum_{i=1}^N \int \int_{\mathcal{R}_i} -\log(p_i(I(x, y))) dx dy + (1 - \alpha) \sum_{i=1}^N \int_0^1 f(\nabla I(C(s))) ds \quad (4.20)$$

Here we recognize the second term from the GAC model. The first term aims at finding the optimal region by using an estimation of the entropy for the probability. By computing the system of Euler-Lagrange motion equations we obtain the following speed function:

$$\begin{aligned} \forall i \in [1, N], \\ F(C(s)) = -\alpha \log \left[ \frac{p_i(I(C(s)))}{p_j(I(C(s)))} \right] + (1 - \alpha) f(\nabla I)\mathcal{M}_i + \nabla f(\nabla I) \cdot \mathbf{n}_i \end{aligned} \quad (4.21)$$

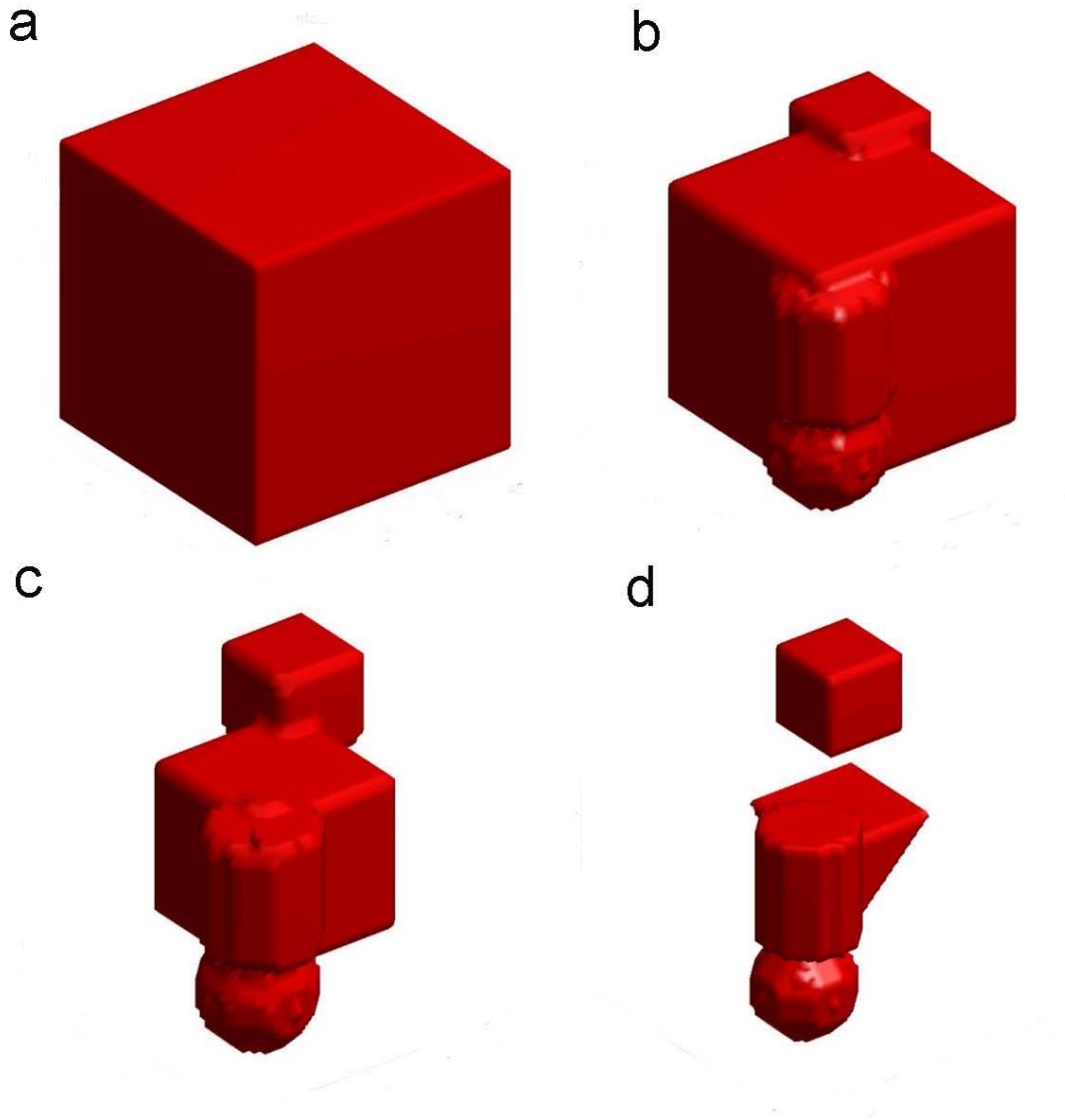


**Figure 4.9:** Segmentation of four 3D objects from one initial surface using the Geodesic Active Surface method. Note how the initial surface easily separate in several surfaces due to their implicit representation by the level set method.

where  $\mathcal{M}_i$  is the mean curvature of the curve  $C_i$  as in Eq. (4.4) and  $f$  is an image dependent function that goes toward zero in the vicinity of an edge as for example Eq. (4.16). Figure 4.10 shows an example of how several regions are defined and interact.

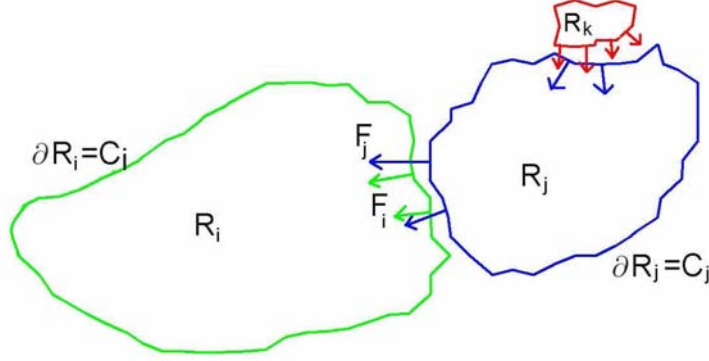


**Figure 4.10:** Region based segmentation with Geodesic Active Regions by evolving several coupled level sets.

The region based force turns out to have some very interesting properties. In the case:

$$\begin{aligned} p_i(I(C(s))) > p_j(I(C(s))) &\Rightarrow \\ \Rightarrow \frac{p_i(I(C(s)))}{p_j(I(C(s)))} > 1 &\Rightarrow -\alpha \log \left[ \frac{p_i(I(C(s)))}{p_j(I(C(s)))} \right] < 0. \end{aligned} \quad (4.22)$$

This leads to a negative speed term that aims at shrinking the curve, so that voxel  $s$  can be attributed to another region.

If, on the contrary, the voxel  $C(s)$  does not belong to  $R_i$ , then:

$$\begin{aligned} p_i(I(C(s))) < p_j(I(C(s))) &\Rightarrow \\ \Rightarrow \frac{p_i(I(C(s)))}{p_j(I(C(s)))} < 1 &\Rightarrow -\alpha \log \left[ \frac{p_i(I(C(s)))}{p_j(I(C(s)))} \right] > 0, \end{aligned} \quad (4.23)$$

and therefore the speed is positive and the force is applied to expand the curve.

In Figure 4.12 an example of segmentation using GAR is shown for the segmentation of the thalamus from a map of fractional anisotropy.

#### 4.5.2 Active contours without edges

Chan and Vese have presented in [30], a method for segmenting images without edge detection by using the weak formulation of the Mumford-Shah functional [72].

They separate the image into two regions, one inside the level set function  $\phi < 0$  and the other region on the outside of the boundary, hence  $\phi \geq 0$ . Each region is represented

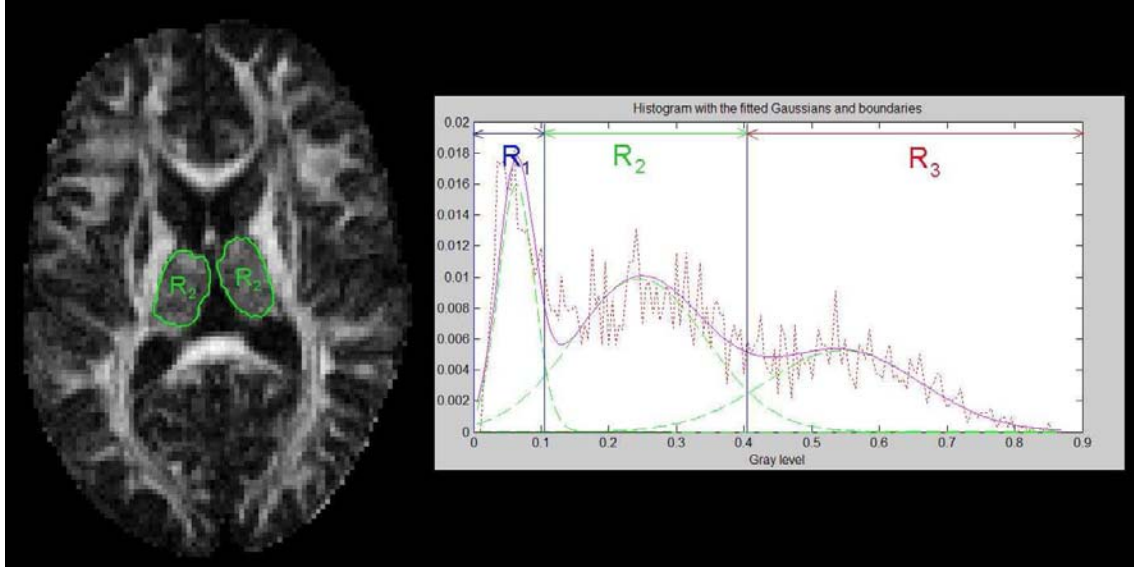


**Figure 4.11:** Segmentation of the thalamus using Geodesic Active Regions [79], on a map of fractional anisotropy (FA). The histogram shows the intensity values of the FA, the Gaussian estimation of the histograms using the maximizing expectation algorithm [5].

by its mean values,  $c_1$  and  $c_2$ , that are defined as:

$$\begin{cases} c_1 = \frac{\int_{\Omega} H_{\epsilon}(\phi) I dx}{\int_{\Omega} H_{\epsilon}(\phi)} \\ c_2 = \frac{\int_{\Omega} (1-H_{\epsilon}(\phi)) I dx}{\int_{\Omega} (1-H_{\epsilon}(\phi))} \end{cases} \quad (4.24)$$

where  $\Omega$  is the image domain and  $\partial\Omega$  is the boundary of  $\Omega$ .  $H_{\epsilon}(\phi)$  is the  $\epsilon$ -regularized version of the Heaviside function and  $c_1$  and  $c_2$  are the averages of the image  $I$  on the region  $\phi \geq 0$  and  $\phi < 0$  respectively.

Here, only the resulting equation for the interface evolution will be presented. As in the previous cases it has been obtained by computing the Euler-Lagrange of an energy functional. For more details we refer to [30]. Their level set equation is the following:

$$\left\{ \begin{array}{ll} \frac{\partial \phi}{\partial t} = \delta_{\epsilon}(\phi) \left[ \mu \nabla \cdot \left( \frac{\nabla \phi}{|\nabla \phi|} \right) - (I - c_1)^2 + (I - c_2)^2 \right] & \text{in } \Omega \\ \frac{\delta_{\epsilon}(\phi)}{|\nabla \phi|} \frac{\partial \phi}{\partial n} = 0 & \text{on } \partial\Omega \end{array} \right\} \quad (4.25)$$

Here  $\delta_{\epsilon}(\phi)$  is the  $\epsilon$ -regularized Delta function [30] and  $\mu > 0$  is a fixed parameter. This equation has similar properties as Eq. (4.21). The front will expand when the voxels close to the interface have values closer to the mean of the image inside the surface and shrink when it resembles the voxels outside more.

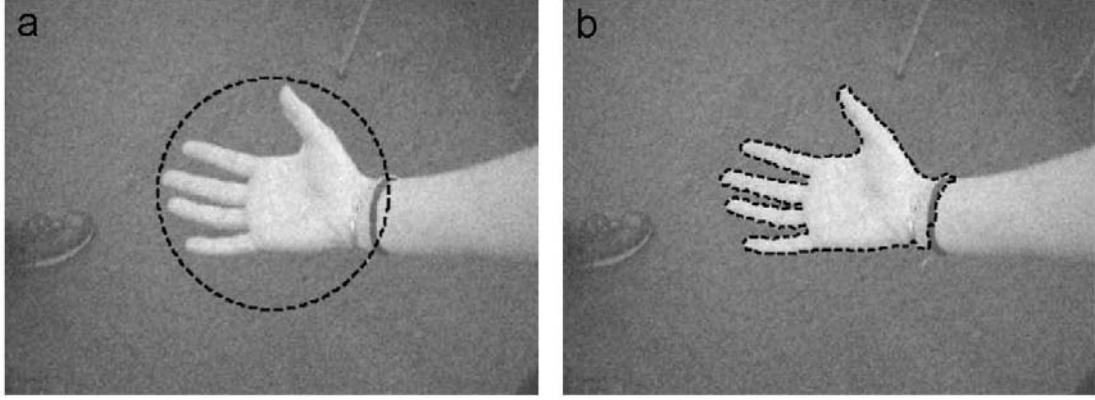


**Figure 4.12:** Rosa's hand segmented by Xavier Bresson, using the Chan-Vese method.

## 4.6 Numerical implementation of the level sets.

As mentioned earlier the numerical schemes for implementing the level set method is borrowed from mechanics and especially from the theory of hyperbolic conservation laws. We will not present the details of the implementation but just mention a few specific features that we have considered during our implementation of the method.

### 4.6.1 The upwind scheme

It is important during the evolution of the level sets to consider that *"the numerical domain of dependence should contain the mathematical domain of dependence"* [87]. A concrete example of this is the computation of the normals. If we consider an expanding closed curve,  $CT(t) := \{x(t) \mid \phi(\mathbf{x}(t), t) = 0\}$ , the domain of dependence is situated just outside the curve where the level set function is positive,  $\phi > 0$ . The normals should therefore be pointing outwards and be computed from the values of the region of dependence, see Figure 4.13.

As we have seen earlier the normal is expressed as  $\mathbf{n} = \nabla\phi / |\nabla\phi|$ . Numerically the derivatives can be computed with three different domains of dependence using the *forward*, *backward* and *centered difference operator*. Numerically the spatial derivatives of a function  $u$  with respect to  $y$  are expressed as follows:

$$\begin{aligned} D^{+y}u &= \frac{u(y+h,t) - u(y,t)}{h} \\ D^{-y}u &= \frac{u(y,t) - u(y-h,t)}{h} \\ D^{0y}u &= \frac{u(y+h,t) - u(y-h,t)}{2h}. \end{aligned} \tag{4.26}$$

To ensure the correct domain of dependence the outward normal along  $y$  should be expressed as:

$$n_y^+ = \max(D^{+y}u, 0) + \min(D^{-y}u, 0). \tag{4.27}$$

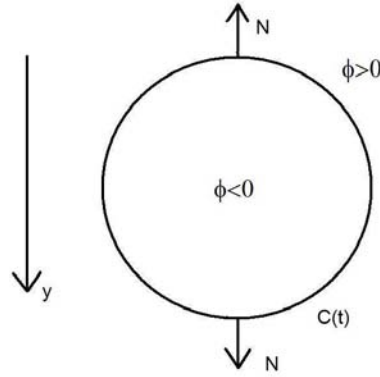


**Figure 4.13:** Regions of interest when computing derivatives according to the upwind scheme. See text for definitions.

If our closed curve is shrinking the normal is pointing inwards and the domain of dependence is situated inside the curve,  $\phi < 0$ . Numerically the inward normal along  $y$  should then be expressed as:

$$n_y^- = \max(D^{-y}u, 0) + \min(D^{+y}u, 0). \quad (4.28)$$

If we have a positive speed  $F$  the curve is moving outwards and we must use  $F n_y^+$  but if on the contrary  $F$  is negative and the curve is shrinking we must use  $F n_y^-$ . This can be summarized as:

$$F \mathbf{n} = \max(F, 0) n_y^+ + \min(F, 0) n_y^-. \quad (4.29)$$

#### 4.6.2 Stability condition

The time-step for the front propagation is determined according to the CFL-criterion [87]. This condition, observed by Courant, Friedrichs and Lewy [37], states that to assure stability for a numerical scheme the domain of dependence for each point in the domain should include the domain of dependence of the PDE itself. This will lead to the following time-step,

$$\Delta t \leq 1/\max(F).$$

We will mostly use

$$\Delta t = 0.5/\max(F),$$

since we have observed that this is the largest possible time step that can be used. The time step needs to be so small because of our way of fixing the level set in the re-initialization algorithm. If the value at a voxel changes too quickly compared to its neighbor, the zero level set can be moved next to a voxel of a high value.

#### 4.6.3 Preserving the level set function

Due to local dependence of the propagation speed, the level set function,  $\phi$ , can differ dependent on the distance to the zero level set. This creates irregularities that deform  $\phi$  so

it ceases to be a signed distance function. A correct level set function is crucial for a correct and smooth evolution of the surface, since the calculations of the normals and curvatures depend directly on it. Therefore, a re-initialization of the signed distance map has to be made regularly. It is implemented using the fast marching method to solve the PDE [2]:

$$|\nabla\phi| = 1. \quad (4.30)$$

#### 4.6.4 Implementation

The general scheme for evolving the level set function will have a similar character no matter how we chose the different front propagation forces,  $F$ , see Algorithm 4.1. In the different implementations the regularization force based on curvature,  $\kappa$ , will also change.

---

**Algorithm 4.1:** General principle for level set evolution

---

- 1: Set  $\Gamma(t = 0) := \{x(t) \mid \phi(\mathbf{x}(t), t) = 0\}$ ,
  - 2: **while** not converged **do**
  - 3:    $\mathbf{n} = \nabla\phi / (|\nabla\phi|)$  respecting the upwind scheme
  - 4:   Compute the curvature,  $\kappa$  respecting the upwind scheme
  - 5:   Compute image dependent speed,  $F$ .
  - 6:    $\chi = (F + \kappa) |\phi|$
  - 7:    $\phi(x, t + 1) = \phi(x, t) + \Delta t \chi$
  - 8:   Reinitialize  $\phi$  such that  $|\nabla\phi| = 1$
  - 9: **end while**
  - 10: Segmentation result:  $\Gamma(t) := \{x(t) \mid \phi(\mathbf{x}(t), t) = 0\}$
- 

## 4.7 Summary

In this chapter we have presented the basics of the extensive and highly theoretical framework of the level set method. There are plenty of more to be told on this matter and there is currently a lot of research on extensions and improvements to be done. The presented parts will be used further on in this thesis. In general, the principal problem has been to attribute appropriate functions to the front-propagation speed,  $F$ . In Chapter 5 we will define  $F$  using diffusive similarity between tensors for segmentation of white matter fiber tracts from Diffusion Tensor Magnetic Resonance Images (DT-MRI). In the following chapter, Chapter 7, we will present a region based approach for segmenting gray matter structures in DT-MRI according to the theories of Paragios et al. [79] presented in Section 4.5. In

Chapter 6 we will extend the region based method by Chan and Vese [30] presented in Section 4.5, to 5D for segmentation of diffusion images of high angular resolution.



---

# A local front propagation method for white matter segmentation

---

# 5

## 5.1 Introduction

In this chapter we present a 3D geometric flow designed to segment the main core of fiber tracts in DT-MRI. By fiber tracts we mean regions containing spatially compact and coherent bundles of axons. These can be tubular structures such as the cortico spinal tract as well as planar structures such as the corpus callosum. The white matter of the brain consists of all such different tracts. In Chapter 3 we showed how these tracts could be easily segmented from a set of fibers obtained from a tractography algorithm. We will here present a method for segmenting the tracts as an entity directly from the DT data without passing through the tractography step. In neuroscience, various problems can benefit from a segmentation of the fiber tracts as a whole as we propose in this chapter. The possibility of measuring the diffusion inside chosen fiber tracts opens new perspectives to follow up evolution of diseases (Parkinson, Multiple Sclerosis, Alzheimers, epilepsy, stroke), to monitor therapy effects and to map anatomically important connectivity to be preserved in surgical interventions.

The challenge is to define an appropriate propagation speed  $F$ , Eq. (4.3), that drives the flow to fill out the whole fiber tract and to include an appropriate regularization that smoothes the tracts without changing their tubular structure. The diffusive properties are very different in different ends of the tracts since the fiber tracts turn, bend and change direction. It is therefore difficult to define the problem as a global minimization problem since the propagation speed must have a very local dependence. Furthermore, it is very important that we use the directional information as well as the quantitative information about the diffusion. In many regions of the brain, fiber tracts pass close to each other and if only a scalar value such as an anisotropy measure is used nothing will separate the regions from each other. Using the full tensor is necessary for satisfying results as has already been

shown for regularization problems [31, 36, 97, 100]. Reducing the DT to for example its principal directions of diffusion leads to several problems. Due to noise in the acquisition, the order of the eigenvalues can sometimes be swapped and in fiber crossings the principal direction loses its significance [8].

Instead of using directly the physical properties of the DT, we base our approach on the assumption that adjacent voxels within the same tract have similar properties of diffusion. Therefore, we measure the similarity of diffusion between voxels and then using this similarity as a front propagation speed. For a local dependence, the similarity is measured between tensors lying on the surface and their neighbors in the direction of propagation. The measure of similarity that we use to compare the diffusion is based on the whole diffusion tensor, which helps to avoid problems that occur when only the principal direction is used. The tensor scalar product (TSP), see Chapter 2, uses all possible combinations of the eigenvectors and an eventual swapping of principal directions will not influence the result. The influence of noise will thereby be diminished.

Once the propagation speed  $F$  is defined the front propagation is implemented using the level set method as in Chapter 4. Fiber tracking methods in general demand a regularized tensor field, our geometric flow regularizes the 3D surface as it evolves inside the fiber tracts so that a regularized tensor field is not needed. Several aspects of our flow take care of this smoothing, the nature of the similarity measure, the inertia that the local dependence induces and the use of a smoothing term added to the flow. The smoothing term is the minimal principal curvature of the tract itself, the use of minimal principal curvature is to keep the thin tubular structure which is typical for fiber tracts. Further details on the choice of curvature was analyzed in Section 4.2.2.

One of the first approaches of using PDEs and variational methods on DT data was published by Parker et al. [80]. They used the fast marching method to create a weighted distance field from the tensor properties. The connection paths between different brain regions are then the geodesics that minimizes the weighted path length and is obtained by backtracking in the distance field. Campbell et al. [27] have also used level set theory to implement a geometrical flow to track the fibers. They mostly focus on the problem of preventing leakage from the thin tubular structure that represents the fibers, by using flux maximizing flows.

Batchelor et al. [12] use more of the tensor information by solving the diffusion equation iteratively. The method creates paths that originate from a chosen seed-point and can be considered as probability measures of a connection. A similar approach is presented by O'Donnell et al. [74] where they find the steady state of the diffusion equation to create a flux vector field. In the same paper they show how the inverse diffusion tensor can define a Riemannian metric that is used to find geodesic paths that can be interpreted as fiber tracts.

The above methods focus on finding individual fiber paths whereas we have chosen to search for regions that correspond to certain fiber tracts. Tench et al. [94] was one of the first to segment regions by finding trajectories of individual fibers and then identifying voxels that belong to the same structure. The identification is based on the similarity

of the shape of the trajectory paths. Zhukov et al. [110] also focus on segmenting white matter regions from DT-MRI instead of on fiber tracts. They present new invariants of the tensor such as an anisotropy measure of the tensor that is rotationally invariant and not dependent on the computation of eigenvalues. These invariants are then used to calculate scalar volumes, one that represents the total diffusivity within a voxel and another that describes the anisotropy. On these scalar maps he segments regions with similar diffusion properties and then he applies a level set method to obtain a smooth segmentation. A drawback with Zhukov's method is that he only uses a scalar measure and ignores the directional information. Posterior to our publication of this work in [57], Wang and Vemuri [102] and Lenglet et al. [64] presented region based approaches for segmentation of DT-MRI using PDEs and variational methods. We will discuss their work further in Chapter 7.

## 5.2 Method

### 5.2.1 Similarity measures of DT

Alexander et al. [3] have explored measures for comparison of tensors to perform elastic matching of DT images. These measures take both the magnitudes and the directions of the diffusion into account. One of the most common measures of similarity between two tensors is the tensor scalar product (TSP). This is a measure of the overlap between two tensors:

$$\mathbf{D}_1 : \mathbf{D}_2 = \text{Trace}(\mathbf{D}_1 \mathbf{D}_2) = \sum_{j=1}^3 \sum_{i=1}^3 \lambda_{1i} \lambda_{2j} (e_{1i} e_{2j})^2. \quad (5.1)$$

The TSP is often normalized to avoid influence by the relative size of the two tensors. This will emphasize the shape and orientation of the tensor.

$$\text{NTSP}(\mathbf{D}_1, \mathbf{D}_2) = \frac{\mathbf{D}_1 : \mathbf{D}_2}{\text{Trace}(\mathbf{D}_1) \text{Trace}(\mathbf{D}_2)}. \quad (5.2)$$

Another way of measuring the tensor similarity using the full tensor information that is also presented by Alexander et al. [3], is the tensor difference (TD).

$$\text{TD}(\mathbf{D}_1, \mathbf{D}_2) = \sqrt{(\mathbf{D}_1 - \mathbf{D}_2) : (\mathbf{D}_1 - \mathbf{D}_2)} \quad (5.3)$$

The TD measures the difference in size and shape as well as orientation between the two tensors.

A way of directly comparing the diffusion between two tensors is to compare the diffusion in the direction of all unit vectors on the unit sphere,  $S^2$ ,  $\mathbf{x}$ , using the double contraction. We will call this measure of similarity for integral similarity (IS).

$$\text{IS}(\mathbf{D}_1, \mathbf{D}_2) = \int_{S^2} \min \left( \frac{\mathbf{x} \mathbf{D}_1 \mathbf{x}^T}{\mathbf{x} \mathbf{D}_2 \mathbf{x}^T}, \frac{\mathbf{x} \mathbf{D}_2 \mathbf{x}^T}{\mathbf{x} \mathbf{D}_1 \mathbf{x}^T} \right) d\mathbf{x}. \quad (5.4)$$

The IS gives us a percentage of the common diffusion for the two tensors.

**Table 5.1:** Comparison between similarity measures between different combinations of isotropic and anisotropic tensors. The normalized tensor scalar product(NTSP), the tensor difference(TD) and integral similarity(IS). Here  $D_{anisotropic,n}$  represents the anisotropic tensor with its principal vector rotated  $n$  degrees.

Tensors	NTSP	1-TD	IS
$(D_{anisotropic,0}, D_{anisotropic,0})$	0.57	1	1
$(D_{isotropic}, D_{isotropic})$	0.33	1	1
$(D_{isotropic}, D_{anisotropic,0})$	0.33	0.25	0.54
$(D_{anisotropic,0}, D_{anisotropic,30})$	0.51	0.75	0.79
$(D_{anisotropic,0}, D_{anisotropic,45})$	0.46	0.5	0.72
$(D_{anisotropic,0}, D_{anisotropic,90})$	0.36	0	0.64

In Table 5.1 the different measures of similarity have been compared. We see that each measure has different specific properties. For the purpose of white matter segmentation we have found the NTSP being the most appropriate measure. Firstly, it is dependent on the global shape of the tensor since it takes into account all eigenvalues and eigenvectors which is not the case with the other similarity measures. Secondly, since the main objective is to propagate the surface in the anisotropic regions while avoiding the isotropic regions, we want a high speed,  $F$ , in the anisotropic areas and a low speed in the isotropic areas. For this, the NTSP measure is highly interesting since only a completely anisotropic tensor with diffusion in only one direction compared with itself will sum up to one and the similarity between two isotropic tensors are low (see Table 5.1). Thirdly, this similarity measure is robust with respect to noise. Noise can sometimes swap the order of the eigenvalues but since the NTSP combines eigenvalues and eigenvectors independently of the order, this measure is more stable compared to other measures.

All the presented measures are dependent on the whole information of the DT. We see that the TD gives a high distinction between different DTs whereas the IS detects a more subtle difference between two rather similar tensors. In Chapter 7 we will use and discuss these two similarity measures more in detail.

### 5.2.2 The similarity based front propagation

As mentioned in the introduction we propose a front propagation method that is based on the assumption that the diffusion is similar between two adjacent voxels within the same tract. To perform the segmentation a small initial surface is placed inside the tract we wish to segment and the surface is then propagated using the similarity measure in Eq. (5.2). The front propagates into a voxel with a speed proportional to the similarity between the diffusion tensor in the voxel and the diffusion tensors in the adjacent voxels lying inside the

fiber. We define the front propagation speed as:

$$F(\mathbf{x}) = \frac{\sum_{\mathbf{y} \in \mathcal{N}(\mathbf{x})} NTSP(D(\mathbf{x}), D(\mathbf{y}))}{|\mathcal{N}(\mathbf{x})|} \quad (5.5)$$

where NTSP is the normalized tensor scalar product as in Eq. (5.2).  $\mathcal{N}(\mathbf{x})$  is the neighborhood of  $\mathbf{x}$  which in our case is defined as:

$$\mathcal{N}(\mathbf{x}) = \{\mathbf{x} - \mathbf{n}, \mathbf{x} - 2\mathbf{n}\}, \quad (5.6)$$

where  $\mathbf{n}$  is the normal which in this case is defined as:

$$\mathbf{n} = \frac{\nabla \phi}{\max(|\nabla \phi|_i)}, \quad (5.7)$$

where  $i$  represents each component ( $x, y, z$  in the 3D case) of the gradient of  $\phi$ . This means that the neighbors of  $D(\mathbf{x})$  are the voxels found by following the normal to the surface one and two voxels backwards from the original voxel, see Figure 5.1.

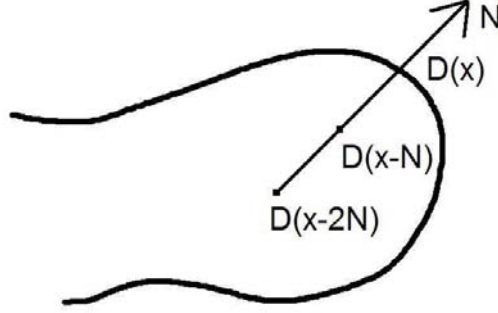


**Figure 5.1:** Choice of adjacent voxels with respect to the normal of the surface.

It is important to notice that the presented flow does not necessarily evolve in the direction of the diffusion. It evolves in the direction where the diffusion properties do not differ too much from the local neighborhood inside the fiber. This allows the surface to propagate towards the sides of the fiber tract and thereby segment the whole tract.

### 5.2.3 Regularization

Due to a high level of noise in the DT-MRI a segmentation only based on properties of the diffusion will be very irregular and sharp corners can occur that will create problems for the evolution. To assure a regular evolution and to smooth the tracts while segmenting them we regularize the flow by adding a curvature dependent speed. Lorigo et al. introduced the use of a curvature definition from co-dimension 2 flows on surfaces with a thin, tubular structure [69]. Instead of using either mean curvature or gaussian curvature, which normally destroy the tubular structure, they use the minimal principal curvature which is a combination of both curvatures see Eq. (4.7). Our level set equation now has the form:

$$\frac{\partial \phi}{\partial t} = (F + \kappa_{min}) |\nabla \phi| \quad (5.8)$$

### 5.3 Implementation details

The method has been implemented in Matlab 6.1 (The MathWorks, Inc.) except for the reinitialization of the signed distance function, which has been implemented in C and compiled with the mex-library, so the function can be called from Matlab. The general algorithm is presented in Algorithm 5.1.

#### 5.3.1 Thresholding

If the speed at one voxel is not equal to zero it will eventually lead to a propagation of the front at that voxel, even though the speed might be very small. To prevent unwanted propagation all speeds inferior to a certain threshold are set to zero. Thresholding is a very abrupt method so it risks causing discontinuities in the propagation. Since it is very important to maintain a continuous speed, we use the regularized Heaviside function, defined in [91], to get a smoother thresholding.

$$H_T(x) = \begin{cases} 0 & \text{if } x < T - \epsilon \\ \frac{1}{2} \left[ 1 + \frac{x-T}{\epsilon} + \frac{1}{\pi} \sin(\pi(x-T)/\epsilon) \right] & \text{if } |x - T| \leq \epsilon \\ 1 & \text{if } x > T + \epsilon \end{cases} \quad (5.9)$$

where  $T$  is the selected threshold and  $\epsilon$  is equal to 0.1 in all experiments.

The surface evolution is stopped when the propagation speed has been sufficiently small for several successive iterations. We have defined sufficiently small when after 10 iterations, the largest displacement of the surface is smaller than 0.1 voxel.

#### 5.3.2 Weighting the Speed Terms

The diffusion and the curvature dependent speed is not always of the same order. To have a satisfactory regularization without inhibiting the front propagation it is therefore important to set the weighting factor between them correctly. The curvature term in Eq. (5.8) is then referred to as  $\alpha\kappa_{min}$ ,

$$\frac{\partial \phi}{\partial t} = (F + \alpha\kappa_{min}) |\nabla \Phi|, \quad (5.10)$$

where  $\alpha$  is the weighting parameter. In all our experiments  $\alpha$  is set to 0.1, an experimentally determined value that provides the best equilibrium between the two forces, see Figure 5.4 and the result section.

Finally, our surface evolution equation has the following form:

$$\frac{\partial \Phi}{\partial t} = (H_T(F)F + \alpha\kappa_{min}) |\nabla \Phi|. \quad (5.11)$$

### 5.4 Data

#### 5.4.1 Synthetic Tensor Fields

To test the method we created a set of synthetic tensor fields. Tensor values for isotropic and anisotropic tensors were taken from real data on DT-MRI of the brain of a healthy

---

**Algorithm 5.1:** Level set evolution for fiber tract segmentation in DTI

---

- 1: Set initial departure region for the surface,  $\Gamma$
  - 2: Compute  $\phi$  such that  $\phi(\Gamma, t = 0) = 0$  and  $|\nabla\phi| = 1$
  - 3: **while** not converged do
  - 4:    $\mathbf{n} = \nabla\phi / (\max |\nabla\phi_i|)$
  - 5:    $\forall \mathbf{x}_i \in \phi(\mathbf{x}_i, t) = 0 : \mathbf{x}_{i-1} = \mathbf{x}_i - \mathbf{n}$
  - 6:    $\forall \mathbf{x}_i \in \phi(\mathbf{x}_i, t) = 0 : \mathbf{x}_{i-2} = \mathbf{x}_i - 2\mathbf{n}$
  - 7:    $\text{NTSP1} = \text{NTSP}(D(\mathbf{x}_i), D(\mathbf{x}_{i-1}))$
  - 8:    $\text{NTSP2} = \text{NTSP}(D(\mathbf{x}_i), D(\mathbf{x}_{i-2}))$
  - 9:    $F = (\text{NTSP1} + \text{NTSP2})/2$
  - 10:   Threshold  $F$ ,  $H_T(F)$
  - 11:   Compute  $\kappa_{min}$
  - 12:    $\chi = (H_T(F)F + \alpha\kappa_{min}) |\nabla\Phi|$
  - 13:    $\phi(\mathbf{x}, t) = \phi(\mathbf{x}, t - 1) + \Delta t\chi$
  - 14:   Reinitialize  $\phi$  such that  $|\nabla\phi| = 1$
  - 15: **end while**
  - 16: Segmentation result:  $\Gamma(t) := \{\mathbf{x}(t) \mid \phi(\mathbf{x}(t), t) = 0\}$
- 

subject. The values of the anisotropic tensor have then been manipulated so that the principal diffusion is in the x-direction.

Uniformly distributed random noise is added to the isotropic tensors so all of them will not be identical, these are used as a background for the fibers that are modelled using the anisotropic tensors. To obtain the desired direction of the anisotropic tensors they are rotated by first multiplying the principal diffusion vector by a rotation matrix and then projecting the remaining eigenvectors onto a plane which is orthogonal to the new principal direction of diffusion. The original eigenvalues are kept and the tensors are then reconstructed.

With this method two different 3D tensor fields are constructed, presented in Figure 5.2. The images show the largest eigenvector of the tensors at a cut along the z-axis. The first tensor field shows a semicircle to demonstrate the ability of following a curved fiber tract and the second tensor field simulates a branching fiber tract. To make the tensor fields more realistic, noise is added [96]. The six amplitude images from which the diffusion tensors

originally would have been acquired if they originated from real DT-MRI are obtained by making the inverse calculation and then noise is added on the amplitude images. The added noise is an approximation of Rician noise [45, 51] as it would be on MR data. The tensor images are then recreated and the resulting tensor fields can be seen in Figure 5.2.

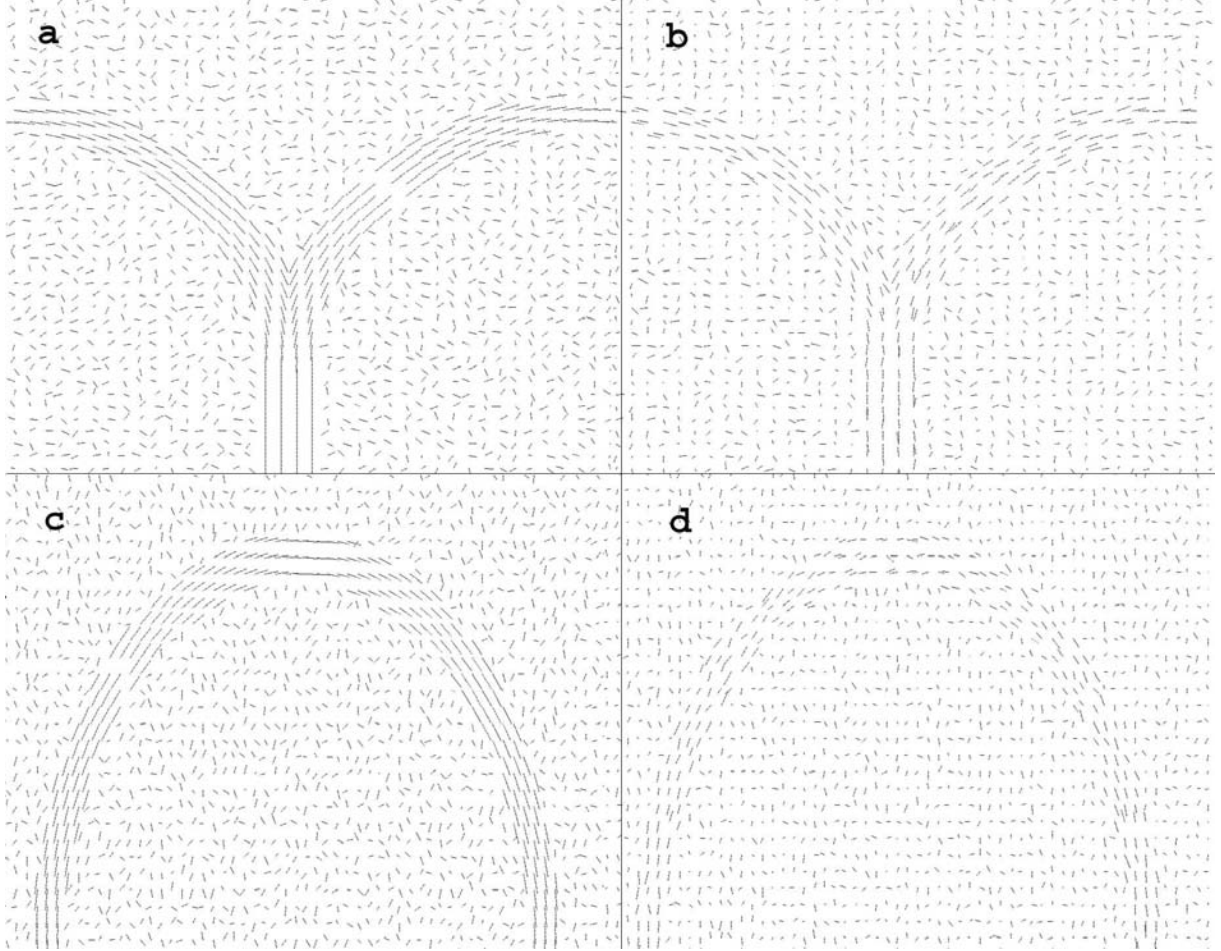


**Figure 5.2:** Synthetic DT fields modelling a diverging and a curved fiber tract. The principal directions of diffusion on a cut along the z-axis. (a) and (c): Before noise is added. (b) and (d): After noise is added.

### 5.4.2 Real DT-MRI

#### MRI Data Acquisition.

The diffusion tensor images used here were acquired with a 1.5 T clinical MRI scanner (Magnetom Symphony; Siemens, Erlangen, Germany). The data was produced with a diffusion-weighted single-shot EPI sequence using the standard Siemens Diffusion Tensor Imaging Package for Symphony. We acquired 44 axial slices in a 128 by 128 matrix covering



the whole brain of healthy volunteers, from the vertex to the end of the cerebellum. The voxel size was 1.64 mm by 1.64 mm with a slice thickness of 3.00 mm without gap. Timing parameters were a TR of 1000 ms and a TE of 83 ms. Diffusion weighting was performed along 6 independent axes and we used a b-value of 1000 s/mm<sup>2</sup> at a maximum gradient field of 30 mT/m. A normalizing image without diffusion weighting was also acquired. In order to increase the signal to noise ratio the measures were repeated 20 times. An anatomical T1 3D gradient echo volume of the entire head was also acquired during the same session. The whole examination lasted about one hour. In the following example, images from two healthy volunteers (male and female between 25- and 30-years old) were considered. Informed consent was obtained in accordance with institutional guidelines. The diffusion data were obtained from the Department of Radiology, University Hospital, Lausanne, Switzerland.

### Preprocessing of Data.

The preprocessing of the data and the geometric flow evolution was carried out in Matlab 6.1. The DT was computed for each voxel by linear combination of the log-ratio images according to Bassler and Pierpaoli [11]. The tensors were linearly interpolated component-wise between slices along the z-axis, to obtain a volume with a 3D regular grid of 1.64 mm.

## 5.5 Results and validation

### 5.5.1 Synthetic Tensor Fields

The method was tested on the synthetic images with different levels of SNR, using an SNR of 8, 16 and 32 on the MR amplitude images as in [96]. The segmentation is initiated by placing a small initial surface somewhere inside the synthetic fiber. An idea of suitable thresholds can be given by again looking at Table 5.1 where some typical values of the NTSP between different combinations of the tensors are presented.

Correct segmentations were obtained with several different thresholds between 0.45 and 0.5 and these thresholds were then used on the real MR data. In Figure 5.3 the effects of different choices of thresholds are shown, all synthetic tensor fields used for the segmentation have a SNR=8. Even though the synthetic tensor fields are very noisy, the resulting surfaces are relatively smooth due to our regularization that is performed as the surface is evolving. In Figure 5.4 the level of regularization is varied. The segmentation results are shown without regularization term, with a regularization term set too high and with an appropriate value of the regularization term.

In Table 5.2 and Table 5.3, quantitative values for the segmentation results are presented. The value is obtained by comparing the signed distance function (SDF) between the contour of the synthetic fiber tract without noise and the segmented fiber tract when noise is added with SNR = 8, and then calculating the error between the SDFs at the contours. The tables present the mean( $L_1$ ) and maximum( $L_\infty$ ) differences in value between the two SDFs.

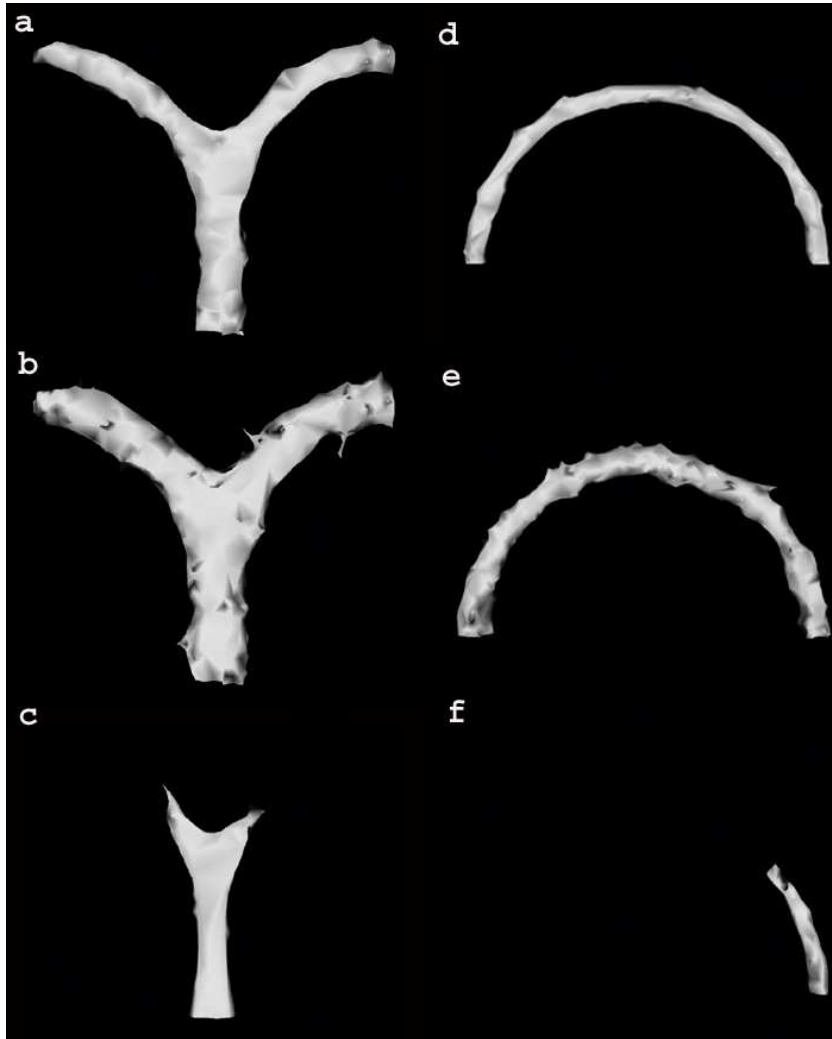


**Figure 5.3:** Effects of varying thresholds on the resulting segmentations of synthetic DT fields with SNR=8. (a) and (d): segmentation is ideal with threshold = 0.45. (b) and (e): segmentation is too large with threshold = 0.40, (c) and (f): segmentation is insufficient with threshold = 0.55.

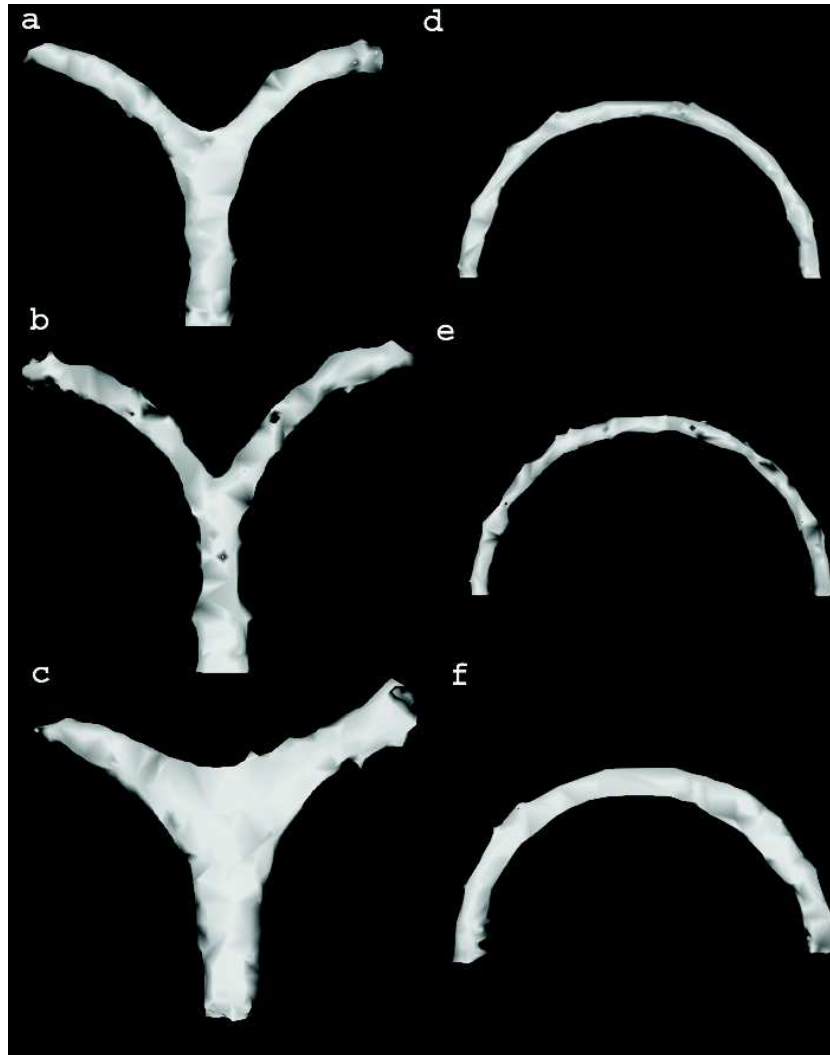


**Figure 5.4:** Effects of varying regularization parameter on the resulting segmentations of synthetic DT fields with SNR=8. (a) and (d): ideal regularization parameter, (b) and (e): no regularization, the segmentation is too noisy, (c) and (f): regularization parameter is set too high and has too high an influence on the real shape of the tracts. Threshold  $T = 0.45$  for all images.

**Table 5.2:** Quantitative values of the segmentation results for different thresholds. The values are obtained by comparing the signed distance functions of the contour of the synthetic fiber tract without noise and those of the segmented fiber tract when noise is added with a  $\text{SNR} = 8$ .

form	threshold	$\alpha$	max	mean
circle	0.40	0.1	2.98	0.56
	0.45	0.1	2.1	0.48
	0.55	0.1	47.5	20.5
fork	0.40	0.1	3.96	0.63
	0.45	0.1	1.56	0.51
	0.55	0.1	17.8	6.0

**Table 5.3:** Quantitative values of the segmentation results using different levels of regularization. The values are obtained by comparing the signed distance functions of the contour of the synthetic fiber tract without noise and those of the segmented fiber tract when noise is added with a  $\text{SNR} = 8$ .

shape	threshold	$\alpha$	max	mean
circle	0.45	0	2.32	1.07
	0.45	0.1	2.1	0.48
	0.45	2	3.3	0.29
fork	0.45	0	2.0	1.06
	0.45	0.1	1.56	0.51
	0.45	2	2.69	0.6

Table 2 shows the results for different thresholds and table 3 for different weighting of the regularization parameter. Both tables confirm the visual results that the best results are obtained for a threshold equal to 0.45 and a weighting factor for the curvature  $\alpha = 0.1$ .

Experiments were also made with smaller and larger neighborhoods than in Figure 5.1 and Eq. (5.5). For a smaller neighborhood the front propagation becomes too sensitive to noise. A larger neighborhood, in the sense that we look further behind the surface in the opposite direction of the normal, improves slightly the robustness of the method but the flow has difficulties segmenting bending fiber tracts and it also increases the computation time. A larger neighborhood, in the sense of adding voxels on the side of the normal, would make it impossible to track thinner fiber tracts. The best compromise between robustness and correctness of the segmentation is a neighborhood, lying on a line in the opposite direction of the normal, of two voxels as shown in Figure 5.1.

### 5.5.2 Real DT-MRI

#### Results

The segmentation has been performed on three different DT-MR images. The initial surface for the front propagation is placed by using color images representing directional information according to a method presented by Pajevic and Pierpaoli [77]. The initial surface is then placed inside an anisotropic region belonging to the fiber tract we wish to segment. The initial surface can be as small as one voxel but in general we chose the initial surface to be a one voxel thin tube that is directed along the supposed fiber. Two of the image acquisitions are from the same person. The results have been validated visually by comparing with post-mortem based neuroanatomical knowledge. Results are presented for one of the DT-MR images.

On the synthetic images we saw that several different thresholds are possible for a good segmentation. On the real MR data the same range of thresholds has been used and depending on the segmentation we desire, the threshold has been slightly varied within this range. In Figure 5.5 the cortico-spinal tract has been successfully segmented. To illustrate the effect of different choices of threshold on real DT-MRI, two segmentations of the corpus callosum have been made with different thresholds. The results can be seen in Figure 5.6. For a stricter threshold only the medial part, i.e. the splenium, the truncus and the genu of the corpus callosum is segmented. When choosing a lower threshold the segmentation surface extends further towards the forceps major, the radiation of the corpus callosum, the tapetum and the forceps minor.

In Figure 5.7 we segmented the inferior long association bundles as a whole, containing the occipito-frontal, the longitudinal inferior and the uncinate fascicles. These bundles run in an intricate and parallel fashion for most of their trajectories, therefore we treat them as one entity. It is a good example of a case where the diffusion orientation plays a crucial role since no contrast between this group and adjacent structures exists neither on fractional anisotropy maps, T1 nor T2 images.

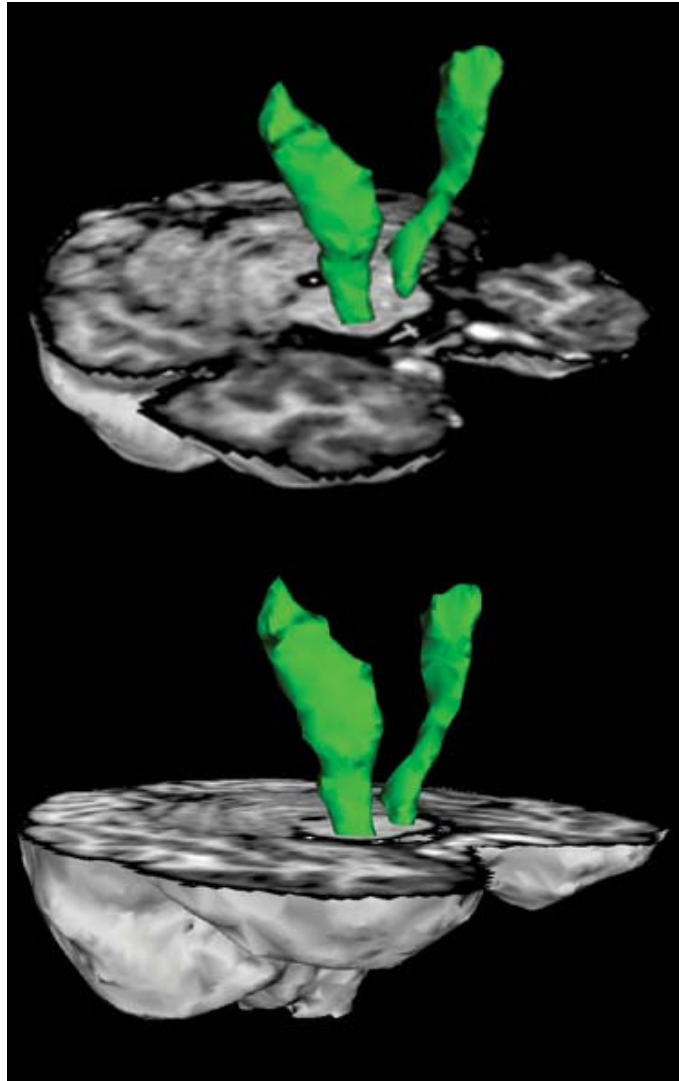


**Figure 5.5:** Segmentation of the left- and right cortico-spinal tract.

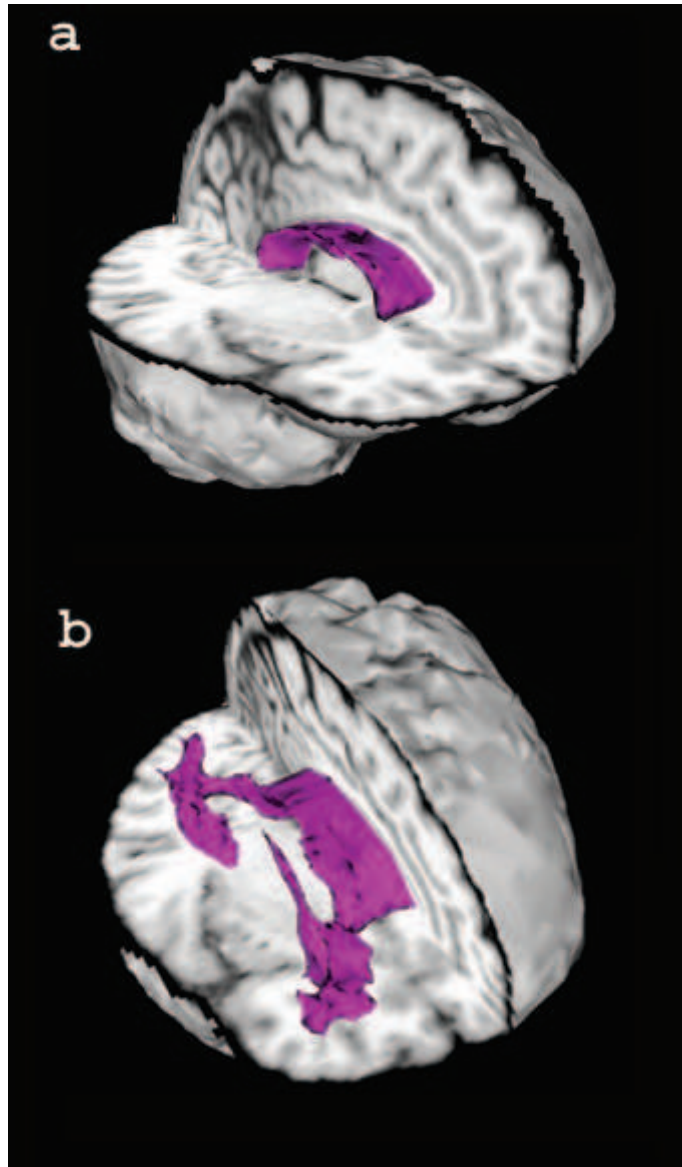


**Figure 5.6:** Segmentation of the corpus callosum (a): Segmentation is limited to the splenium, truncus and genu when threshold,  $T = 0.47$ , (b): in addition to (a) the segmentation also includes the forceps major, the radiations, the tapetum and the forceps minor when threshold,  $T = 0.45$ .

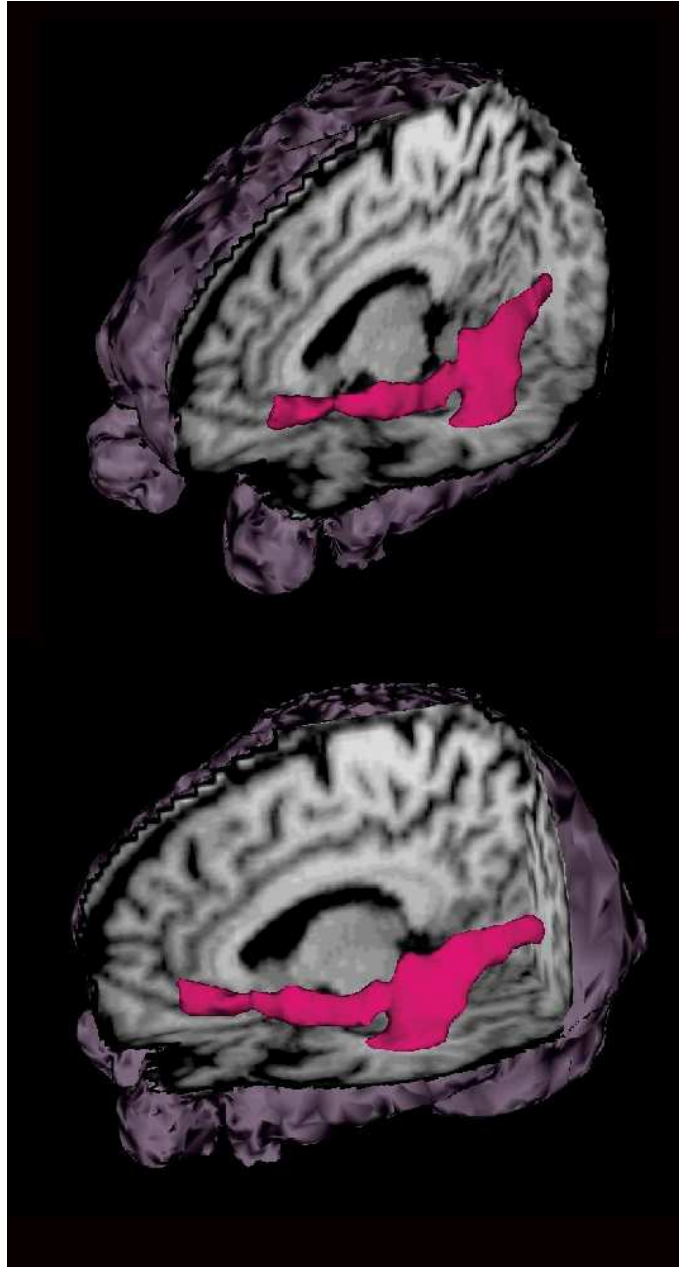


**Figure 5.7:** Segmentation of the inferior long association bundles as a whole (occipito-frontal, longitudinal inferior and uncinate fascicles).



## 5.6 Discussion

We have presented a new method for segmentation of the main core of fiber tracts by assuming that two adjacent voxels within the same tract have similar diffusion properties. The method manages to segment the larger tracts in the brain. This presented segmentation methodology can be very useful for several purposes such as studying the water diffusion in a tract of interest, e.g. the genu of the corpus callosum and the centrum semiovale in alcoholics [68, 82] or in the splenium of the corpus callosum in schizophrenic patients [40]. Through its precise description of the contour of a white matter structure it allows to compare its shape across a selected population, e.g. study of the corpus callosum sexual dimorphism [34, 81].

The weakest point of the segmentation method is the sensitivity to the choice of parameters. Since there is no objective measure of the exact solution for the brain images it is difficult to determine exactly the optimum thresholds and the a slightly different threshold can give quite a different result. The balance between the propagation speed and the regularization speed has also been determined on the synthetic images. We have seen that ignoring regularization leads to a noisy and irregular surface. When the regularization force is too strong the global shape of the segmented tract is deformed.

As mentioned in the introduction, most of the existing methods focus on following the principal eigenvector of the DT. The DT contains a lot more information than just the main direction and magnitude of the diffusion. The other eigenvectors and eigenvalues also contain important data which are often ignored. Just looking at the principal direction also leads to a larger sensitivity to noise since a smaller deviation of the principal direction will lead to an important accumulative error. By exploring more of the tensor information we have created a flow that is less sensitive to noise. The similarity measure we use is based on the whole tensor and combines all eigenvectors which makes it insensitive to swapping of eigenvalues, a phenomenon that can appear in the presence of noise. The similarity measure is shape dependent and favors anisotropic diffusion which is a great advantage for our application.

Using geometric flows for the segmentation has the advantage to other methods that it permits local comparisons of the diffusion in the direction of the surface evolution. An important advantage of our approach is the level set implementation. It provides an elegant tool for propagating and smoothing the segmented tracts and makes it possible to follow several paths simultaneously and effectively handle branchings and merging of fiber tracts.

Calculating the NTSP with adjacent voxels lying inside the propagating surface leads to a regularization of the fiber tract in addition to the regularization performed with the curvature based propagation force.

## 5.7 Conclusion

We have shown how similarity measures between tensors can be used for propagating an interface. We have seen how it is possible to perform the propagation with a highly local

dependence and using neither region nor boundary information. This propagation has been used for segmentation of some of the principal fiber tracts in a human brain. The fiber tracts are elongated regions of high anisotropy with diffusive properties that change throughout the tract. This work has been published in [57] [55].

In the next chapter we will show another application of how to propagate a flow using tensor similarity. This time the similarity will be used to define regions with high internal coherence independently of their anisotropy. We have stepped outside of the white matter to segment parts of the gray matter where the difference in diffusion between different parts is very subtle.

In Chapter 6 we will see the extension of fibers tract segmentation to HARD data.

---

# Evolving hyper surfaces for segmentation in position orientation space

---

# 6

## 6.1 Introduction

In Chapter 5 we presented a 3D geometric flow algorithm designed for segmenting fiber tracts from DT-MRI. The method was based on the assumption that adjacent voxels in a tract have similar properties of diffusion and we defined similarity measures between tensors to propagate the surface. Various problems can benefit from fiber tract segmentation, like quantitative investigation of the diffusion inside the chosen fiber tracts, white matter registration and surgical planning. However as mentioned in Chapter 2 the DTI model has several shortcomings concerning the resolution of complex brain white matter structures, in particular in the presence of fiber crossings. Passing from DTI to HARD data, see Section 2.3.4, can resolve this problem. Currently, the HARD data is used to map cerebral connectivity through fiber tractography [48] but we will in this chapter show how to adapt the approaches presented in Chapter 5 and Chapter 7 to the HARD problem.

In DTI several practical representations can be computed such as direction of principal diffusion, anisotropy and comparisons between different compartments of diffusion by diagonalizing the DT. These simplifications are less straightforward for the ODF. Frank et al. [41] presented a way of determining the anisotropy from HARD data but only anisotropy is not sufficient for segmentation of white matter tracts and the problem of crossing fibers remain unsolved. The field of ODF is often simplified to so called stix-maps. They reduce the ODF to a set of vectors representing its local maxima. The first idea we had to tackle the segmentation problem for HARD data was to use the stix-maps for computing a similarity measure based on the scalar product between its vectors. The front propagation had the same local dependence as in Chapter 5, see Figure 5.1. The front propagation speed was defined by first computing the scalar product between all the direction vectors of the stix-map. The combination with the highest scalar value was kept and the rest were

removed. If the angle between the two vectors that were kept was sufficiently small the surface would be propagated. This gave some first results that were not too bad but the flows had a tendency always to prefer straight lines. It is also highly questionable to reduce the complete ODF to only one principal direction.

When tackling any kind of problem it can often be useful to augment the dimensionality of the problem. By doing this on our data many of the problems encountered can be solved simultaneously. Instead of considering a 3D map of ODFs, we define a 5D position-orientation space (POS) as a combination of a spherical space of orientation and a Euclidean space of position. Two fiber tracts with different directions of diffusion that are crossing each other in the same voxel become separated in this 5D space and can be segmented separately without interference from one another. Another positive aspect of this 5D space is that it consists of only scalar values which allow us to adapt classical segmentation methods for grayscale images. However, augmenting the dimensionality has some drawbacks, namely the well-known "curse of dimensionality" [16] which refers to the exponential extension of the space as the dimension augment. This will make the computations very heavy.

Firstly we will explain the underlying principles of POS and show how to define it from a 3D map of ODF. We will then show that it is possible to segment white matter structures from HARDI MRI data by propagating a hyper-surface in this non-Euclidean 5D space.

As we have seen in Figure 4, the level set formalism is defined for  $N$ -dimensions and we will here show how to practically apply it in 5D.

## 6.2 Position Orientation Space

A HARDI experiment provides a 3D map of ODFs. Thus, for every position vector  $\mathbf{x} = (x, y, z)$ , in Euclidean 3D space,  $\mathbb{R}^3$ , there is an ODF measuring the intensity of diffusion in any direction,  $\mathbf{u} = (\varphi, \theta)$  where  $\mathbf{u}$  is a vector restricted to the unit sphere,  $S^2$ , with  $(0 \leq \theta < 2\pi, 0 \leq \varphi \leq \pi)$ . The cartesian product of  $\mathbb{R}^3$  and  $S^2$  forms POS that we note  $\Omega$ :

$$(\mathbf{x}, \mathbf{u}) \in \Omega = \mathbb{R}^3 \times S^2. \quad (6.1)$$

And its implied metric tensor allows us to determine the gradient operator as:

$$\nabla = \hat{\mathbf{x}} \frac{\partial}{\partial x} + \hat{\mathbf{y}} \frac{\partial}{\partial y} + \hat{\mathbf{z}} \frac{\partial}{\partial z} + \hat{\varphi} \frac{\partial}{\partial \varphi} + \frac{1}{\sin(\varphi)} \hat{\theta} \frac{\partial}{\partial \theta}. \quad (6.2)$$

To get some intuition about what POS is and why it is useful for fiber tract segmentation is it instructive to consider the case of a 2D map of ODF restricted to a plane. In Figure 6.1a a 2D slice of ODFs is shown. The slice shows a crossing between two fiber tracts. The ODFs in the figure are restricted to the plane and can therefore be described through only one angle,  $\theta$ . The intensity of the ODF varies with the angle. In the case where we only have one fiber there will be a peak in the intensity for the angle that corresponds to the direction of the fiber. In positions where two fiber tracts cross there will be two intensity peaks, one for the direction of each fiber. These two cases are illustrated in Figure 6.1b.

The third dimension represents the orientation of diffusion, hence the 2D ODF map is mapped as a 3D scalar field. This means that even though the two fiber tracts cross over in 2D, they will be separated in 3D and can therefore easily be segmented, see Figure 6.2.

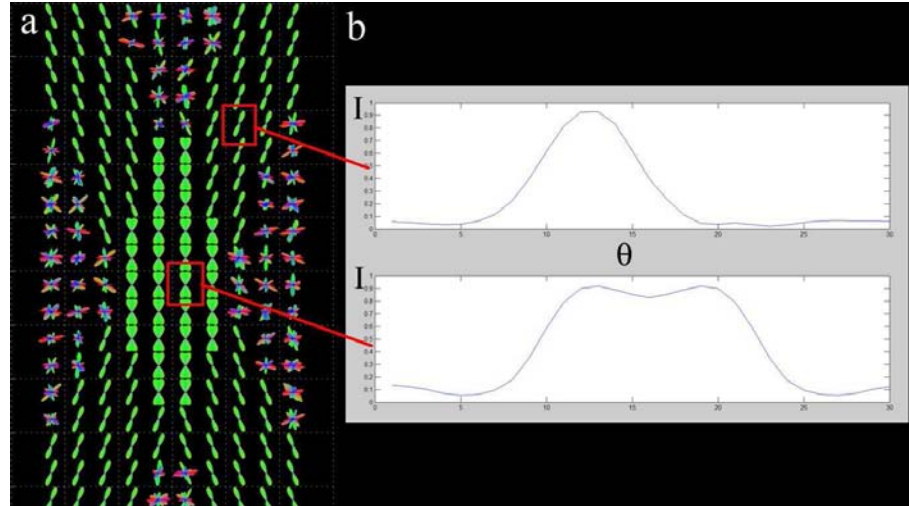


**Figure 6.1:** Example of POS for a 2D slice of a volume of ODFs. The slice shows a crossing between two fiber tracts. The intensity of the ODF varies with the angle,  $\theta$ . In the case where we only have one fiber there will be a peak in the intensity for the angle that corresponds to the direction of the fiber. In positions where two fiber tracts cross there will be two intensity peaks, one for the direction of each fiber.

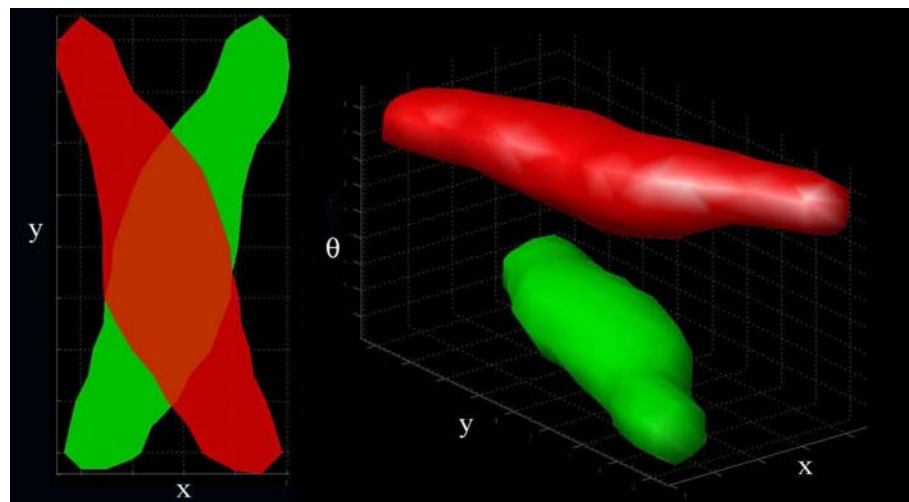


**Figure 6.2:** Example of POS for a 2D slice of a volume of ODFs. The 2D ODF field is mapped as a 3D scalar field. This means that even though the two fiber tracts cross over in 2D, they will be separated in 3D and can therefore easily be segmented.

## 6.3 Method and implementation

### 6.3.1 Creating POS

We have constructed the 5D POS from a 3D map of ODF. The values of the ODF are placed on a 2D grid. Due to the symmetry of the diffusion data only a hemisphere is sampled so we have that:

$$(\varphi, \theta) \in \{0, \frac{\pi}{n}, \dots, \pi - \frac{\pi}{n}\} \times \{0, \frac{\pi}{n}, \dots, \pi\}, \quad (6.3)$$

where  $n$  is the sampling step.

Due to the spherical geometry of the space there is a periodicity in the data. The two extremities along the  $\theta$ -axis are neighbors. Due to the symmetry of the diffusion data this periodicity is also present along the  $\varphi$ -axis. If, due to the same symmetry, only a hemisphere is considered, the periodicity along the  $\varphi$ -axis can be disregarded.

### 6.3.2 Evolution of the hyper-surface.

The hyper-surface is evolved according to Eq. (4.25). Once the POS is defined we have a scalar image not too different from a classical gray scale image. The specific considerations except for the high number of dimensions are the periodicity and the computation of the gradients, see Eq. (6.2). Implementing a level set function in 5D is theoretically straightforward but practically difficult. One of the main problem is handling the storage of the huge amount of data that is treated. Optimizing the computation of the level set function and its re-initialization is crucial. There is however one important issue to consider theoretically: the computation of the curvature. Hence, we propose to use the theory developed by Ambrosio and Sonner [4] as presented in Section 4.2.2 to determine the mean curvature in a 5D space, see Eq. (4.9) and Eq. (4.10).

## 6.4 Data

### 6.4.1 Synthetic data

To test the method we constructed a 3D volume of ODFs modelling two crossing fiber tracts, see left figure in Figure 7.2. The ODFs are normalized by removing the minimum from each ODF.

### 6.4.2 Real data set

The diffusion images were obtained on a healthy volunteer with a 3T Philips Intera scanner. We used a diffusion weighted single shot EPI sequence with timing parameters:  $TR/TE/\Delta/\delta = 3000/154/47.6/35$  ms,  $b_{max} = 12000 mm^2/s$  and a spatial resolution of  $2 \times 2 \times 3 mm^3$ . The data were acquired by sampling q-space on a 3D grid with 515 diffusion encoded directions restricted to the interior of a sphere of radius 5. From this acquisition the ODF map is reconstructed according a standard DSI scheme [103].

The diffusion data were obtained from Athinoula A. Martinos Center for Biomedical Imaging, Massachusetts General Hospital and the Harvard Medical School, Boston, MA, United States. Informed consent was obtained in accordance with institutional guidelines for all of the volunteers.

## 6.5 Results and validation

### 6.5.1 Synthetic data

One surface was initialized by placing a small surface of a few voxels in each fiber tract. The hyper surface was evolved until convergence and then projected back into 3D Euclidean space. The result can be seen in Figure 6.3. We see how each fiber tract is segmented completely without influence from the other crossing fiber.

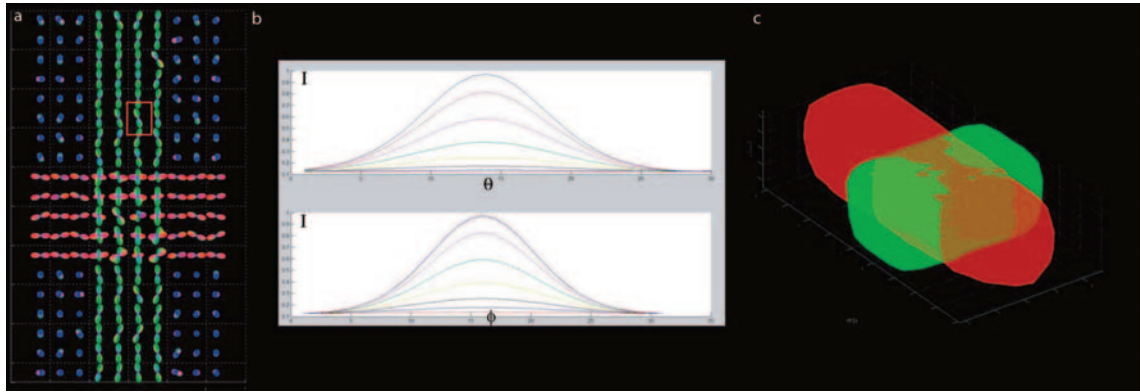


**Figure 6.3:** a) Slice of the synthetic 3D volume of ODFs. b) The intensity of the different angles plotted against each other. c) The 3D projection of the 5D result.

### 6.5.2 Real data set

The ODFs are normalized by removing the minimum from each ODF. The small initial surfaces were placed inside a brain region known to contain well known fiber tracts. The results are shown in Figure ?? and display the core of important fiber tracts such as the corpus callosum (green), the cortico spinal tract (red) and the arcuate fasciculus in blue. These are early results but show proof of principle. The current problem is the handling of data storage and only smaller volumes can be treated at the moment.

## 6.6 Discussion and Conclusion

We have shown that extending the dimensionality of the segmentation space from 3D to 5D originally overlapping structures disentangle. We have seen from the result on synthetic

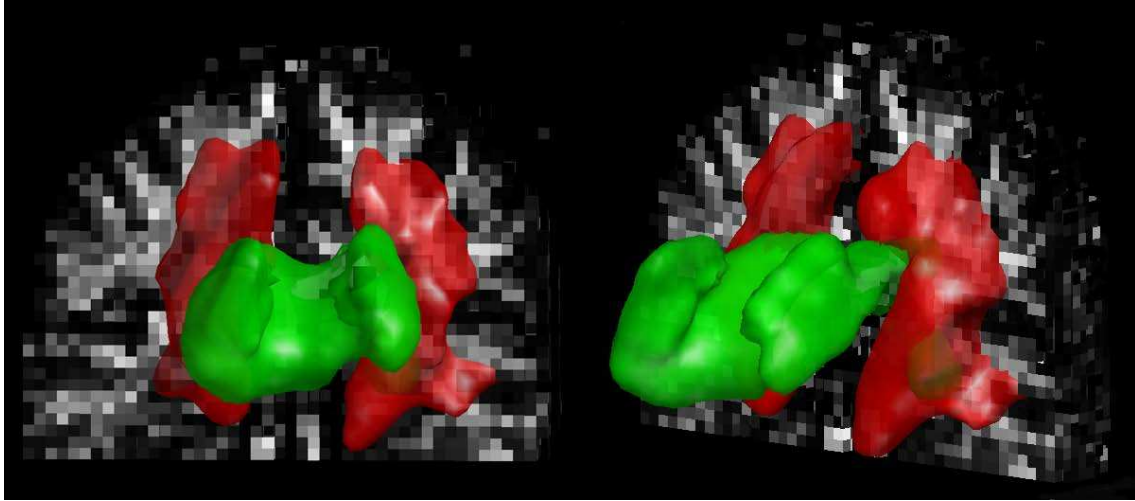


**Figure 6.4:** Results from application on HARD MRI from a human brain. The red surface is a part of the cortico spinal tract. The green surface is a segment of the corpus callosum.

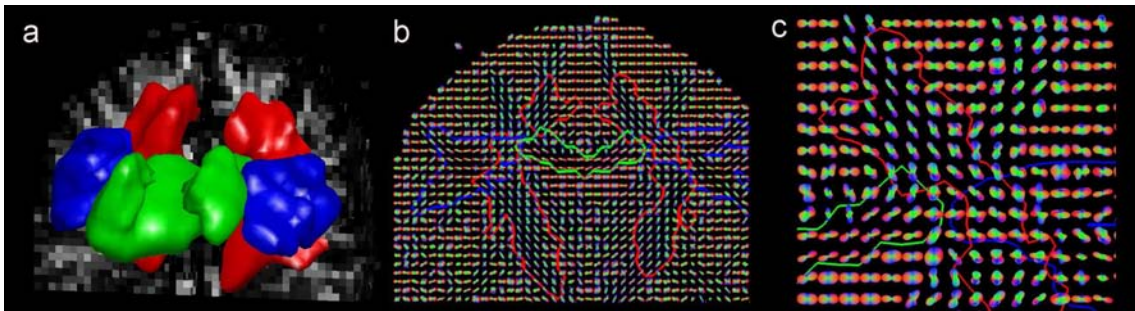


**Figure 6.5:** Results from application on HARD MRI from a human brain. The red surface is a part of the cortico spinal tract. The green surface is a segment of the corpus callosum and the blue is the arcuate fasciculus. a) The 3D projection of the 5D results. b) A coronal cut of the 3D projection of the result superposed on a coronal slice of the original ODFs. c) A zoom of b) that shows overlapping surfaces that were distinct regions in 5D.



data, that crossing fiber tracts in 3D are represented in 5D POS as separate objects characterized by intense diffusion. The results shown for brain HARD MRI data are the early results. Due to the huge 5D matrices only parts of the structures have been segmented. However, they clearly show the potential of this approach to clearly delimit structures of coherent diffusion. The problem of data handling will be solved with better computer power and a more efficient implementation and data storage.

Further, we have shown that it is possible to implement the level set method for evolving a hyper-surface in a non-Euclidean 5D space. To solve the problem of the implementation of the mean-curvature flow we have proposed to use the theory developed by Ambrosio and Sonner [4].

Segmenting regions in HARD MRI is a new approach for interpreting data with a different objective than classical fiber tractography. Fiber tractography provides a map of the cerebral connectivity and aims at visualizing fiber tracts as a set of lines. Our approach treats one fiber tract as one single object characterized by intense and coherent diffusion. This representation gives a different view of the brain architecture that can be more appropriate for applications such quantitative investigation of the diffusion as well as for surgical planning and white matter registration.



---

# Region based segmentation of tensor fields

---

# 7

## 7.1 Introduction

In the two previous chapters the goal was to segment highly anisotropic parts of the tensor fields, where the diffusive properties varied throughout the segmented structures. In this chapter we search for structures with a highly coherent diffusion throughout the entire structure. To maximize the coherence within the structure we define an energy functional as in Section 4.3, and we use the calculus of variations to obtain the level set equation. This yields a region-based speed that will be based on a similarity measure between diffusion tensors. The region-based speed will drive a set of coupled surfaces towards the solution of the segmentation problem. Firstly, we apply our method for segmenting the thalamus and its nuclei. We then apply the same method for segmentation of tensor fields in other domains than diffusion imaging, namely fluid dynamics where the tensor representation is commonly used. The particular case considered in this chapter is fields of Reynolds stress tensors which are explained more in detail in Section 7.6.

This chapter proposes several new strategies to efficiently segment complex objects in tensor fields. First of all, we use a sensitive similarity measure, presented in Section 5.2.1, that distinguishes very subtle differences between regions within, for example, the thalamus. Secondly, we present a new way of selecting the most representative tensor of a group of tensors for these kinds of applications. Most authors suggest to use the mean tensor whereas we argue for the importance of using the tensor with the minimum variance with its neighboring tensors. The third important point is the necessity of using several coupled level sets to define the background. Methods differentiating only between foreground and background will fail when applied to complex structures such as the brain. It is crucial for a region-based approach to consider all the surrounding structures for a correct definition of the speeds driving the segmentation.

For DT-MRI in general, emphasis has mainly been put on identifying white matter structures, but many gray matter structures can also be revealed through this new image modality. Most gray matter structures contain passing fibers which will affect the mean diffusion within the voxel and give the diffusion tensor a characteristic shape for that specific structure. Only recently, DT-MRI has started being used for segmentation purposes. The first approaches performed fiber tractography and used the result for segmentations [94]. Identification of the thalamic nuclei has been made by Behrens et al. [14] by mapping the connections between the thalamus and the cortex. Wiegell et al. [108] were some of the first to segment DT-MRI directly from the data by using a k-means algorithm, this method was used to segment the thalamic nuclei. The most recent approaches have been to use Partial Differential Equations (PDE), variational methods and level sets [39, 55, 57, 65, 84, 102, 110]. In the previous chapter we used the diffusive similarity between voxels to define a geometric flow implemented with level set method for fiber tract segmentation. Similarity measures based on the whole tensor information were used for propagating the flow. Since then, several papers have provided a well developed theory on PDE and segmentation in DT-MRI [39, 64, 65, 84, 101, 102]. Wang et al. [102] were the first to define regions from the DT and they used region based forces for the front propagation. The region-based force is defined from a distance metric between tensors. Wang et al. presented in [101] the very interesting approach of Kullback-Leibler (KL) distances. The KL distance is a frequently used concept in information theory and is a measure of the natural distance between two random variables. From this distance, Wang et al. [101] have derived similarity measures and segmented 2D tensor fields. Lenglet et al. [64] extended their work for 3D images and explored the statistics of the KL distances to segment tensor fields with higher internal variance. In this method however, we are not interested in allowing a high internal variance, rather in detecting the very small variances that exist between the thalamic nuclei. In fluid dynamics, numerous applications of the level set method for interface tracking exist [71][109]. The main contribution of our method in this domain is the improved contrast between different flow properties. This example shows that our segmentation method can be applied to several types of tensor fields.

We will here present an energy functional based on the theory of geodesic active regions (GAC) by Paragios and Deriche [78] as explained in Section 4.5. We will then show how it leads to the level set equation that will propagate the surfaces. The method will be applied on a synthetic tensor field and then on the thalamus and its nuclei where the results are compared with anatomical atlases. Finally, we apply the method on fields of Reynolds stress tensors from fluid mechanics.

## 7.2 Method

We have developed a region based approach for segmenting tensor fields: Each region is represented by the tensor that best represents all the tensors within the region. The probability of a voxel belonging to a certain region is then determined by tensor similarity measures between the most typical tensor of each region and the tensors lying close to the

region boundary.

To find the most representative tensor among a group of DTs, Jones et al. [61] use a distance metric,  $d_{ij}$ , between two tensors,  $(D_i, D_j)$ :

$$d_{ij} = \sqrt{(D_i - D_j) : (D_i - D_j)}. \quad (7.1)$$

where  $:$  stands for the Tensor Scalar Product as defined in Eq. (5.1). For determining the most representative tensor of the data set, this distance is computed between each pair of tensors. For each tensor we compute  $c_i$ :

$$c_i = \frac{\sqrt{\sum_{j=1, j \neq i}^n d_{ij}^2}}{n-1}, \quad (7.2)$$

and the most representative tensor is then the tensor with lowest value of  $c_i$ . This corresponds to the tensor with the smallest distance to all other tensors within the group.

The similarity measure that we use for comparing the tensors is the integrated similarity presented in Eq. (5.4). The similarity measure is the percentage of the common diffusion that each tensor has with the most typical tensor of each region. This percentage can be considered as a probability measure of a voxel belonging to a certain region. We therefore permit ourselves to set the energy functional as in the theories of Paragios et al. [78] where the region term aims at minimizing an estimation of the entropy of the similarity measure:

$$E(\{R_i\}_{1 \leq i \leq N}) = \alpha \sum_{i=1}^N \int \int \int_{\mathcal{R}_i} -\log(\text{IS}(D_{s(x,y,z)}, D_{typ,i})) dx dy dz + (1 - \alpha) \sum_{i=1}^N \int_0^1 ds_i, \quad (7.3)$$

where  $ds_i$  is the Euclidean arc length of the curves,  $\{R_i\}_{1 \leq i \leq N}$  are the regions and IS is the integral similarity described in Eq. (5.4).  $D_{typ,i}$  is the most representative tensor associated with the level set,  $\phi_i$  and it is computed according to Eq. (7.2).  $D_{s(x,y,z)}$  is the DT in voxel  $s$  at position  $(x, y, z)$ . Notice that compared with Eq. (4.20) the boundary information has been removed by setting  $f(I) = 1$ .

Computing the Euler-Lagrange gives for each surface the propagation speed:

$$F_i(s) = -\alpha \log \left( \frac{\text{IS}(D_s, D_{typ,i})}{\text{IS}(D_s, D_{typ,j \neq i})} \right) + (1 - \alpha) \mathcal{M}_i, \quad (7.4)$$

where  $\mathcal{M}_i$  is the mean curvature. It is continuously recalculated as the surface evolves. We will name the image dependent part of the propagation force  $F_i^D$ :

$$F_i^D(s) = -\log \left( \frac{\text{IS}(D_s, D_{typ,i})}{\text{IS}(D_s, D_{typ,j \neq i})} \right). \quad (7.5)$$

$F_i^D$  expands the surface,  $\Gamma_i$ , in the direction of the voxels of diffusion most similar to  $D_{typ,i}$ . To improve the segmentation we will chose to compare that probability of belonging to  $R_i$  with the maximum of the probabilities of belonging to the other regions. We therefore adjust Eq. (7.5) as follows:

$$F_i^D(s) = -\log \left( \frac{\text{IS}(D_s, D_{typ,i})}{\max_j (\text{IS}(D_s, D_{typ,j \neq i}))} \right), \quad (7.6)$$

which means that we compare only with the region  $j \neq i$  that has the highest resemblance with  $D_s$ .

### 7.2.1 Coupling Forces

When propagating several curves, overlapping can occur, meaning that a voxel has been initially attributed to two different regions. To avoid this, an artificial force is added in the direction of the normal to the corresponding level set motion equations. The force will penalize voxels which have been attributed to more than one region. If necessary, voxels that have not yet been labelled will also be penalized in order to force each voxel to belong to a region. The coupling forces for each surface,  $H_i$ , are defined as in [78].

$$H_i(j, \phi_j(s)) = \frac{1}{N-1} \begin{cases} +1, & \text{if } \phi_j(s) > a \\ -\frac{1}{\tan(1)} \tan(\phi_j(s)/a), & \text{if } |\phi_j(s)| \leq a \end{cases} \quad (7.7)$$

Here,  $a$  is a parameter to decide within which distance the coupling force shall act.

### 7.2.2 Final evolution

Each one of our surfaces,  $\Gamma_i$ , are now evolving according to the level set equation:

$$\frac{\partial \phi_i}{\partial t} = (F_i^D + \mathcal{M}_i + H_i) |\nabla \phi| \quad (7.8)$$

where  $F_i^D$  is the region based force Eq. (7.6),  $\mathcal{M}_i$  is the mean curvature and  $H_i$  is the coupling force.

## 7.3 Implementation details and parameters

The method has been implemented in Matlab 6.1 (The MathWorks, Inc.) except for the re-initialization of the signed distance function, which has been implemented in C and compiled with the mex-library. The algorithm can be seen in Algorithm 7.1.

### Convergence

The evolution of the surfaces is automatically stopped when the zero level set has only moved insignificantly after 10 iterations, in our case less than 0.1 voxel.

### Weighting the Speed Terms

The diffusion dependent speed,  $F_i$ , and the curvature dependent speed,  $\mathcal{M}_i$ , speed for each surface  $S_i$ , is not always of the same order. For a satisfactory regularization without inhibiting the front propagation it is therefore important to set the weighting factor between them correctly. Hence, we have the following relation:

$$\frac{\partial \phi_i}{\partial t} = (\alpha F_i^D + \beta \mathcal{M}_i + \gamma H_i) |\nabla \phi_i| \quad (7.9)$$

where  $\alpha, \beta, \gamma$  are weighting parameters. The parameters are set to  $\alpha = 10, \beta = 1$  and  $\gamma = 1$  for all experiments which has experimentally shown a good equilibrium between the forces.

---

**Algorithm 7.1:** Level set evolution for region based segmentation of DTI

---

```

1:  $N$  = number of surfaces.

2: Set initial departure regions for all surfaces surface,  $\Gamma_i \ i = 1..N$ 

3:  $\forall i$  compute  $\phi_i$  such that  $\phi_i(\Gamma_i, t = 0) = 0$  and  $|\nabla\phi_i| = 1$ 

4: while not converged do

5:   for  $i = 1..N$ 

6:      $\forall k \in \phi_i < 0$ 

7:      $\forall l \neq k \in \phi_i < 0$ 

8:      $d_{kl} := \sqrt{(D_k - D_l) : (D_k - D_l)}$ 

9:      $c_k = \frac{\sqrt{\sum_{k=1, l \neq k}^n d_{kl}^2}}{n-1}$ 

10:     $D_{typ,i} = \operatorname{argmin}(c_k)$ 

11:   end for

12:   for  $i = 1..N$ 

13:     $F_i^D = \log \left( \frac{\operatorname{IS}(D_s, D_{typ,i})}{\max(\operatorname{IS}(D_s, D_{typ,j \neq i}))} \right)$ 

14:     $\mathcal{M}_i = \nabla \cdot \left( \frac{\nabla\phi}{|\nabla\phi|} \right)$ 

15:     $H_i(j, \phi_j) = \frac{1}{N-1} \left\{ \begin{array}{ll} +1, & \text{if } \phi_j > a - \frac{1}{\tan(1)} \\ \tan(\phi_j/a), & \text{if } |\phi_j| \leq a \end{array} \right\}$ 

16:     $\chi = (\alpha F_i^D + \beta \mathcal{M}_i + \gamma H_i) |\nabla\phi_i|$ 

17:     $\phi_i(x, t) = \phi_i(x, t-1) + \Delta t \chi$ 

18:    Reinitialize  $\phi_i$  such that  $|\nabla\phi_i| = 1$ 

19:   end for

20: end while

21: Segmentation result:  $\Gamma(t) := \{x(t) \mid \phi(\mathbf{x}(t), t) = 0\}$ 

```

---

## 7.4 Data

The method has been tested on synthetic data and on diffusion data from two healthy volunteers.

### 7.4.1 Synthetic data set

The method was first validated on a synthetic tensor volume containing regions of tensors with slightly different diffusion properties. Values from different regions of the thalamus were used. These tensors were then placed in six regions in a 3D volume and rician noise was added [96]. A cut of a slice through the regions can be seen in Figure 7.1. To initialize the surfaces we ran a k-means clustering algorithm as in [108]. The k-means operates on a vector of parameters representing the tensors. This vector is constituted of the six values of the DT and three position parameters. The position values are weighted according to their relative importance. In our implementation this weight is 0.000000001. Once the clusters are obtained, the center points of the clusters are used as initialization points.

The algorithm was then applied to the tensor fields with a signal-to-noise-ratio(SNR) of 32. With a lower SNR similar regions can not be distinguished so for segmentation of the thalamic nuclei good imaging acquisitions with a reasonably good SNR are needed.

### 7.4.2 Real data set

The images were obtained with a single shot EPI sequence on a 3T Inera scanner from Philips. Six diffusion weighted images and 1 without diffusion weighting were acquired. TR and TE were 4858 ms and 78 ms respectively and b value was set to  $1000\text{mm}^2/\text{s}^2$ . We acquired 24 axial slices in a 256 by 201 matrix that was interpolated to a 256 by 256 matrix, covering the region of the deep cerebral nuclei. The voxel size was 1.0 mm by 1.0 mm with a slice thickness of 2.0 mm without gap. The data were again interpolated to 1.0mm by 1.0mm by 1.0mm. The diffusion data were obtained from the Department of Radiology, University Hospital, Lausanne, Switzerland.

Informed consent was obtained in accordance with institutional guidelines for the volunteers.

To validate the results, the segmented thalamus was defined according to the plane crossing the anterior (AC) and the posterior (PC) commissures (AC-PC referential) and co-registered with digital images of the Schaltenbrand and Wahren stereotactic atlas (SWSA) [86].

### The thalamic cytoarchitecture

The thalamus can be considered as the central relay station for brain neuronal communication. Every sensory system (except olfaction) makes synapses here before projecting into the cerebral cortex. Information received from diverse brain regions is passed on to the cortex through the thalamus. These passing fibers will slightly influence the anisotropy and shape of the diffusion tensor. Because these axonal projections have different orientations



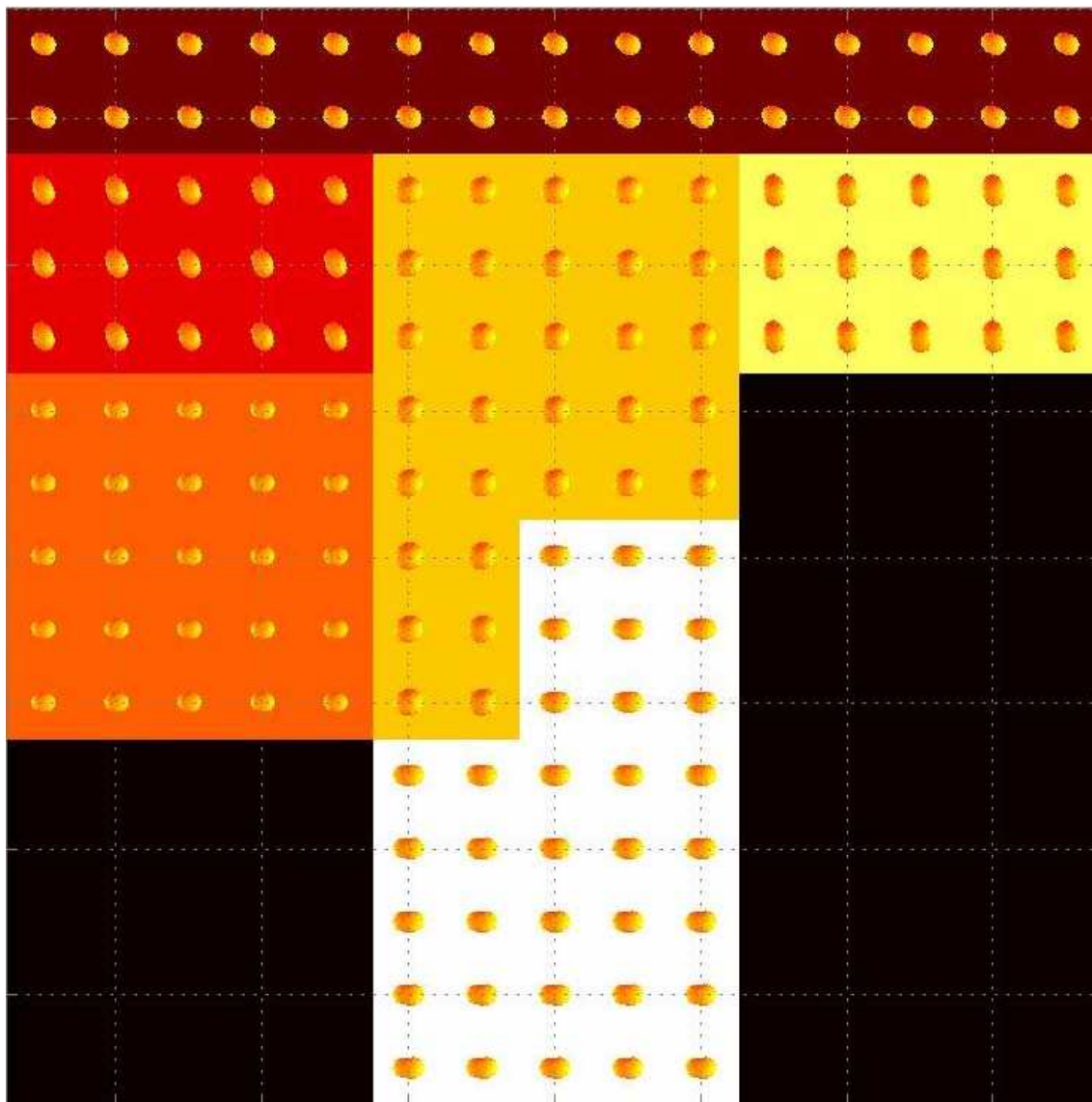


**Figure 7.1:** A cut of the synthetic tensor field used to test the segmentation method. The form of the tensors can be seen in each voxel displayed on a color map representing the anisotropy and principal direction [77].

depending on the region they connect to, diffusion is differentially orientated. This will allow us not only to segment the thalamus but also its nuclei.

The thalamus and its nuclei are structures that are hardly differentiated using other imaging modalities such as Computerized Tomography or conventional Magnetic Resonance Imaging (MRI), which do not provide the necessary image contrast. Therefore, radiological identification of the individual thalamic nuclei is not currently possible and even the thalamus precise boundaries are difficult to identify. Often it is segmented by atlas matching or by hand.

The thalamic cytoarchitecture is divided into several nuclei, each with a specific function. The thalamic nuclei have traditionally been studied with histological methods and their number varies depending on the method used. However, most studies identify 11 major nuclei, some of them being subdivided. Wiegell et al. [108] have shown how Diffusion Tensor MRI (DT-MRI) can differentiate the principal thalamic nuclei, non-invasively, basing on the characteristic fiber orientation, which is assumed to stay the same within one certain nucleus and varies from one nucleus to another. Identification of the thalamic nuclei in DT-MRI has also been done by Behrens et al. [14] by performing tractography between the thalamus and the cortex. Thalamic subregions were identified through their specific cortical connectivity.

## 7.5 Results and validation

### 7.5.1 Synthetic data set

In Figure 7.2 the regions have been segmented on the synthetic tensor field without any noise added. The results are displayed as curves on a background color that represents the result from the k-means algorithm [108]. It seems that our method is better to segment the regions that are more elongated. The k-means clustering algorithm weights the distance between the tensors as well as the similarity between them and when they are far apart they get more easily attributed to another region. If the algorithm puts more weight to the similarity than the spatial distance, the clusters become less centered and non-connected clusters can appear. In Figure 7.2 the same segmentations have been made on a field with a  $\text{SNR} = 32$ .

### 7.5.2 Segmentation of the thalamus

For the segmentation of the thalamus, a bloc of the complete images containing the desired structure was selected. With an a priori knowledge of brain anatomy several surfaces were initiated manually in the different structures by looking on color maps [77]. A typical choice of initial surfaces can be seen in Figure 7.3. The high resolution of our images makes a clear distinction between regions so that there is a significant difference between the anterior and the posterior part of the thalamus. We therefore initiate two surfaces, one surface for the anterior part and one surface for the posterior part of the thalamus. The posterior part itself is one of the nuclei, the pulvinar nuclei.

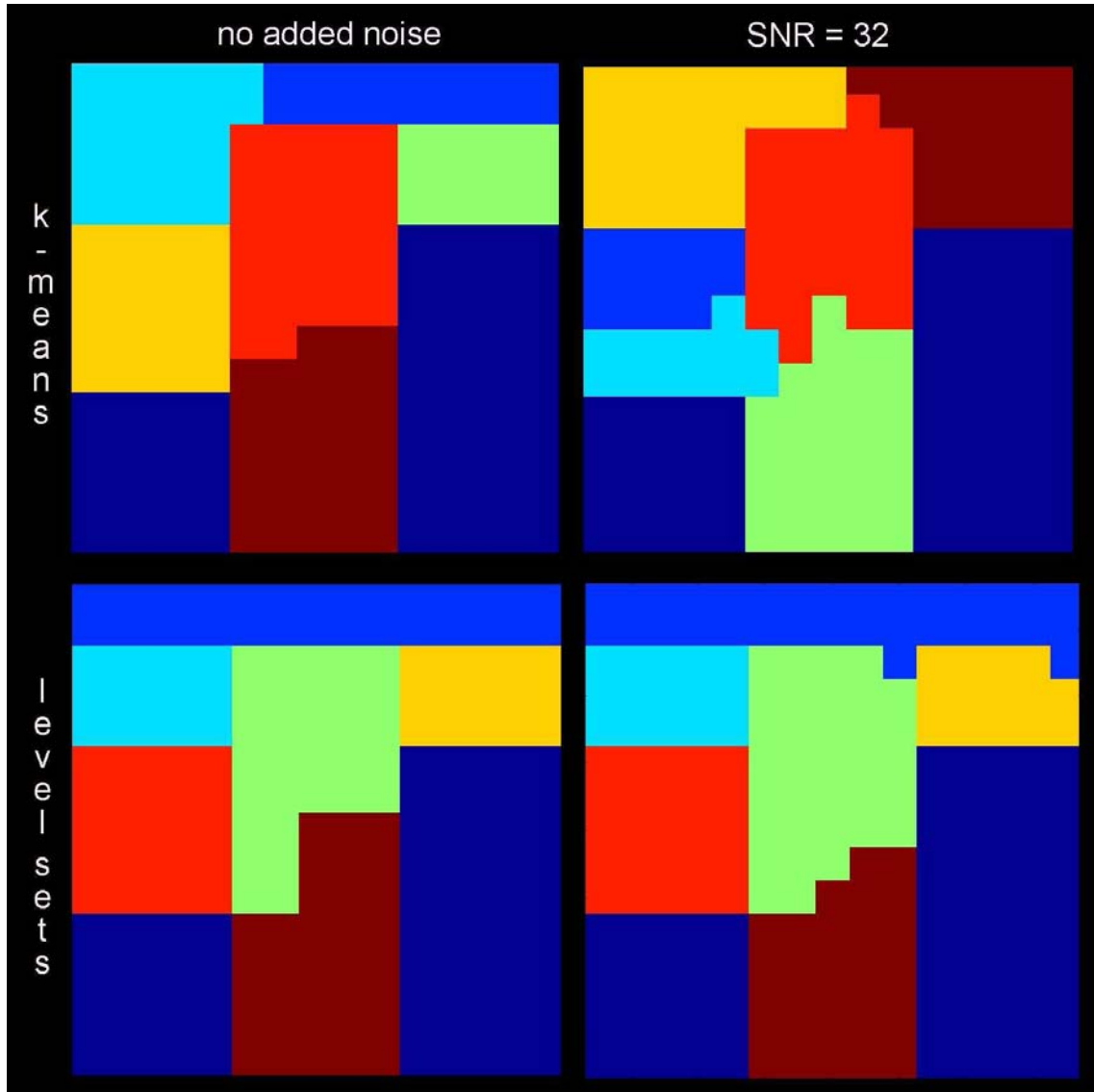


**Figure 7.2:** A cut of the segmentation result on a synthetic field. First line contains the results from the k-means algorithm [108]. The second line is the results with the method presented in this chapter. First column shows results without any noise added. Second column with  $\text{SNR} = 32$ . The level set methods results in a better segmentation for elongated structures and when noise is present and also seems more robust to noise.

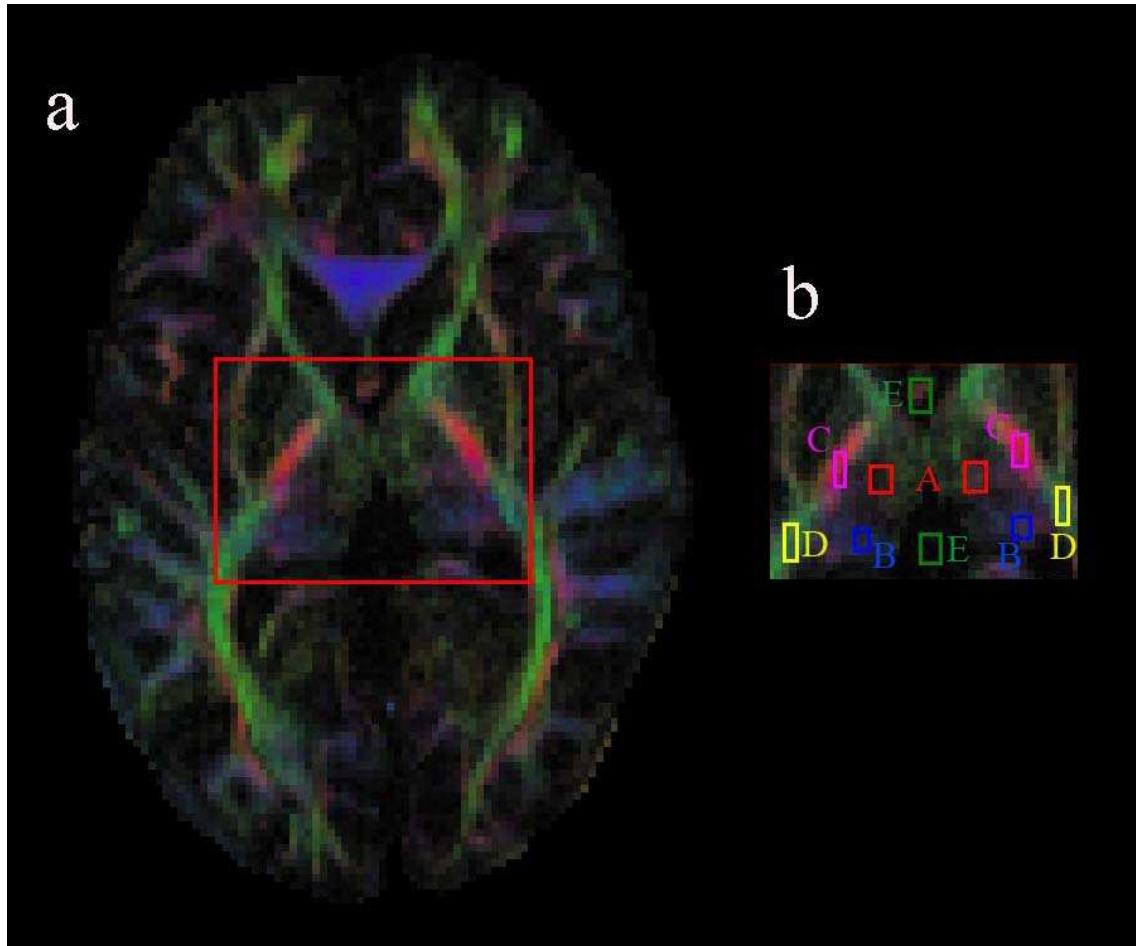


**Figure 7.3:** Placing of the initial surfaces for the segmentation of the thalamus. a) Color map of a horizontal section of a tensor field. b) The selected cut where the segmentation algorithm is run with the initial surfaces. They aim to segment the following structures: A: Thalamus anterior, B: Thalamus posterior (pulvinar nuclei), C: Capsula interna, crus posterior (cortico spinal tract), D: Radiato optica and Fasciculus longitudinalis superior, E: The third ventricle.

The thalamus has been segmented on two different subjects. The results for one of the subjects can be seen in Figure 7.4, Figure 7.5 and Figure 7.6.

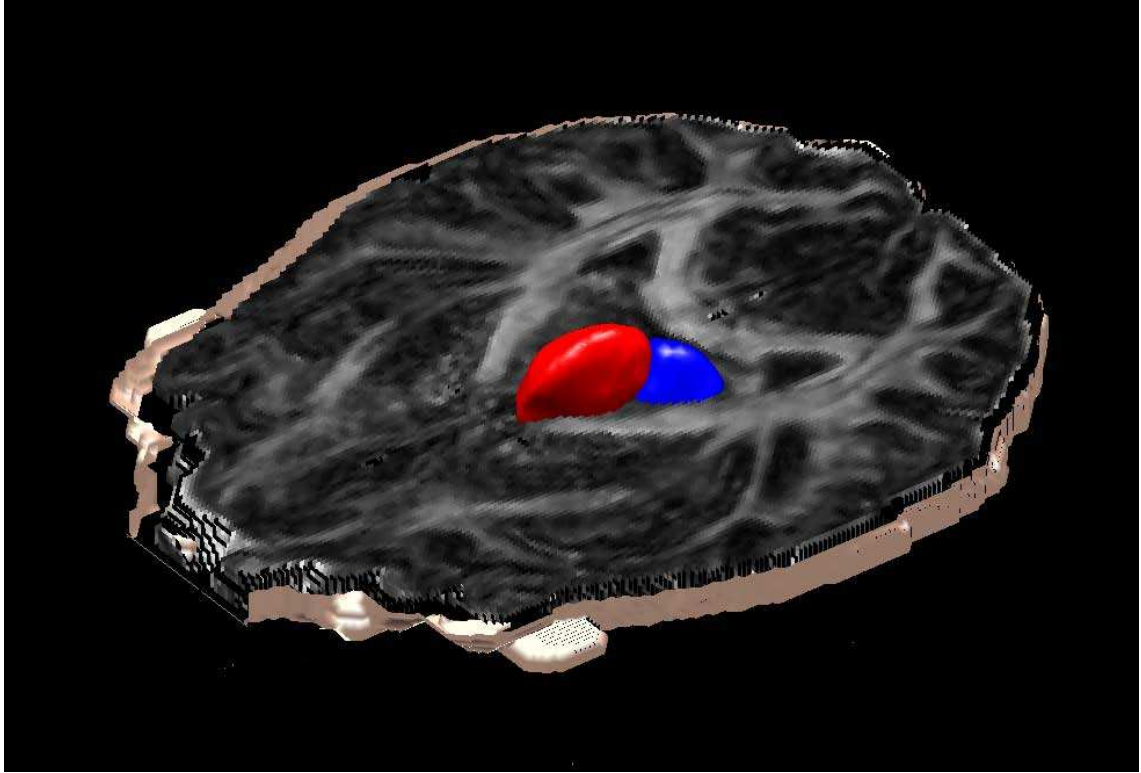


**Figure 7.4:** The segmentation of the thalamus displayed as a 3D surface on a horizontal cut of the fractional anisotropy map. The anterior (red surface) and posterior part (pulvinar nuclei, blue surface) are segmented separately.

Taking the segmentation one step further we have segmented the thalamic nuclei. For this the thalamus segmentation is used as a mask. The surfaces are initialized by running the k-means algorithm by [108]. The center of each cluster was then used as initial points for the surfaces. The results can be seen in Figure 7.7, Figure 7.8 and Figure 7.9. From the result the different nuclei have been identified by an expert by comparing with the Schaltenbrandt atlas (SWSA) [86] that was co-registered on the resulting segmentation of thalamic nuclei. Figure 7.10 shows the correlation between axial slices of the segmented thalamus performed 2 and 7 mm above the anterior commissure(AC)- posterior commissure(PC) plane. The nuclei could be identified as follows: Pu: Pulvinar, Ce: nucleus centralis, M : nucleus medialis, A : nucleus anterior, Lp : nucleus lateropolaris : Zc+Zim+Zo : nucleus Zentrooralis caudalis, intermedius and oralis, Tmth: tractus mamillothalamicus, Vc: nucleus ventrocaudalis, Vim: nucleus ventralis intermedius, Vo: nucleus ventrooralis.

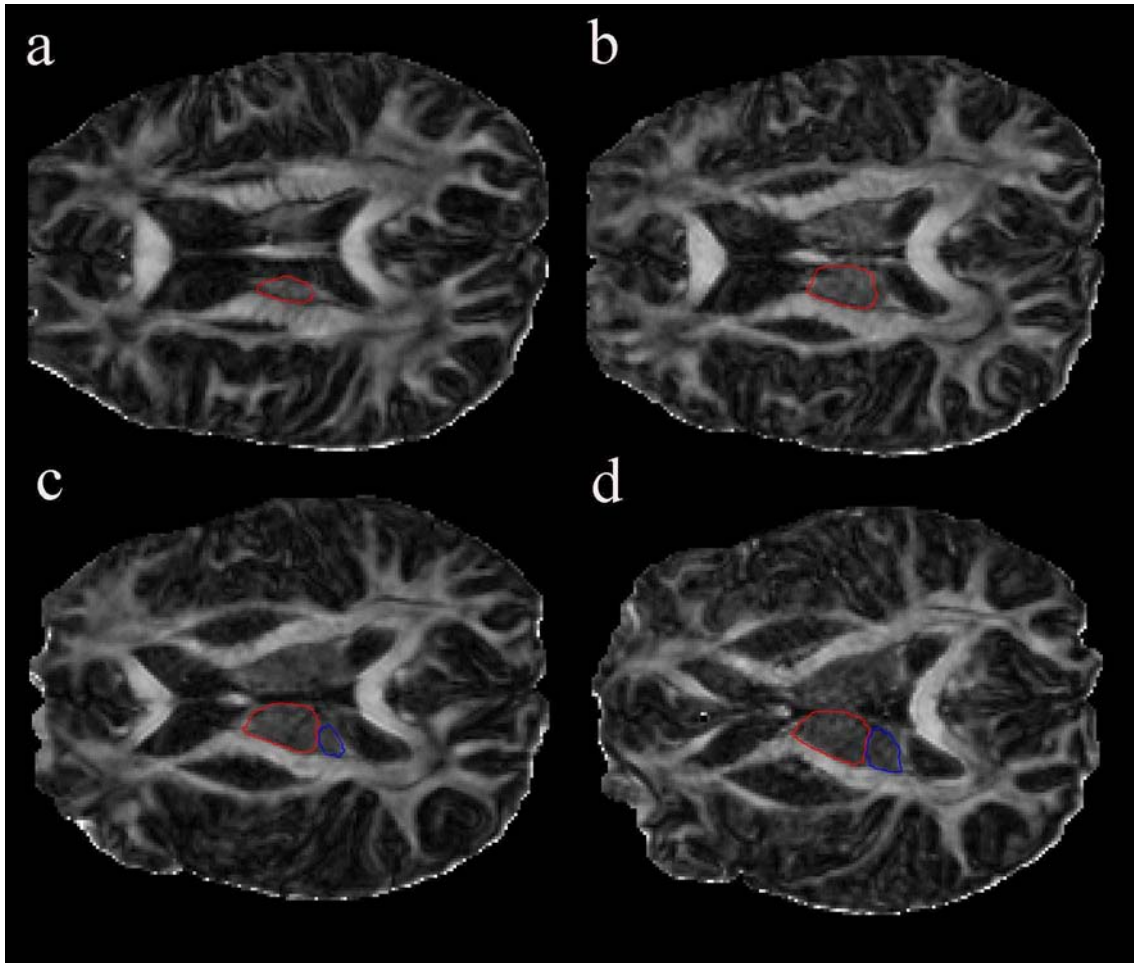


**Figure 7.5:** The segmentation of the thalamus displayed on horizontal cuts of the fractional anisotropy map. The anterior (red surface) and posterior part (pulvinar nuclei, blue surface) are segmented separately.

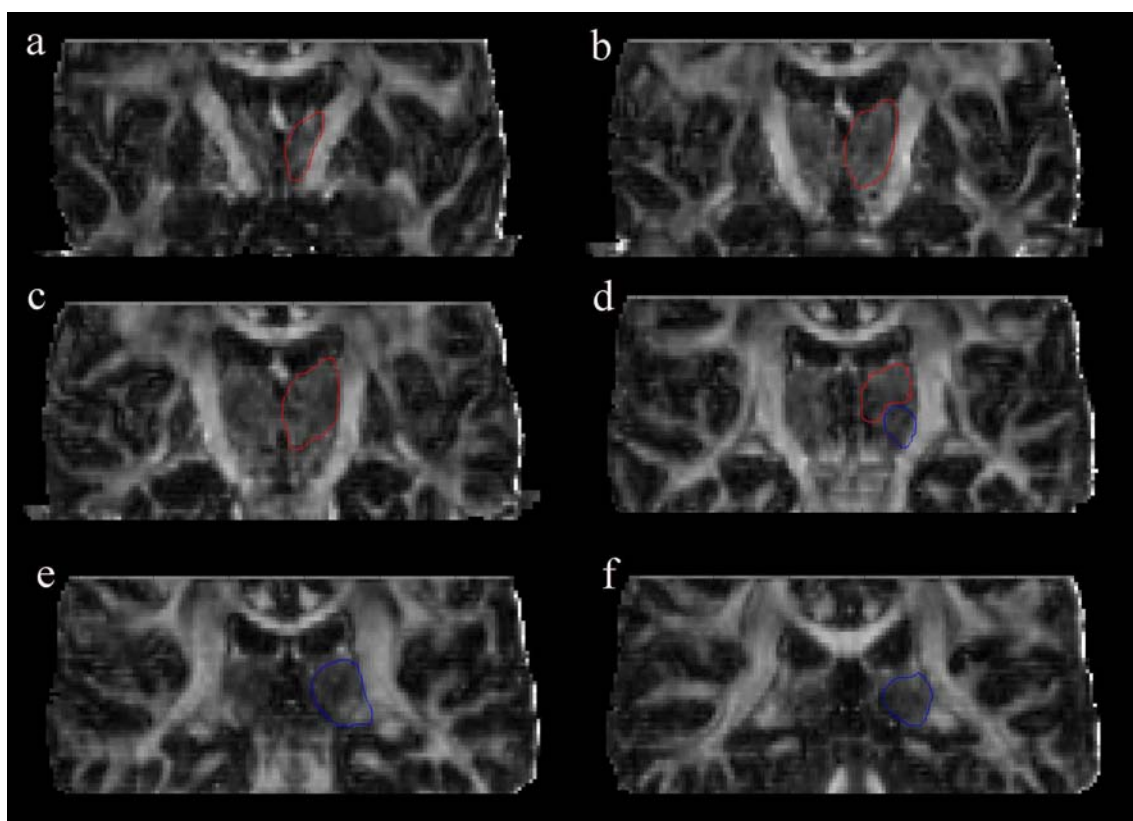


**Figure 7.6:** The segmentation of the thalamus displayed on coronal cuts of the fractional anisotropy map. The anterior (red surface) and posterior part (pulvinar nuclei, blue surface) are segmented separately.



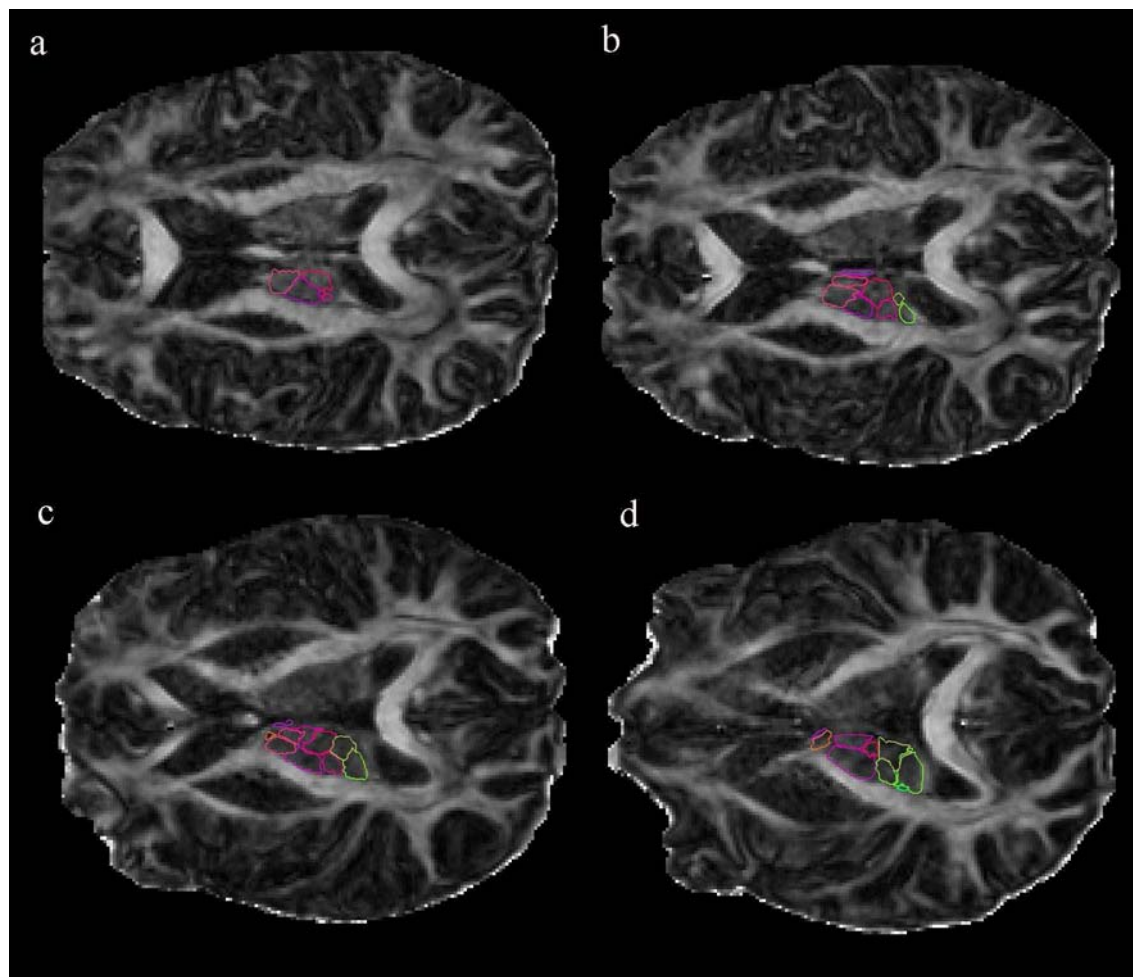


**Figure 7.7:** The segmentation of the thalamic nuclei displayed on horizontal cuts of the fractional anisotropy. Segmentation is made in 14 parts.



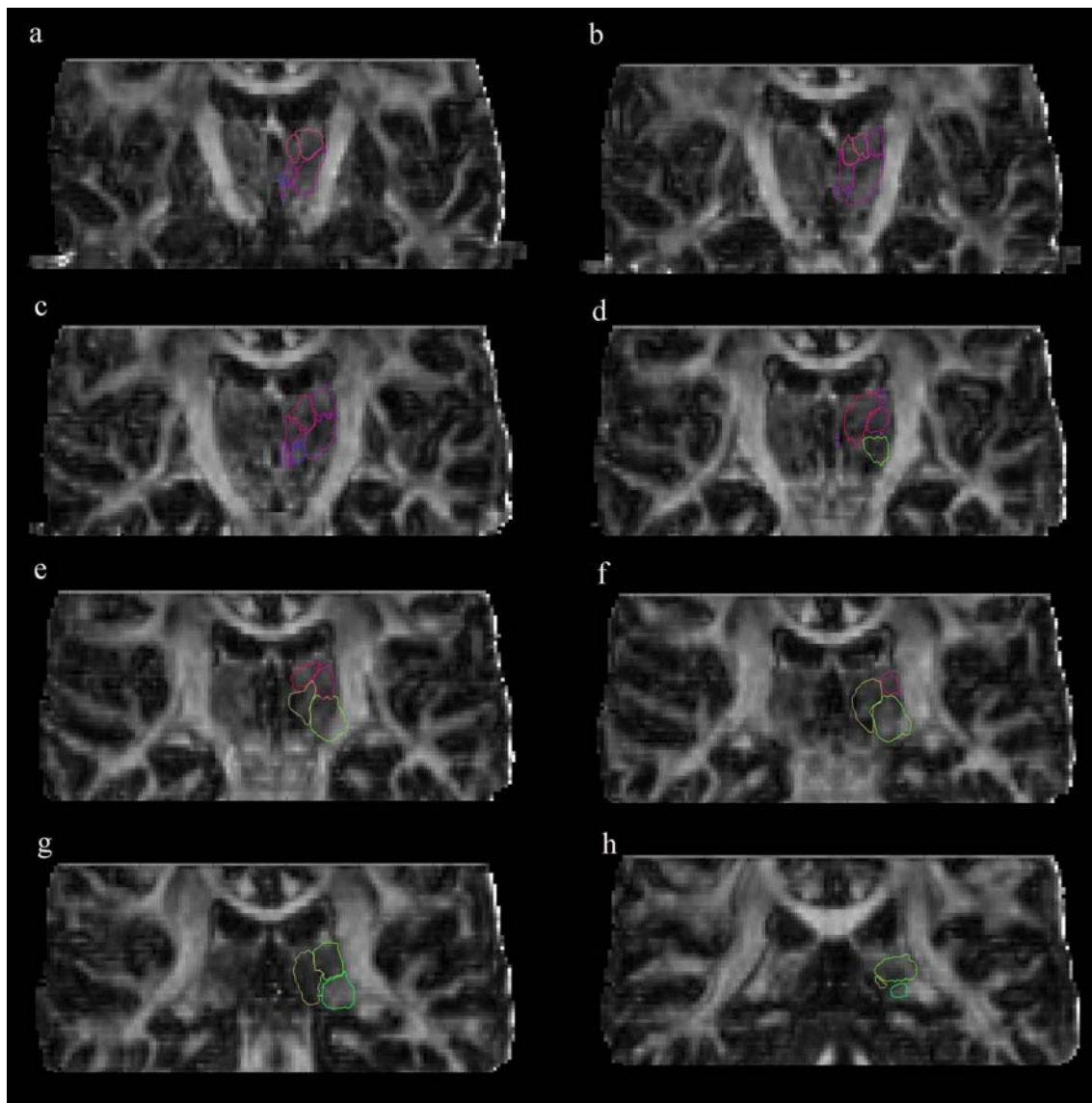


**Figure 7.8:** The segmentation of the thalamic nuclei displayed on coronal cuts of the fractional anisotropy. Segmentation is made in 14 parts.

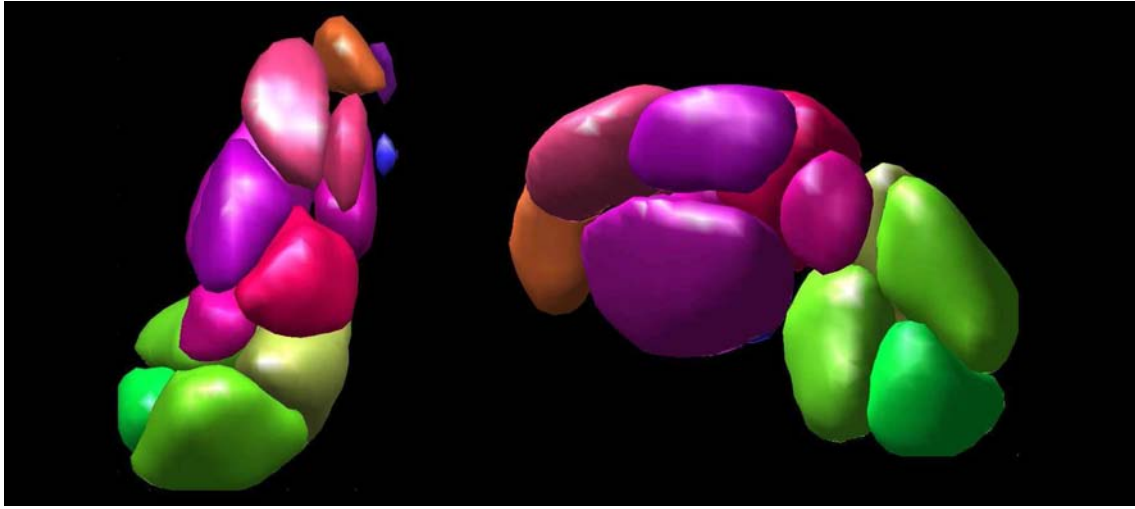


**Figure 7.9:** The segmentation of the thalamic nuclei seen in 3D. Segmentation is made in 14 parts.

## 7.6 Application of tensor segmentation in fluid dynamics

Diffusion Imaging is not the only domain in which tensor representations are used. The tensor notation is a very common tool in fluid dynamics. The purpose of the tensors remains the same as in diffusion, namely description of fluid motion. As in diffusion imaging the fluids are treated on a macroscopic level governed by the *continuum hypothesis* that reconciles the discrete molecular nature of the fluids (microscopic description) with the continuum view (macroscopic description). In fluid dynamics there exists a length scale that determines the appropriate view.

In this section we will focus on the most common fundamental class of fluids known as Newtonian incompressible fluids. A fluid is described by a continuum density field,  $\rho(\mathbf{x}, t)$ , and velocity field,  $\mathbf{U}(\mathbf{x}, t)$ . In an incompressible fluid we have that  $\rho(\mathbf{x}, t) = \text{constant}$ . The behavior of the velocity field is governed by the Navier-Stokes equation:

$$\frac{\partial u_i}{\partial t} + u_j \frac{\partial u_i}{\partial x_j} = \frac{\partial p}{\partial x_i} + \frac{1}{Re} \frac{\partial^2 u_i}{\partial x_j \partial x_j} + \frac{\partial u_i}{\partial x_i}. \quad (7.10)$$

This is the dimensionless version of Navier-Stokes where  $u_i$  is the velocity in direction  $i$  and  $p$  is the pressure. The first term:

$$\frac{\partial u_i}{\partial t},$$

is the conservation of momentum and the last term:

$$\frac{\partial u_i}{\partial x_i},$$

governs the mass conservation.  $Re$  is the Reynolds number that characterizes the flow. It is expressed as a function of the characteristic length,  $L$ , speed,  $U$  and molecular viscosity,  $\nu$ :

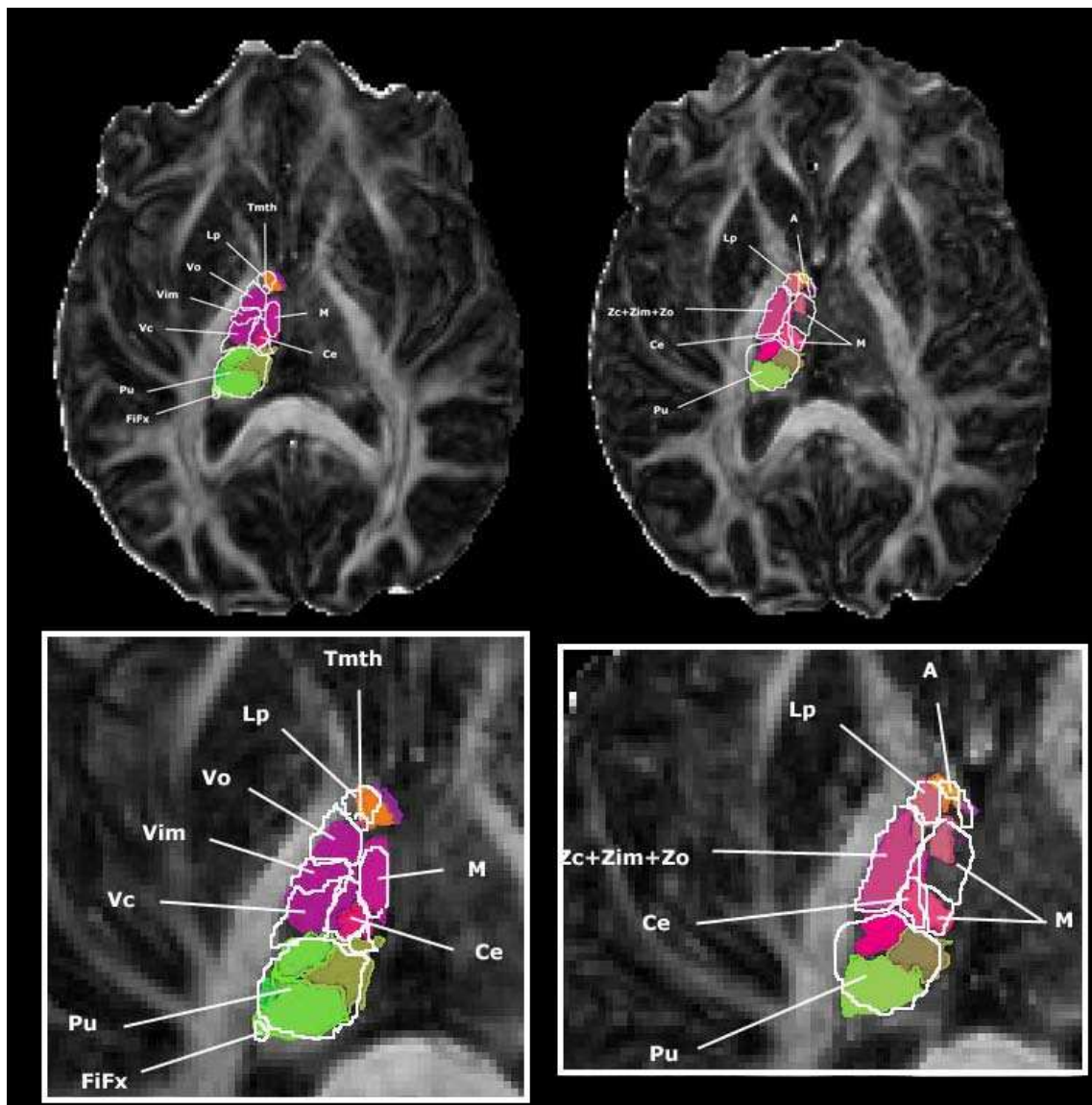


**Figure 7.10:** The segmentation of the thalamic nuclei co-registered with SWSA. For identification of the nuclei, see text.

$$Re = \frac{UL}{\nu}.$$

For small Reynolds numbers,  $Re \rightarrow 0$ , the flow is considered laminar and for  $Re \rightarrow \infty$  the flow is turbulent. An often studied case is the transition between the two types of flows. In the turbulent case it can be useful to decompose the velocity field  $\mathbf{U}(\mathbf{x}, t)$  into:

$$\mathbf{U}(\mathbf{x}, t) = \langle \mathbf{U}(\mathbf{x}, t) \rangle + u(\mathbf{x}, t) \quad (7.11)$$

where  $\langle \mathbf{U}(\mathbf{x}, t) \rangle$  is the mean velocity field and  $u(\mathbf{x}, t)$  its fluctuation which average over time  $\langle u(\mathbf{x}, t) \rangle = 0$ . This separation is referred to as *Reynolds decomposition*. The case we will study later on is a flow constant in the mean,  $\mathbf{U}(\mathbf{x})$  which means that  $\partial U_i / \partial t = 0$ . Using this property and substituting with this decomposition in Eq. (7.10) gives us the Reynolds averaged Navier-Stokes equation:

$$U_j \frac{U_i}{x_j} = \frac{\partial p}{\partial x_i} + \frac{1}{Re} \frac{\partial^2 U_i}{\partial x_j \partial x_j} + \frac{\partial}{\partial x_j} \langle u_i u_j \rangle. \quad (7.12)$$

$$\frac{\partial U_i}{\partial x_i} = 0.$$

The interaction between the mean and the fluctuating field is described by the covariance term  $\langle u_i u_j \rangle$ , known as the *Reynolds stress tensor*. The Reynolds stress tensor shows the interaction between the fluctuating and field and the mean field. We will not go further into details about the flow equations but focus on the Reynolds stresses. The Reynolds stresses are components of a second-order symmetric tensor, just as the diffusion tensor. In spite of this similarity, the Reynolds stress tensor (RST) have some properties that the DT does not. In the RST, each component has a specific meaning. The diagonal components ( $\langle u_1^2 \rangle, \langle u_2^2 \rangle, \langle u_3^2 \rangle$ ) are the *normal stresses* and the off-diagonal components are *shear stresses*. The trace that for the DT corresponds to the mean diffusion is for the RST the definition of the *turbulent kinetic energy*,  $k(\mathbf{x}, t)$ :

$$k = (\langle u_1^2 \rangle + \langle u_2^2 \rangle + \langle u_3^2 \rangle) / 2. \quad (7.13)$$

This is the turbulent kinetic energy per the unit mass in the fluctuating velocity field.

The concept of anisotropy is also used in fluid dynamics. The isotropic stress is  $\frac{2}{3}k\delta_{ij}$  and the anisotropic stress is the deviation of the isotropic part.

$$a_{ij} = \langle u_i u_j \rangle - \frac{2}{3}k\delta_{ij}. \quad (7.14)$$

Even though the DT and RST differs in the meaning of their components the tensors still have the same properties such as being, for 3D flows,  $3 \times 3$  symmetric tensors. We therefore decided to try if we could identify zones of different flow properties by applying our tensor segmentation algorithm to a set of RST.

The data we used were obtained from a simulation of the motion of a Newtonian fluid within a lid-driven cubical three-dimensional cavity. The flow is maintained by the continuous diffusion of kinetic energy from the moving wall carried out at Reynolds numbers

above 10 000, see Figure 7.11 and Leriche et al. [66] for more details on the experiment and numerical simulation. The data were obtained by a direct numerical simulation which "consists in solving the full, non-linear time dependent Navier-Stokes equations without any empirical closure assumptions for described initial and boundary conditions" [62]. The part of the data we used were the RST obtained from the static mean flow.

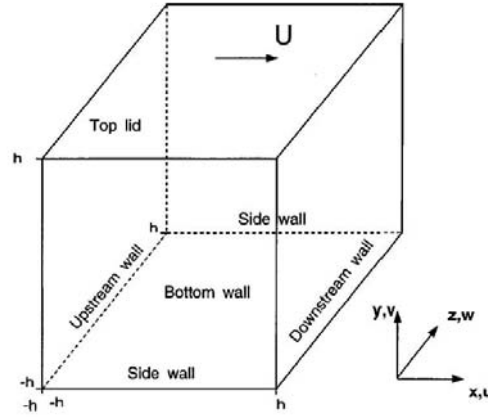


**Figure 7.11:** Experimental set up of the lid-driven flow. The image shows the flow domain and axes system. Reynolds number is given by  $Re = U_0(2h)/\nu$ . Figure copied from [66].

We started by computing the fractional anisotropy and color maps to see if these had a meaning for the RST. Slices from these maps are shown in Figure 7.12. Cuts are shown along each axis  $(x, y, z)$  at  $-0.93h$ ,  $-0.5h$  and  $0h$ . The cuts at  $(x, y, z) = -0.93h$  provides representation of the near wall behavior which is expected to be very anisotropic. The walls are situated at  $\pm 1h$ . The planes  $(x, y, z) = 0h$  are the planes of statistical symmetry.

The second important question to answer was whether the similarity measure we used for the DT segmentation has a meaning for the RST. It is clear that the direct sense as percentage of common diffusion between two sensors will not be the same. However, it remains a good comparison of the kind of flow each tensor represents. As a first attempt we simply applied our existing algorithm on the data. The results are shown in Figure 7.13. For comparison the figure from [66] are included in Figure 7.14.

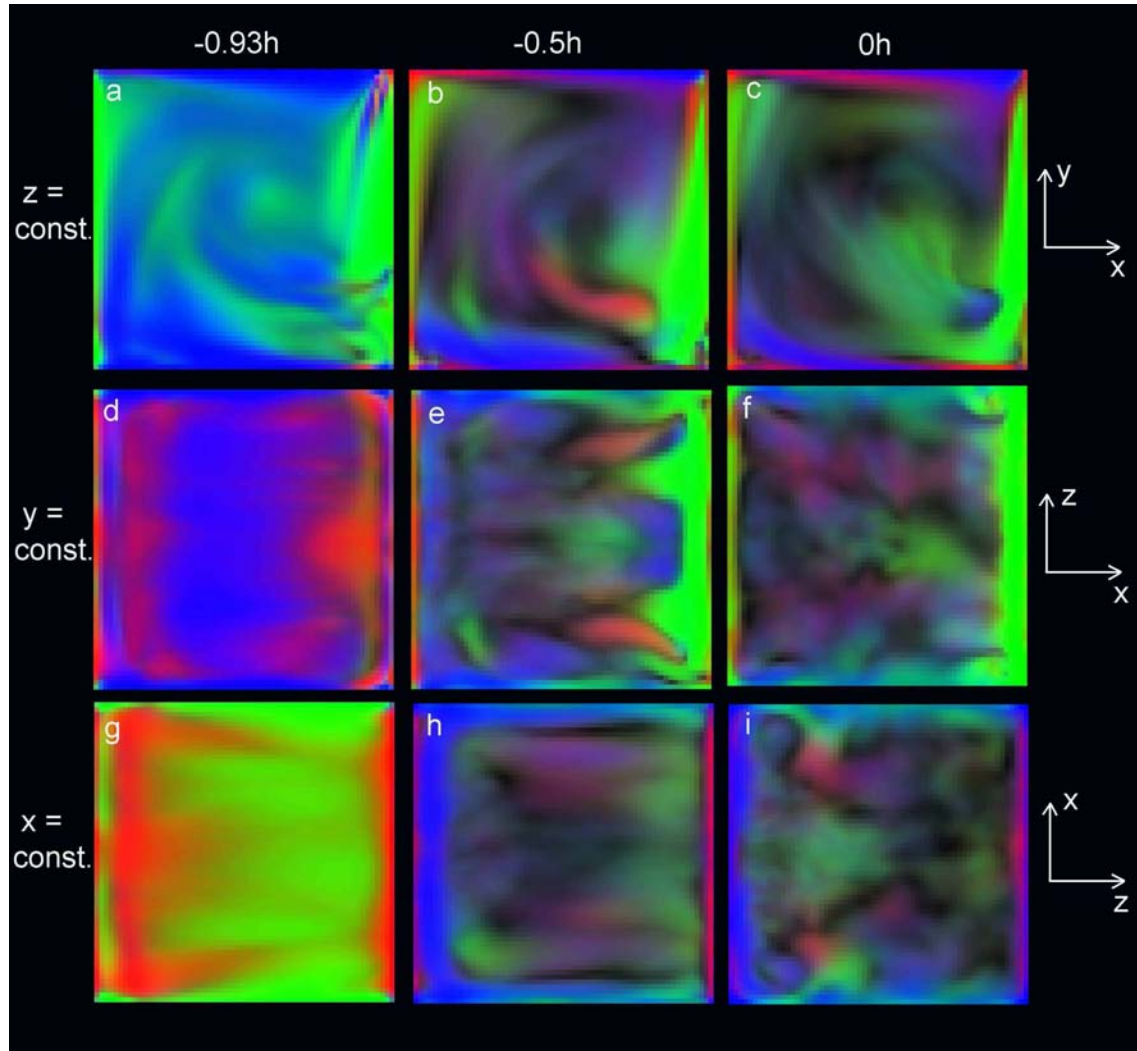


**Figure 7.12:** Color map slices of the Reynolds stress tensors from a flow in a lid-driven cubical cavity. a-c shows the  $xy$ -plane, d-f shows the  $xz$ -plane and g-i the  $yz$ -plane. a, d and g shows the plane at  $-0.93h$  along the  $z$ -,  $y$ - and  $x$ -axis respectively. b, e and h shows the plane at  $-0.5h$  and c, f and i at  $0h$ .



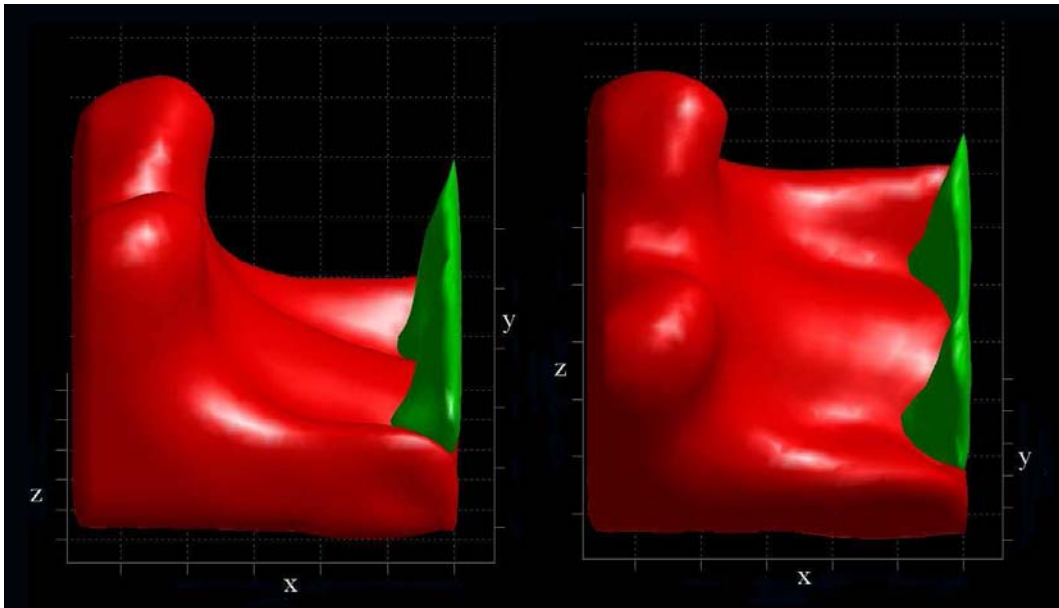


**Figure 7.13:** Results from segmentation of Reynolds stress tensors obtained from a flow in a lid-driven cubical cavity.

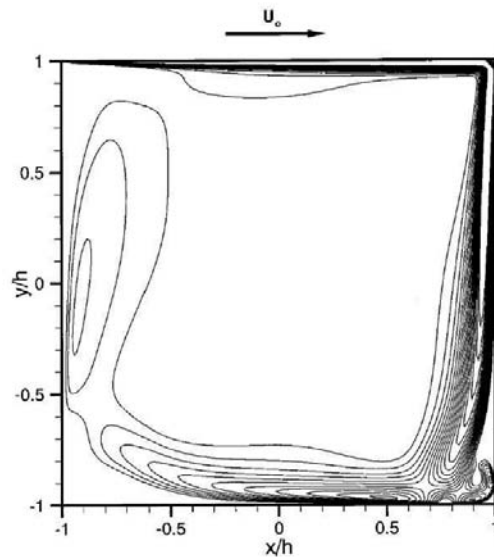


**Figure 7.14:** Results from article by Leriche et al. [66]. The figure shows level curves for  $\sqrt{U_1^2 + U_2^2}$  at the plane  $z = 0.427h$ .

## 7.7 Discussion and Conclusion

In this chapter we presented a new method for segmenting tensor fields by using similarity tensors. Compared with the previous chapter in which we used a similarity measure that favored anisotropic regions, this measure shows strictly the percentage of common diffusion between two tensors. The similarity is used to define an energy functional from which region based forces can be derived. These forces drive a set of coupled level sets towards the optimal segmentation. The method has been applied to DT-MRI of gray matter and to fields of RST from fluid dynamics. In gray matter, the method has shown to be capable of distinguishing and separating regions with only very subtle differences in diffusion such as the difference between the thalamic nuclei. The application on RST is an early work but shows promising results for enhancing the contrast between the different properties of the flow. Furthermore, it shows that our proposed method can be used outside the diffusion imaging domain. This is a first attempt to apply our method on different kinds of tensor data. The application has been made without any modification of the method and we can already see that it can be useful as a complementary visualization tool for 3D flows. By modifying the similarity measure to better take into account the specific features of each tensor component we can anticipate an even better result.

The method we propose to segment the thalamus and the thalamic nuclei is a continuation of our work on fiber tract segmentation. It distinguishes itself on three main points. The first main difference of our approach is the similarity measure we use. It is capable of detecting very subtle changes between tensors. When segmenting gray matter structures these subtle differences are more important than for white matter segmentation. The second important point in our work is the choice of the most representative tensor of each level set. The approach proposed by Wang et al. [102] is to compute a mean tensor for each region. For regions with high inter-resemblance, the mean tensor has a tendency of developing towards an isotropic tensor and all regions will then be associated to similar tensors. This can be avoided by using a method proposed by Jones et al. [61] that was originally used to find the tensor image that best represented a whole set of images. We have transformed this method to find the tensor that best represents the set of tensors contained within a surface. The third important difference is the use of several coupled level sets that each represent a region we wish to segment. When segmenting structures with such complex architecture as the brain, simply separating foreground and background is mostly insufficient. Using such a simplification leads to either an over- or under segmentation of the desired structure. Using several coupled level sets, each representing a region increases robustness of the method.

When comparing results with the k-means algorithm we can state that the advantages of the k-means algorithm are that it is fast and does not require any pre-initialization. The advantages of our methods are a higher flexibility regarding the shape of the nuclei and that it diminishes the influence of noise due to the self-regularization of the surfaces. It is also difficult to include other similarity measures than direct comparison of tensor elements in the k-means algorithm. Using the level set method we have more liberty to choose features



on which we wish to base our segmentation.

The method generates good results for segmentation of the thalamus. As for the thalamic nuclei, our validation study shows that the level set method applied on DT-MRI of the thalamus provides an overall consistent segmentation of the thalamic nuclei related to their anatomical position defined by the SWSA. For some nuclei (pulvinar), it was even able to show subdivisions within the structure, already described in the SWSA. For others (nucleus ventralis or zentrooralis), it could not recognize the caudal, intermediate and oral portions of the nucleus.

The work on segmentation of the thalamus and its nuclei have been presented in [60] and submitted to [59]. It is currently used in a project for finding the thalamus of schizophrenic patients with the purpose of tracking fibers between the thalamus and the cortex. An example of their early results can be seen in Figure 7.15.

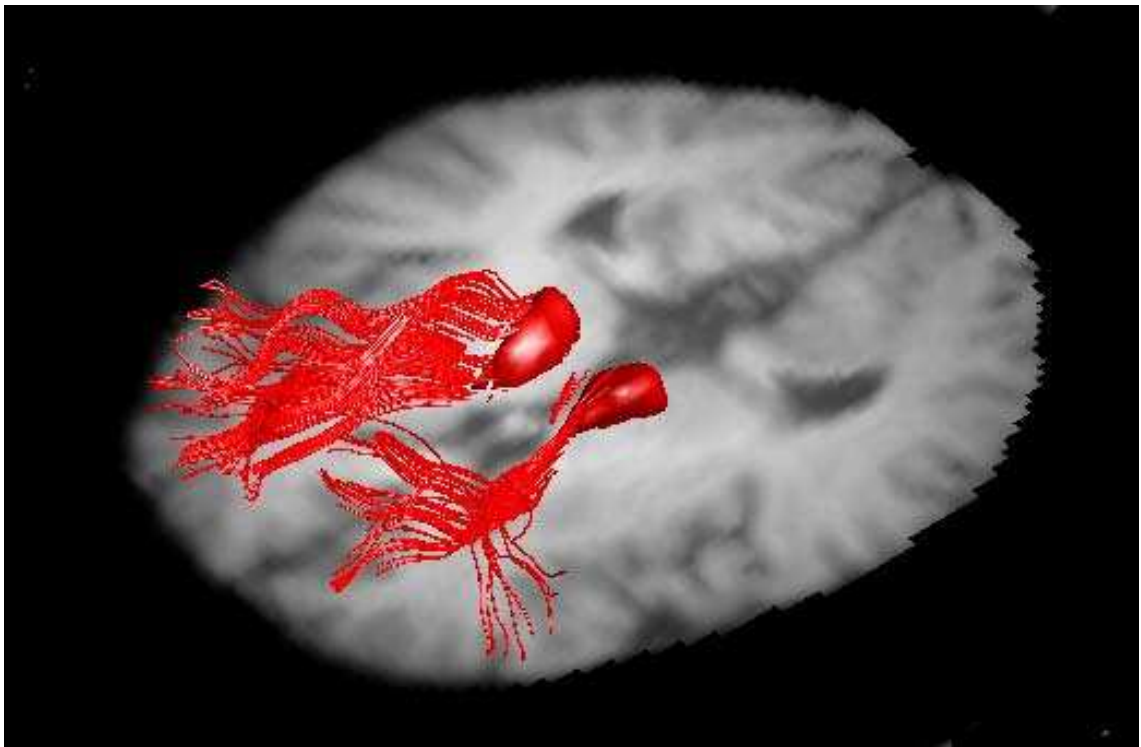


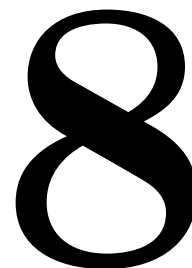
**Figure 7.15:** Fiber tractography between the thalamus, segmented by our method, and the cortex. Early results from a study on schizophrenic patients. Image presented with courtesy of Leila Cammoun.



---

# Discussion and conclusion

---



## 8.1 Review of discussed topics

Throughout this thesis we have explored the possibilities provided by the level set framework for analysis of multi-valued images. Segmentation methods for tensor fields such as Diffusion Tensors Images (DTI) as well as fields of functions i.e. High Angular Resolution Diffusion (HARD) images have been presented.

For segmentation of tensor fields we have explored similarity measures for comparison of tensors that depend on the specific case we wish to study. For white matter segmentation in DTI the similarity measure emphasizes anisotropic regions, which is favorable for this particular purpose. The segmentation is made on a local basis since white matter, in general fiber tracts, experiences different diffusion in different parts of the structure. Structures such as the deep cerebral nuclei that are mainly composed of gray matter have more homogenous diffusion properties so in these structures we seek to maximize the internal coherence within the entire structure. We can therefore have a region based approach to the segmentation problem. This region based method has also been applied to tensor field in fluid dynamics which demonstrates the generality of the problem.

For HARD images two methods for fiber tract segmentation have been presented based on two different types of coherence. The coherence is either measured as the similarity between fibers obtained from a tractography algorithm or the similarity of scalar values in a five-dimensional non-Euclidean space. The similarity between two fibers is determined by a counting strategy and is equal to the number of voxels they have in common. A spectral clustering algorithm is then used for grouping fibers with a high inter-resemblance. When segmenting white matter with the level set method we propose to expand the space we are working in from a three-dimensional space of ODFs to a five-dimensional space of position and orientation. This new high dimensional space is non-Euclidean but scalar and

regions crossing in three dimensions become clearly separated regions in five dimensions. By a careful definition of this space and an adaptation of the level set to five dimensions the fibers can be segmented as separated structures using a Chan-Vese level set model for region-based segmentation for gray scale images.

## 8.2 Achievements

1. A novel approach to segmentation of tensor fields by using measures of similarity.
2. A fully automatic spectral clustering algorithm for grouping of fibers from HARDI, based on the counting of voxels in common between fibers, has been developed. The algorithm is fast, simple to implement and shows very promising results. It has a great opportunity of becoming a helpful tool for visualization of fiber tractography results as it provides a clear contrast between the major tracts as well as the cortical zones. This work has been presented in [58].
3. A local front propagation algorithm based on tensor similarity. The algorithm is used for fiber tract segmentation in DT-MRI. This work has been presented in [57] and published in [55].
4. A region based approach for segmentation of tensor fields by maximizing the coherence within each region. The method was applied to segmentation of structures mainly composed of gray matter in DT-MRI using a region-based level set method. A new way of representing regions by an appropriate choice of the most typical tensor of the set of DT contained within the region was presented together with a new similarity measure especially designed for detection of very subtle changes between DTs. We presented segmentations of the thalamus and its nuclei that were validated by an expert and superposition of anatomical atlases. This work has been presented in [60] and is submitted for publication in [59].
5. A novel representation of HARD data was presented that extends the three-dimensional view of diffusion functions to a five-dimensional space of scalars. A level set method was implemented in 5D taking into consideration the non-Euclidean topology of the space and the mean-curvature in this high-dimensional space. This will be presented in [56].

## 8.3 Potential applications

Localization and definition of structures has numerous potential applications in medicine. There are several advantages by considering white matter tracts as an entity with a clear delineation of the structural borders instead of separate fibers. Firstly, it simplifies quantification of the diffusion which is of highest importance for clinical studies. Secondly, clearly delimited structures are more practical to use in direct clinical applications such as neurosurgical planning.

Our thalamus segmentation method is currently applied in a study of the pre-frontal cortico-thalamic projections in schizophrenic patients where the thalamus segmentation is used as a departure point for the fiber tractography algorithm. Several studies concerning the shape and volume of the thalamus have also been used in studies of schizophrenia. Despite the advanced development in medical image analysis, the localization of most structures is currently made by hand from anatomical MRI. This is both time consuming and subjective. An automatization of this procedure would greatly improve the conditions under which the clinical studies are made today. Further, diffusion weighted MRI can provide an enhanced contrast for many structures as a more complete description of the structure properties is given.

The principal application of the clustering algorithm is to enhance the imaging contrast even further by providing a clear distinction between different white matter structures. Its great advantage is its simplicity and rapidity and that it is operating on data from fiber tractography which is becoming a frequently used tool. By mapping the fibers back into voxel space a quantification of the diffusion can also be made.

## 8.4 Discussion and future directions

A striking problem today is the big gap between tools used in clinical research and the technical possibilities developed in the image processing labs. The majority of all clinical research based on diffusion imaging use scalar simplifications such as fractional anisotropy and mean diffusion that are the most accessible and quantifiable measures. To ensure that our technological advances in the image analysis field becomes more than just a playground for computer scientists it is important that the tools we develop are reliable, user friendly and provide quantitative results for inter-subject comparisons. Concerning the reliability one important question to address is whether we can trust our images on which our analysis is founded. The diffusion tensor images are a great simplification of the underlying neuronal architectonics but as the angular and spatial resolution increase, as in DSI, the images becomes more anatomically plausible [105]. This argues that these images provide a meaningful representation of the cerebral anatomy but are still in need of further improvement and validation. Despite the higher precision and anatomical correspondence of DSI compared to DTI only DTI is today clinically feasible due to the long acquisition times of DSI. Even though the acquisition times can be reduced the low SNR remains a problem. Continuing to explore tools for analyzing DTI in parallel with DSI is therefore still of interest. Assuming that we can trust our images we still need a profound validation of the methods before they can be used in clinical practice.

Diffusion imaging is a new and continuously developing technology and there are endless possibilities of new developments to make for better exploitation of these new diffusion data. Recent developments even permit investigations of gray matter such as cortex. A key problem is quantification which is more complicated for DSI than for DTI. This is a problem that just very recently has been addressed [33]. We will not discuss the general possibilities of diffusion imaging but focus on the future paths for the tools developed in

this thesis.

#### 8.4.1 Region based segmentation of tensor fields

The most complete tool developed in this thesis is the region based segmentation of structures mainly composed by gray matter (see Chapter 7). This method can, with the right initialization segment many other structures that the thalamus, such as the remaining deep cerebral nuclei. The method in its present stage is close to becoming a practical tool and what is mostly needed are automatic procedures for initialization of the algorithm. A general problem with the level set method is that the solution is a local minimum and is therefore be dependent on the initialization. This problem could be avoided by developing hybrid methods that use a different segmentation method for a coarser pre-segmentation and letting the level set method do the fine-tuning. Another solution is using multi scale segmentation where the object is segmented on different scales obtained by smoothing the image using a total variation flow [46]. Adding a priori knowledge about the shape of structures could also improve the stability of the algorithm [22].

A practical application of the segmentation of the thalamic nuclei is as an aid in pre-surgical planning. Nowadays, one of the most promising treatments of Parkinsons disease is deep brain stimulation, which is a validated approach to place electrode in the thalamus. A precise segmentation of the thalamus leads to more safe interventions and improved success rate. Other practical applications are investigation of brain diseases such as stroke that are known to affect the thalamus [25] [52].

In order to further validate our algorithm, one of our short term plans is to scan a pathologic brain post mortem for possible application of our segmentation algorithm.

#### 8.4.2 Position-orientation space

Considering the 3D maps of ODFs obtained from HARDI as a 5D space of scalars open up for many new interpretations. This can help us quantifying the diffusion by considering the directions separately. In DSI, the ODF is a simplification of the more detailed PDF which contain a radial dependence which would lead to a six-dimensional space that can provide even more useful information and interpretation.

So far we have only used this 5D space for white matter segmentation but this new way of considering the diffusion maps useful for analysis of gray matter regions such as cortex and deep cerebral nuclei.

Handling data of 5D is a heavy and time consuming procedure. To fully exploit this new image representation current algorithms must be optimized.

#### 8.4.3 Spectral clustering

The adjacency matrix used for fiber clustering is a common concept in network theory. Considering the neuronal fibers as a network is of course nothing new so adapting theories from this domain is a logical step. This aspect has been further developed in [47].

---

The Euclidean space in which we map the fibers is very simple but does not have an anatomical meaning. Using Talairach boxes [92] would provide this meaning and would also make it possible to perform inter-subject clustering of fibers. We will continue to develop the algorithm presented in this thesis.

#### 8.4.4 Distance maps

When segmenting a structure with the level set method the final segmentation is expressed in terms of a distance map where the boundary of the structure corresponds to the zero'th level. This means that every other part of the brain is expressed in terms of closest distance to the segmented structure. This is a concept often used in probabilistic atlas registration. The distance function could also be seen as a map of the probability of being close to the actual object. The distance map could define regions of elevated risk during neurosurgical intervention. These two aspects of the distance maps are something we would like to further explore in our future work.





---

# Bibliography

---

- [1] URL <http://nobelprize.org/>.
- [2] D. Adalsteinsson and J.A. Sethian. A fast level set method for propagating interfaces. *Journal of Computational Physics*, 118:269–277, 1995.
- [3] D. Alexander, J. Gee, and R. Bajcsy. Similarity measures for matching diffusion tensor images. In *Proceedings BMCV'99*, 1999.
- [4] L. Ambrosio and H.M. Soner. Level set approach to mean curvature flow in arbitrary codimension. *Journal of Differential Geometry*, 43:693–737, 1996.
- [5] M Bach Cuadra. *Atlas-based Segmentation and Classification of Magnetic Resonance Brain Images*. PhD thesis, EPFL, 1015 Ecublens, November 2003.
- [6] P.J. Basser, J. Mattiello, and D. Le Bihan. Estimation of the effective self-diffusion tensor from the nmr spin echo. *J. Magn. Reson.*, 103:247–254, 1994.
- [7] P.J. Basser, J. Mattiello, and D. Le Bihan. Mr diffusion tensor spectrography and imaging. *Biophys. J.*, 66:259–267, 1994.
- [8] P.J. Basser and S. Pajevic. Statistical artefacts in diffusion tensor mri (dt-mri) caused by background noise. *Magn Reson Med*, 44(1):41–50, 2000.
- [9] P.J. Basser, S. Pajevic, C. Pierpaoli, J. Duda, and A. Aldroubi. In vivo fiber tractography using dt-mri data. *Magn Reson Med*, 44(4):625–32, 2000.
- [10] P.J. Basser and C. Pierpaoli. Microstructural and physiological features of tissues elucidated by quantitative-diffusion-tensor mri. *J Magn Reson B*, 111(3):209–19, 1996.
- [11] P.J. Basser and C. Pierpaoli. A simplified method to measure the diffusion tensor from seven mr images. *Magn Reson Med*, 39:928–934, 1998.
- [12] P.G. Batchelor, F. Hill, F. Calamante, and D. Atkinson. Study of connectivity in the brain using the full diffusion tensor from mri. In *IPMI*, pages 121–133, 2001.
- [13] C. Beaulieu. The basis of anisotropic water diffusion in the nervous system - a technical review. *NMR in Biomedicine*, 15(7-8):435–455, 2002.

- 
- [14] TE. Behrens, H. Johansen-Berg, MW. Woolrich, SM. Smith, CA. Wheeler-Kingshott, PA. Boulby, GJ. Barker, EL. Sillery, K. Sheehan, O. Ciccarelli, AJ. Thompson, JM. Brady, and PM. Matthews. Non-invasive mapping of connections between human thalamus and cortex using diffusion imaging. *Nat Neurosci.*, 6(7):750–757, 2003.
  - [15] M. Belkin and P. Niyogi. Laplacian eigenmaps and spectral techniques for embedding and clustering. *Advances in Neural Information Processing Systems*, 14, 2002.
  - [16] R. Bellman. *Adaptive control processes: A guided tour*. 1961.
  - [17] C.M Bishop. *Neural Networks for Pattern Recognition*. 1995.
  - [18] F. Bloch. Nuclear induction. *Phys. Rev.*, 70:460–474, 1946.
  - [19] M. Brand and K. Huang. A unifying theorem for spectral embedding and clustering. Technical report, 2003.
  - [20] X. Bresson, T. Butz, and J.-P. Thiran. Anaconda: A new active contour oriented non deterministic approach. Technical Report TR-ITS-2005, Swiss Federal Institute of Technology, Lausanne, Switzerland, 2005.
  - [21] X. Bresson, P. Vandergheynst, and J. Thiran. A variational model for object segmentation using boundary information and statistical shape prior driven by the mumford-shah functional. *International Journal of Computer Vision*, [Submitted]], 2004.
  - [22] X. Bresson, P. Vandergheynst, and J.P. Thiran. A priori information in image segmentation: Energy functional based on shape statistical model and image information. In *Proceedings of International Conference on Image Processing 2003 , ICIP03, Barcelona, Spain*, volume 3, pages 428–428. IEEE, IEEE, September 2003.
  - [23] A. Brun, , H.-J. Park, H. Knutsson, and C.-F. Westin. Coloring of dt-mri fiber traces using laplacian eigenmaps. In *Eurocast, LNCS 2809*, pages 518–529. Springer, 2003.
  - [24] A. Brun, H. Knutsson, H.-J. Park, Shenton M., and C.-F. Westin. Clustering fiber traces using normalized cuts. In *Proceedings of the Seventh International Conference on Medical Image Computing and Computer-Assisted Intervention (MICCAI'2004)*, 2004.
  - [25] F. Buffon, N. Molko, D. Hervé, R. Porcher, I. Denghien, S. Pappata, D. Le Bihan, M-G. Bousser, and H. Chabriat. Longitudinal diffusion changes in cerebral hemispheres after mca infarcts. *Journal of Cerebral Blood Flow and Metabolism*, 25:641–650, 2005.
  - [26] PT. Callaghan. *Principles of nuclear magnetic resonance microscopy*. 1991.
  - [27] J. S. W. Campbell, K. Siddiqi, Baba C. Vemuri, and G. B. Pike. A geometric flow for white matter fibre tract reconstruction. In *International Symposium On Biomedical Imaging*, 2002. URL <http://www.cim.mcgill.ca/~siddiqi/conference.html>.

- 
- [28] V. Caselles, R. Kimmel, and G. Sapiro. Geodesic active contours. *International Journal of Computer Vision*, 22:61–79, 1997.
- [29] V. Caselles, R. Kimmel, G. Sapiro, and C. Sbert. Minimal surfaces: A three dimensional segmentation approach. *Numerische Mathematik*, 77(4):423–451, 1997.
- [30] T.F. Chan and Vese L. A. Active contours without edges. *IEEE Transactions on Image Processing*, 10(2):266–277, 2001.
- [31] C. Ched'hotel, D. Tschumperlé, R. Deriche, and O. Faugeras. Constrained flows of matrix-valued functions: Application to diffusion tensor regularization. In *ECCV (1)*, pages 251–265, 2002.
- [32] Y.G. Chen, Y. Giga, and S. Goto. Uniqueness and existence of viscosity solutions of generalized mean curvature flow equations. *Journal of Differential Geometry*, 33: 749–786, 1991.
- [33] K-H. Cho, Y-P. Chao, Y-C. Li, J-H. Chen, and C-P. Lin. Mapping fiber density distribution with diffusion spectrum imaging. *Proceedings of 13th Annual Meeting ISMRM, Miami*, page 577, 2005.
- [34] S. Clarke, R. Kraftsik, H. van der Loos, and G.M. Innocenti. Forms and measures of adult and developing human corpus callosum: Is there sexual dimorphism. *The Journal of Comparative Neurology*, 280:213–230, 1989.
- [35] T.E. Conturo, N.F. Lori, T.S. Cull, E. Akbudak, A.Z. Snyder, J.S. Shimony, R.C. McKinstry, H. Burton, and M.E. Raichle. Tracking neuronal fiber pathways in the living human brain. *Proc Natl Acad Sci U S A*, 96(18):10422–7, 1999.
- [36] O. Coulon, D.C. Alexander, and S.R. Arridge. Diffusion tensor magnetic resonance image regularisation. *Medical Image Analysis*, 8(1):47–67, 2004.
- [37] R. Courant, K.O. Friedrich, and H. Lewy. On the partial differential equations of mathematical physics. *IBM Journal*, 11:215–235, 1967.
- [38] A. Einstein. *Investigations on the theory of the Brownian movement*. Dover Publications, 1956. Collection of papers translated from the German.
- [39] C. Feddern, J. Weickert, and B. Burgeth. Level-set methods for tensor valued images. In *Proc. Second IEEE Workshop on Variational, Geometric and Level Set Methods in Computer Vision.*, pages 65–72, 2003.
- [40] J. Foong, M. Maier, C.A. Clark, G.J. Barker, D.H. Miller, and M.A. Ron. Neuropathological abnormalities of the corpus callosum in schizophrenia: a diffusion tensor imaging study. *J Neurol Neurosurg Psychiatry*, 68(2):242–4, 2000.
- [41] L.R. Frank. Anisotropy in high angular resolution diffusion-weighted mri. *Magn Reson Med*, 45(6):935–9, 2001.

- 
- [42] IM Gelfand and SV. Fomin. *Calculus of Variations*. Dover Publications, 2000. C.
  - [43] D. Geman. Random-fields and inverse problems in imaging. *Lect Notes Math*, 1427: 113–193, 1990.
  - [44] S. Geman and D. Geman. Stochastic relaxation, gibbs distributions, and the bayesian restoration of images. *IEEE T Pattern Anal*, 6(6):721–41, 1984.
  - [45] H. Gudbjartsson and S. Patz. The rician distribution of noisy mri data. *Magn Reson Med*, 34:910–914, 1995.
  - [46] L. Gui, X. Bresson, and Thiran JP. Multiscale image segmentation using active contours. EPFL-ITS Technical Report 2005-012, 1015 Ecublens, April 2005.
  - [47] P. Hagmann. *From diffusion MRI to brain connectomics*. PhD thesis, STI-ITS, Ecole polytechnique fédérale de Lausanne, Switzerland, 2005.
  - [48] P. Hagmann, T. Reese, W. Tseng, R. Meuli, JP. Thiran, and Wedeen V. Diffusion spectrum imaging tractography in complex cerebral white matter: An investigation of the centrum semiovale. In *ISMRM 12'th scientific meeting*, volume 12, page 623, May 2004.
  - [49] P. Hagmann, J.P. Thiran, L. Jonasson, P. Vandergheynst, S. Clarke, and R. Meuli. Dti mapping of human brain connectivity: Statistical fibre tracking and virtual dissection. *NeuroImage*, 19(3):545–554, 2003.
  - [50] E.L. Hanh. Spin echos. *Phys. Rev.*, 80:580–594, 1950.
  - [51] RM. Henkelman. Measurement of signal intensities in the presence of noise in mr images. *Med. Phys.*, 12:232–233, 1985.
  - [52] D. Hervé, N. Molko, S. Pappata, F. Buffon, D. LeBihan, M-G. Bousser, and H. Chabriat. Longitudinal thalamic diffusion changes after middle cerebral artery infarcts. *Journal of Neurology Neurosurgery and Psychiatry*, 76:200–205, 2005.
  - [53] J.P Hornak. The basics of mri. URL <http://www.cis.rit.edu/htbooks/mri/>.
  - [54] K.M. Jansons and D.S. Alexander. Persistent angular structure: new insights from diffusion mri data. *Inverse problems*, In Press, 2003.
  - [55] L. Jonasson, X. Bresson, P. Hagmann, R. Meuli, O. Cuisenaire, and J.-Ph. Thiran. White matter fiber tract segmentation in dt-mri using geometric flows. *Medical Image Analysis*, In Press, 2004.
  - [56] L. Jonasson, P. Hagmann, X. Bresson, Thiran JP., and V.J. Wedeen. Representing diffusion mri in 5d for segmentation of white matter tracts with a level set method. In *Information Processing in Medical Imaging, July 2005*, 2005.

- 
- [57] L. Jonasson, P. Hagmann, X. Bresson, R. Meuli, O. Cuisenaire, and J.-Ph. Thiran. White matter mapping in dt-mri using geometric flows. In *Computer Aided Systems Theory - Eurocast 2003, LNCS 2809*, pages 585–595. Springer, 2003.
  - [58] L. Jonasson, P. Hagmann, Thiran JP., and V.J. Wedeen. Fiber tracts of high angular resolution diffusion mri are easily segmented with spectral clustering. In *Proceedings of 13th Annual Meeting ISMRM, Miami*, page 1310, 2005.
  - [59] L. Jonasson, P. Hagmann, C. Pollo, X. Bresson, C. Richero Wilson, R. Meuli, and Thiran JP. A level set method for segmentation of the thalamus and its nuclei in dt-mri. [submitted]. *Special Issue of Signal Processing on Diffusion Tensor Imaging*, 2005.
  - [60] L. Jonasson, P. Hagmann, C. Richero Wilson, X. Bresson, C. Pollo, R. Meuli, and Thiran JP. Coupled, region based level sets for segmentation of the thalamus and its subnuclei in dt-mri. In *Proceedings of 13th Annual Meeting ISMRM, Miami*, page 731, 2005.
  - [61] D.K. Jones, L.D. Griffin, D.C. Alexander, M. Catani, , M.A. Horsfield, R. Howard, and S.C. Williams. Spatial normalization and averaging of diffusion tensor mri data sets. *NeuroImage*, 17:592–617, 2002.
  - [62] L. Kleiser and T.A. Zang. Numerical simulation of transition in wall-bounded shear flows. *Annual Review of Fluid Mechanics*, 23(23):495–537, 1991.
  - [63] P.C. Lauterbur. *Nature*, 242:190, 1973.
  - [64] C. Lenglet, M. Rousson, and R. Deriche. Segmentation of 3d probability density fields by surface evolution: Application to diffusion mri. In *Proc. 7th Intl. Conf. on Medical Image Computing and Computer Assisted Intervention*, Saint-Malo, France, September, 2004.
  - [65] C. Lenglet, M. Rousson, R. Deriche, and O. Faugeras. Inferring white matter geometry from diffusion tensor mri: Application to connectivity mapping. In *Pajdla and Matas*, Prague, Czech Republic, 2004. Springer-Verlag.
  - [66] E. Leriche and S. Gavrilakis. Direct numerical simulation of the flow in a lid-driven cubical cavity. *Physics of Fluids*, 12(6):1363–1376, 2000.
  - [67] Z.P. Liang and E. Haacke. *Encyclopedia of Electrical and Electronics Engineering*. 1999.
  - [68] K.O. Lim and J.A. Helpert. Neuropsychiatric applications of dti - a review. *NMR Biomed*, 15:587–593, 2002.
  - [69] L.M. Lorigo, O. Faugeras, W.E.L. Grimson, R. Keriven, R. Kikinis, and C.F. Westin. Co-dimension 2 geodesic active contours for mra segmentation. In *IPMI 1999*, pages 126–139, 1999.

- 
- [70] O. Mansfield and P.K. Grannell. *J. Phys.*, C6:L422, 1973.
- [71] W. Mulder, S.J. Osher, and J.A. Sethian. Computing interface motion in compressible gas dynamics. *Jour. Comp. Phys.*, 100:209–228, 1992.
- [72] D. Mumford and J. Shah. Optimal approximation by piecewise smooth functions and associated variational problems. *Commun. Pure Appl. Math.*, 42:577–685, 1989.
- [73] A. Ng, M. Jordan, and Y. Weiss. On spectral clustering: Analysis and an algorithm, 2001. URL [citeseer.ist.psu.edu/ng01spectral.html](http://citeseer.ist.psu.edu/ng01spectral.html).
- [74] L. O'Donnell, Haker S., and Westin C.F. New approaches to estimation of white matter connectivity in diffusion tensor mri: Elliptic pdes and geodesics in a tensor-warped space. In *MICCAI2002*, 2002.
- [75] S. Osher and N. Paragios. *Geometric Level Set Methods in Imaging, Vision, and Graphics*. 2003.
- [76] S. Osher and J.A. Sethian. Fronts propagating with curvature-dependent speed: Algorithms based on Hamilton-Jacobi formulations. *Journal of Computational Physics*, 79:12–49, 1988. URL [citeseer.nj.nec.com/osher88fronts.html](http://citeseer.nj.nec.com/osher88fronts.html).
- [77] S. Pajevic and C. Pierpaoli. Color schemes to represent the orientation of anisotropic tissues from diffusion tensor data: application to white matter fiber tract mapping in the human brain. *Magn Reson Med*, 42(3):526–40, 1999.
- [78] N. Paragios and R. Deriche. Coupled geodesic active regions for image segmentation. Technical Report 3783, INRIA, Oct. 1999.
- [79] N. Paragios and R. Deriche. Geodesic active regions: A new paradigm to deal with frame partition problems in computer vision. *Journal of Visual Communication and Image Representation*, Mar./Jun, 2003.
- [80] G.J.M Parker, C.A.M. Wheeler-Kingshott, and G.J. Barker. Distributed anatomical brain connectivity derived from diffusion tensor imaging. In *IPMI 2001*, pages 106–120, 2001.
- [81] D.J. Pettey and J.C. Gee. Sexual dimorphism in the corpus callosum: A characteristic of local size variations and a classification driven approach to morphometry. *NeuroImage*, 17:1504–1511, 2002.
- [82] A. Pfefferbaum and E.S. Sullivan. Microstructural but not macrostructural disruption of white matter in women with chronic alcoholism. *NeuroImage*, 15:708–718, 2002.
- [83] E.M. Purcell, H.C. Torrey, and R.V. Pound. Resonance absorption by nuclear magnetic moments in a solid. *Phys. Rev.*, 69:37, 1946.

- 
- [84] M. Rousson, C. Lenglet, and R. Deriche. Level set and region based surface propagation for diffusion tensor mri segmentation. In *CVAMIA and MMBIA*, 2004.
  - [85] G. Sapiro. Color snakes. 1995.
  - [86] G. Schaltenbrand and W. Wahren. *Atlas for Stereotaxy of the Human Brain*. 1977.
  - [87] JA. Sethian. *Level set methods and fast marching methods: Evolving interfaces in computational geometry, fluid mechanics, computer vision, and materials science*. 1999.
  - [88] EO Stejskal. Use of spin-echos in a pulsed magnetic-field gradient to study anisotropic diffusion and flow. *J Chem Phys*, 43:3597–3603, 1965.
  - [89] EO Stejskal and JE Tanner. Spin diffusion measurements - spin echoes in presence of a time-dependent field gradient. *J Chem Phys*, 42(1):288–292, 1965.
  - [90] PC Sundgren, Q. Dong, D. Gomez-Hassan, S. Mukherji, P. Maly, and R. Welsh. Diffusion tensor imaging of the brain:review of clinical applications. *Neuroradiology*, 46:339–350, 2004.
  - [91] M. Sussman, E. Fatemi, P. Smereka, and S. Osher. An improved level set method for incompressible two-phase flows. *Computers and Fluids*, 27(5-6):663–680, 1998.
  - [92] J. Talairach and P. Tournoux. *Co-planar stereotaxic atlas of the human brain : 3-dimensional proportional system : an approach to cerebral imaging*. 1988.
  - [93] W.D. Taylor, E. Hsu, K. Ranga Rama Krishnan, and JR. MacFall. Diffusion tensor imaging: Background, potential and utility in psychiatric research. *Biol. Psychiatry*, 55:201–207, 2004.
  - [94] C.R. Tench, P.S. Morgan, M. Wilson, and L.D. Blumhardt. White matter mapping using diffusion tensor mri. *Magn Reson Med*, 47(5):967–72, 2002.
  - [95] HC. Torrey. Bloch equation with diffusion terms. *Physical Review*, 104:563–565, 1956.
  - [96] J.D. Tournier, F. Calamante, M.D. King, D.G. Gadian, and A. Connelly. Limitations and requirements of diffusion tensor fiber tracking: an assessment using simulations. *Magn Reson Med*, 47(4):701–8, 2002.
  - [97] D. Tschumperle and R. Deriche. Diffusion tensor regularization with constraints preservation. In *CVPR'2001*. Computer Vision and Pattern Recognition, 2001.
  - [98] D.S. Tuch. *Diffusion MRI of Complex Tissue Structure*. PhD thesis, Division of Health Science and Technology, MIT, 2002.
  - [99] DS Tuch, TG Reese, MR Wiegell, and VJ Wedeen. Diffusion mri of complex neural architecture. *Neuron*, 40(5):885–895, 2003.

- 
- [100] BC. Vemuri, Rao M. Chen, Y., T. McGraw, Z. Wang, and T. Mareci. Fiber tract mapping from diffusion tensor mri. In *Proceedings of the IEEE Workshop on Variational and Level Set Methods in Computer Vision*, pages 81–88, 2001.
  - [101] Z. Wang and B. Vemuri. An affine invariant tensor dissimilarity measure and its applications to tensor-valued image segmentation. In *Computer Vision and Pattern Recognition, 2004. CVPR 2004.*, pages 228–233. Proceedings of the 2004 IEEE Computer Society Conference on, 2004.
  - [102] Z. Wang and B. Vemuri. Tensor field segmentation using region based active contour model. In *ECCV 2004, LNCS 3024*, pages 304–315. Springer, 2004.
  - [103] V.J. Wedeen, P. Hagmann, WYI. Tseng, T.G. Reese, and T.G. Weisskoff. Mapping complex tissue architecture with diffusion spectrum magnetic resonance imaging. *Accepted Magn Res Med*, 2005.
  - [104] V.J. Wedeen, T.G. Reese, D.S. Tuch, M. R. Wiegell, T.G. Weisskoff, and D. Chessler. Mapping fiber orientation spectra in cerebral white matter with fourier-transform diffusion mri. In *Proceedings of 8th Annual Meeting ISMRM, Denver*, page 82, 2000.
  - [105] V.J. Wedeen, R. Wang, T. Benner, P. Hagmann, W-Y. Tseng, G. Sorensen, and A. de Crespigny. Dsi tractography of cns fiber architecture and cortical architectonics. In *Proceedings of 13th Annual Meeting ISMRM, Miami*, page 584, 2005.
  - [106] Y. Weiss. Segmentation using eigenvectors: a unifying view. In *Proc. IEEE Int. Conf. on Computer Vision*, pages 975–982, 1999.
  - [107] E. Weisstein. Mathworld. URL <http://mathworld.wolfram.com/>.
  - [108] M. R. Wiegell, D. S. Tuch, H. B.W. Larsson, and V. J. Wedeen. Automatic segmentation of thalamic nuclei from diffusion tensor magnetic resonance imaging. *NeuroImage*, 19:391–401, 2003.
  - [109] J. Zhu and J.A. Sethian. Projection methods coupled to level set interface techniques. *J. Comp. Phys.*, 102:128–138, 1992.
  - [110] L. Zhukov, K. Museth, D. Breen, R. Whitaker, and A. Barr. Level set modelling and segmentation of dt-mri brain data. *Journal of Electronic Imaging*, 12(1):125–133, 2003.



---

# Curriculum Vitae

---

***Full name:*** Lisa Jonasson

***Degrees:*** Master of Science in Engineering Physics,  
Chalmers University of Technology, Göteborg, Sweden

***Address:*** Signal Processing Institute (ITS)  
School of Engineering (STI)  
Swiss Federal Institute of Technology (EPFL)  
CH-1015 Lausanne  
Switzerland

***Contact numbers:*** Tel. (+41 21) 693 36 32  
Fax. (+41 21) 693 76 00  
E-mail: lisa.jonasson@epfl.ch

***Civil status:*** Single

***Date and place of birth:*** August 9<sup>th</sup> 1976, Sweden

***Nationality:*** Swedish

---

## Professional Experiences

---

- Since  
Mar. 2002*** Research Assistant at the Signal Processing Institute (ITS),  
Swiss Federal Institute of Technology at Lausanne (EPFL)  
- leading to a Ph.D. in medical image processing.  
Under the direction of Prof. Jean-Philippe Thiran.  
Research activities: high dimensional image processing, image segmentation, level set methods, Diffusion Weighted MRI, DT-MRI, DSI
- Oct. 2004 -  
Dec. 2004*** Visiting research fellow, NMR center,  
MGH, Harvard Medical School, Boston, United States.  
Invited by: Prof. Van J Wedeen.  
Research activities: Diffusion Spectrum Imaging
- Mar. 2001 -  
Feb. 2002*** Research Assistant at the Signal Processing Institute (ITS),  
Swiss Federal Institute of Technology at Lausanne (EPFL).  
Under the direction of Prof. Jean-Philippe Thiran.  
Research activities: Development of a new segmentation tool for ultrasound images.
- Sept. 2000 -  
Feb. 2001*** Student position in TEMICS (Traitement, Modélisation d'Images et Communications) group, IRISA, Rennes, France.  
Under the direction of Dr. Stephane Pateux.  
Completed diploma work on scalable video coding based on active adaptive meshes.
- Sept. 1999 -  
Aug. 2000*** Chalmers China Japan Committee.  
Volunteered during my engineering studies on finding sponsors, selling ads, organizing company presentations and developing a CV data base of technology students that were promoted and sold to Swedish companies.
- Jun. - Aug.  
1998 and 1999*** Programmer at the Antenna Design Department, Ericsson Microwave Systems, Mölndal, Sweden.  
Participated in the development of antenna analysis software in MATLAB for radar surveillance, including the verification of programs in Fortran and MATLAB.
- Jun. 1995 -  
Aug. 1996*** Engineer at the Electro Magnetic Compatibility (EMC) Department.  
Performed EMC-tests on electronic devices and for automotive industry

## Publications

---

### Journal Papers

- L. Jonasson, X. Bresson, P. Hagmann, O. Cuisenaire, R. Meuli and J. Thiran  
White matter fiber tract segmentation in DT-MRI using geometric flows  
Medical Image Analysis, Vol. 9, No 3, pp. 223-236, June 2005
- G. Devuyt, T. Karapanayiotides, M. Pustaszari, J. Lobrinus, L. Jonasson, O. Cuisenaire, A. Kalangos, P. Despland, J. Thiran, P. Ruchat and J. Bogousslavsky  
Ultrasound Measurement of the Fibrous Cap in Symptomatic and Asymptomatic Atheromatous Carotid Plaques  
Circulation, Vol. 111, No 21, pp. 2776-2782, May 2005
- L. Jonasson, P. Hagmann, C. Pollo, X. Bresson, C. Richero Wilson, R. Meuli and J. Thiran  
A level set method for segmentation of the thalamus and its nuclei in DT-MRI.  
*Submitted* Special Issue of Signal Processing on Diffusion Tensor Imaging, 2005
- P. Hagmann, J. Thiran, L. Jonasson, P. Vandergheynst, S. Clarke, P. Maeder and R. Meuli  
DTI mapping of human brain connectivity: statistical fibre tracking and virtual dissection  
Neuroimage, Vol. 19, No 3, pp. 545-554, July 2003

### Conference Papers

- L. Jonasson, P. Hagmann, X. Bresson, J. Thiran and V. Wedeen  
Representing Diffusion MRI in 5D for Segmentation of White Matter Tracts with a Level Set Method.  
Information Processing in Medical Imaging, July 2005.
- L. Jonasson, P. Hagmann, C. Richero Wilson, X. Bresson, C. Pollo, R. Meuli and J. Thiran  
Coupled, region based level sets for segmentation of the thalamus and its subnuclei in DT-MRI.  
Proceedings of 13th Annual Meeting , Miami, p. 731, 2005
- L. Jonasson, P. Hagmann, J. Thiran and V. Wedeen  
Fiber tracts of high angular resolution diffusion MRI are easily segmented with spectral clustering.  
Proceedings of 13th Annual Meeting , Miami, p. 1310, 2005
- P. Hagmann, J. Thiran, L. Jonasson, R. Meuli, S. Clarke, P. Vandergheynst and P. Maeder  
Mapping Brain Connectivity with Statistical Fibre Tracking and Virtual Dissection

Proc.

Intl. Soc. Mag. Reson. Med, ISMRM 11th scientific meeting, Toronto, Canada, Vol. 11, p. 2156, July 2003

- L. Jonasson, P. Hagmann, X. Bresson, R. Meuli, O. Cuisenaire and J. Thiran  
White Matter Mapping in DT-MRI Using Geometric Flows  
Computer Aided Systems Theory - EUROCAST 2003, Vol. 2809, pp. 585-596, 2003

#### **Master thesis**

- C. Richero Wilson, L. Jonasson and J. Thiran  
Competing Level Sets for Segmentation of the Thalamus  
June 2004
- R. Bartolomé Méndez, L. Jonasson and J. Thiran  
Ultrasound Texture Analysis for Massetric Muscle Health Evaluation  
May 2002

#### **Invited talks**

- Segmentation of Diffusion Tensor MRI Using Level Set Methods.  
Center for Imaging Science, John Hopkins University, Baltimore, USA  
December 07, 2004
- White matter segmentation in DW-MRI using geometric flows  
MR-Physik und Departement für Medizinische Radiologie Universitätsspital, Basel,  
Switzerland.  
June 08, 2004

---

## Studies

---

- Since 2002***      Swiss Federal Institute of Technology (EPFL),  
Lausanne, Switzerland  
Signal Processing Institute (ITS) of the School of Engineering (STI)  
Working towards a Ph.D. thesis (Docteur ès Sciences)
- 1996-2001***      Chalmers University of Technology, Göteborg, Sweden  
Physics Department  
Master of Science in Engineering Physics, February 2001

---

## Post-graduate Education

---

- 2002***              Biomedical Imaging: IEEE Summer School on Biomedical Imaging,  
Berder Island, France

---

## Languages

---

- Swedish:***          mother tongue
- English:***          fluent
- French:***            fluent
- Danish:***            fluent

---

## Computer Skills

---

- Programming languages:*** Matlab, C/C++
- Operating systems:*** Linux, Unix, Windows
-

